MASSACHUSETTS INSTITUTE OF TECHNOLOGY

DEPARTMENT OF NUCLEAR ENGINEERING

Cambridge, Massachusetts

DESIGN OF A COLD NEUTRON SOURCE FOR THE MIT REACTOR

by

R. C. Sanders, D. D. Lanning,

T. J. Thompson

May, 1970

MITNE-114

MASSACHUSETTS INSTITUTE OF TECHNOLOGY

DEPARTMENT OF NUCLEAR ENGINEERING

Cambridge, Massachusetts

DESIGN OF A COLD NEUTRON SOURCE FOR THE MIT REACTOR

by

R. C. Sanders, D. D. Lanning,

T. J. Thompson

May, 1970

MITNE-114

ABSTRACT

A new design for the MIT reactor thermal column has been developed to increase the thermal neutron flux in that region. By removing graphite from the thermal column and creating a cavity with graphite walls, it is possible to increase the thermal neutron flux by a factor of about 30. The location of a scattering material, such as a cold neutron moderator, in the cavity does not greatly reduce this increase in neutron flux, but does cause an asymmetry in the flux incident on the scatterer. The flux incident on the source side of the scatterer is approximately 60% higher than the flux incident on the back side.

A cold neutron cryostat has been designed, built, and tested in the present MIT reactor thermal column. The cryostat consists of a 12 inch diameter aluminum sphere containing D_2O ice cooled by cold gaseous helium in aluminum coils. The sphere is surrounded by an aluminum vacuum jacket to form the cryostat. Initial testing indicates that the cryostat is effective in increasing the number of long wavelength neutrons. For a cold D_2O moderator temperature of a -40°C the measured increase in neutrons of 5 Å wavelength is about a factor of 1.8. From this experimental result it is estimated that there will be a factor of about 50 gain in 5 Å neutrons for a moderator temperature of 20°K.

The expected neutron spectrum in the cold moderator has also been calculated theoretically. The theory predicts the observed increases in cold neutron intensities; however, it over estimates the gain in 5 Å neutrons by about 25%. This difference falls within the uncertainty in the value for the effective mass of the D_2O ice.

BLANK PAGE

ACKNOWLEDGMENTS

The author thanks Dr. Theos. J. Thompson for his assistance and guidance as the initial supervisor of this work. He expresses his appreciation to Dr. David D. Lanning who assumed the position of thesis supervisor when Dr. Thompson undertook the role of AEC Commissioner in 1969. He also thanks Dr. N. Thomas Olson, the thesis reader, for his helpful suggestions, especially in the writing of the manuscript.

The assistance of Dr. Yoshiguti Hukai and Mr. Ronald J. Chin in carrying out the experimental work is greatly appreciated. Dr. Franklyn M. Clikeman and Mr. David A. Gwinn are thanked for the assistance they provided in setting up the electronics of the neutron detection system.

The author would like to thank the MIT Reactor Staff, the Reactor Machine Shop, the Reactor Electronics Shop, and the Radiation Protection Office for their assistance and suggestions.

The typing was done by Mrs. Carol Lindop, and the drawings by Mr. Leonard Andexler. Their assistance is appreciated. Miss Roberta Dailey is also thanked for her assistance in preparing the final manuscript.

The computations for this thesis have been done in part at the MIT Information Processing Center on the IBM 360/65.

The author was supported in part by an Atomic Energy Commission Fellowship in Nuclear Science and Engineering, and

by a National Science Foundation Graduate Fellowship.

This project has been supported by a Sloan Pure Physics Research Grant.

TABLE OF CONTENTS

LIST OF FIGURES

LIST OF TABLES

Chapter 1

Introduction

Cold neutrons are defined as those neutrons having energies less than 0.005 ev or wave-lengths longer than about 4 Å. At these wave-lengths cold neutrons become important tools in material science because their wavelength is on the order of lattice spacings in solids.

For several years X-rays have been used for studying materials. Cold neutrons can now be used to extend the range of these studies. First, X-rays interact with atoms while neutrons interact with nuclei. Thus, cold neutrons can give more detailed information about the lattice; for example, the magnetic dipole moments of the atoms making up the lattice.

Secondly, because of their much shorter interaction time with the lattice, X-ray see the static position while cold neutrons see position as a function of time, and thus more information is obtained about the thermal motions of the lattice. The vibrational period of a lattice is on the order of 10^{-14} seconds compared with a traverse time of 10^{-18} seconds for an X-ray, and 3×10^{-13} seconds for a 0.005 ev neutron.

The energy of the X-ray scattered from the atom is independent of the thermal motions of the atom; whereas, a scattered neutron can either gain or loose energy, depending on the thermal motion of the scattering nucleus. Therefore, the cold neutron can give information about the type and energy of the thermal motion of the atom in the lattice (26).

Although cold neutrons are effective tools, their use has

been limited because of the low intensity of beams usually available from thermal reactors. The thermal neutron spectrum of such a reactor is very nearly a maxwellian distribution at the temperature of the moderator which is typically above 300°K. At this temperature the flux of 4 Å neutrons is less than 1/16 the maximum flux, while the flux of 8 Å neutrons is less than 1/14 the 4 Å flux (27).

One method of increasing the cold neutron fraction of the neutron spectrum is to extract the beam from near the reactor core where the thermal flux is the highest and eliminate that part of the spectrum with wavelengths shorter than 4 Å by using a beryllium filter; however, in this case the cold neutron beam has a high probability of being hidden in the fast neutron and gamma ray background. With this in mind the obvious method of obtaining a high intensity cold neutron beam appears to be to increase the cold neutron fraction of the thermal spectrum through the use of a cold moderator located where the fast neutron and gamma ray fluxes are minimal.

Ideally the cold moderator shifts the thermal neutron spectrum from that characteristic of the reactor temperature (on the order of 300°K) to a spectrum characteristic of the temperature of the cold moderator (100°K or less). This will increase the relative number of low energy neutrons. To do this it is necessary for the cold moderator to have a large slowing down power and a low absorption cross section.

Hydrogenous materials have high slowing down powers; however, because of the high hydrogen absorption cross section that increases with decreasing neutron energy, a large fraction

of the cold neutrons are absorbed in the moderation and the maximum possible gain in cold neutrons is not realized. On the other hand, non-hydrogenous materials, such as deuterium oxide, beryllium, and graphite, with low absorption cross sections; have relatively low slowing down powers and therefore large volumes are needed to obtain high cold neutron gains. Consequently a large cooling capacity is needed to maintain the moderator at a low temperature.

Another disadvantage of hydrogenous materials is their decomposition in a high radiation field. This presents the possibility of producing hydrogen gas in sufficient quantities to form an explosive mixture with oxygen upon warming up the moderator. On the other hand, heavy water is less susceptible to radiation damage (28).

To date several cold neutron sources have been located in various reactors (27, 29, 30, 31). In general these have been located in beam tubes of reactors and have been limited in size to a few hundred cubic centimeters. Consequently these cold neutron sources have not been efficient in producing high cold neutron gains; however, they have provided valuable information about cold moderating materials.

In 1968, installation of a helium liquifying plant was initiated at the MIT reactor to provide coolant for an incore cryostat to be used to study radiation damage in materials. The plant is expected to deliver about 100 liters of liquid helium per hour to the incore cryostat. The discharge from the incore cryostat is expected to be gaseous helium at a temperature of

between 10 and 20 degrees Kelvin. With this large cooling capacity available, it was decided to locate a cold neutron source in the thermal column of the reactor. This location has been selected for the following reasons.

First, with the large cooling capacity available, it is desirable to take advantage of a large volume of non-hydrogenous cold moderator. The thermal column provides the necessary space for such a moderator.

Second, with a large volume moderator the induced heating due to gamma rays and fast neutrons is appreciable. Consequently one would like to locate the cold moderator as far as possible from the reactor core, but still in a high thermal neutron flux. By removing graphite from the thermal column it is possible to create a cavity around the cold neutron source. Such a cavity allows neutrons to stream rapidly down the thermal column with a minimum amount of leakage out through the sides; thus, enhancing the thermal flux available to the cold moderator.

The purpose of this work is twofold. First, Chapters 2 through 4 discuss the optimization of the thermal column. The effect of a cavity on the thermal flux in the thermal column is investigated. A detailed analysis is carried out to determine the optimum cavity size for the maximum thermal neutron flux.

Second, Chapters 5 through 7 discuss the design, construction, and testing of 15 liter cold neutron source which is located in the present thermal column, and is to be used to gain information about and operating experience with a large volume cold neutron source. Also presented are calculations of the expected neutron spectrum in the cold moderator.

Chapter 2

Hohlraum Flux Calculations

2.1. Method

A calculational model used for optimizing the thermal neutron flux in the thermal column is derived in this section. The thermal column is located between the reactor core and the heavy water lattice facility, as shown in figure 2.1. To enhance the thermal flux in the thermal column, it is proposed to remove graphite from the thermal column; thus, creating a cavity or hohlraum with graphite walls. The method used to calculate the effect of such a cavity on the thermal flux in the thermal column is the same as that used by John Madell (2) in the design of the hohlraum below the heavy water lattice facility (figure 2.1).

Consider a cavity surrounded by reflecting walls, with a source of neutrons on one of the surfaces. Since the cavity is filled with air, it will be assumed that the neutrons have an infinite mean free path in the cavity, and consequently suffer collisions only at the walls.

Let $dA(\underline{r})$ be a differential area located at $\underline{r}$ on one of the surfaces, and $G(\underline{r})$ be the number of neutrons/$cm^2 \cdot$sec incident on $dA(\underline{r})$. Then $G(\underline{r})\, dA(\underline{r})$ is the number of neutrons/sec incident on $dA(\underline{r})$.

Let $S(\underline{r}')$ be the number of neutron/$cm^2 \cdot$sec emitted by the source at $\underline{r}'$, and $K_1(\underline{r},\underline{r}')$ be the probability that a neutron emitted at $\underline{r}'$reaches $\underline{r}$. Then the number of neutrons/sec emitted

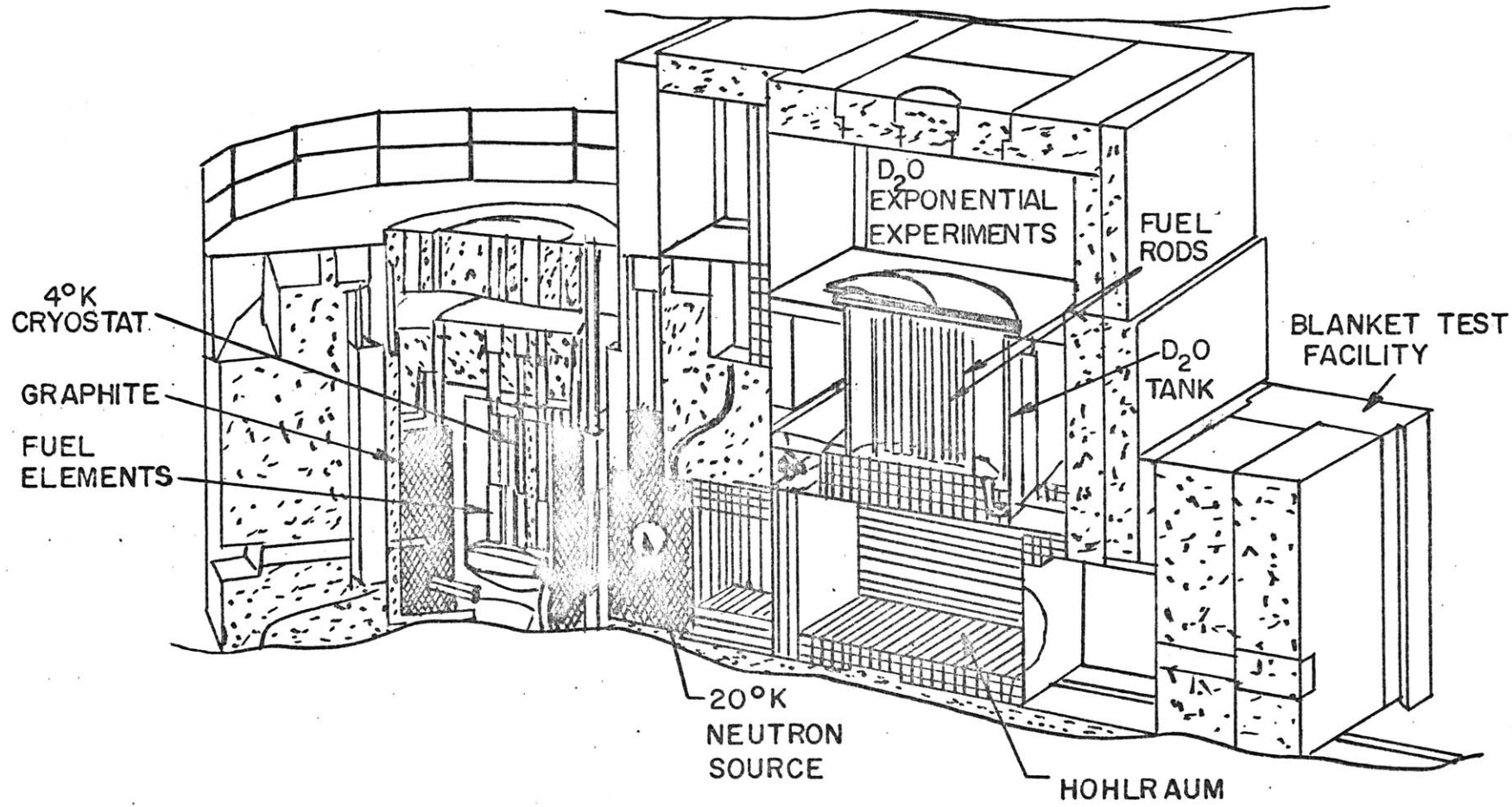

FIG. 2.1 CUT-AWAY VIEW OF THE MITR RESEARCH REACTOR

by the source at $\underline{r}'$ and reaching $\underline{r}$ is given by

$$\int_{\text{Source } \underline{r}'} S(\underline{r}')K_1(\underline{r},\underline{r}')dA(\underline{r}'). \qquad (2.1)$$

Let $K_2(\underline{r},\underline{r}')$ be the probability that a neutron incident on the surface at $\underline{r}'$ be scattered back into the cavity and reaches $\underline{r}$. Then the number of neutrons/sec reaching $\underline{r}$ due to scatters at $\underline{r}'$ is given by

$$\int_{\text{All } \underline{r}'} G(\underline{r}')K_2(\underline{r},\underline{r}')dA(\underline{r}'). \qquad (2.2)$$

Applying a steady-state neutron balance results in

$$G(\underline{r})dA(\underline{r}) = \int_{\text{All } \underline{r}'} G(\underline{r}')K_2(\underline{r},\underline{r}')dA(\underline{r}') + \int_{\text{Source } \underline{r}'} S(\underline{r}')K_1(\underline{r},\underline{r}')dA(\underline{r}'). \qquad (2.3)$$

The above equation is exact; however, it cannot be solved because of the unknown Kernals, $K_2(\underline{r}, \underline{r}')$ and $K_1(\underline{r},\underline{r}')$. Before proceding, it will therefore be necessary to make some simplifying assumptions. These assumptions are discussed in a latter section of this chapter.

Since $K_2(\underline{r},\underline{r}')$ is the probability that a neutron incident on the surface at $\underline{r}'$ is scattered back into the cavity and reaches $\underline{r}$, it may be considered as the product of two probabilities. First is the probability that a neutron incident on the surface at $\underline{r}'$ be scattered back into the cavity at $\underline{r}'$. In diffusion theory one defines the albedo as the ratio of the number of neutrons/cm^2·sec leaving the surface to the number of neutrons/cm^2·sec entering the surface. This is the probability that neutrons entering the surface will be scattered back out; however it is an average effect over the entire surface and does

not take into account the fact that a neutron may enter the surface at one point and leave at another. The first assumption then will be that the scattering (reflection) is a surface effect and the albedo can be defined at a point.

Second is the probability that a neutron emitted at $\underline{r}'$ reaches $\underline{r}$. If it is assumed that the scattered neutrons and the source neutrons are emitted from the surface according to Lambert's Law; that is, the probability that a neutron leaves the surface in solid angle dw at an angle ϕ' with respect to the normal to the surface is given by (1),

$$\frac{\cos \phi}{\pi} \, dw \qquad (2.4)$$

then equation (2.3) becomes,

$$G(\underline{r})dA(\underline{r}) = \int_{\text{All } \underline{r}'} G(\underline{r}')B(\underline{r}')K_1(\underline{r},\underline{r}')dA(\underline{r}') + \int_{\text{Source } \underline{r}'} S(\underline{r}')K_1(\underline{r},\underline{r}')dA(\underline{r}') \qquad (2.5)$$

where $B(\underline{r}')$ = albedo at $\underline{r}'$

$$K_1(\underline{r},\underline{r}') = \frac{\cos\phi'\cos\phi}{\pi|\underline{r}-\underline{r}'|^2}dA(\underline{r}) \qquad (2.6)$$

$|\underline{r}-\underline{r}'|$ = distance from $\underline{r}$ to $\underline{r}'$

ϕ = angle between the normal to $dA(\underline{r})$ and $(\underline{r}-\underline{r}')$

$\cos\phi\frac{dA(r)}{|\underline{r}-\underline{r}'|^2}$ = Solid angle subtended by $dA(\underline{r})$ at $\underline{r}'$.

Using this, equation 2.4 becomes

$$G(\underline{r})dA(\underline{r}) = \int_{\text{All } \underline{r}'} G(\underline{r}')B(\underline{r}')\left[\frac{\cos\phi'\cos\phi}{\pi|\underline{r}-\underline{r}'|^2}\right]dA(\underline{r})dA(\underline{r}') \qquad (2.7)$$

$$+\int_{\text{Source } \underline{r}'} S(\underline{r}')\left[\frac{\cos\phi'\cos\phi}{\pi|\underline{r}-\underline{r}'|^2}dA(\underline{r})dA(\underline{r}')\right].$$

Integrating over $A(\underline{r}_i) = A_i$ gives,

$$\int_{A_i} G(\underline{r}_i)dA(\underline{r}_i) = \int_{A_i} \int_{\text{All } \underline{r}'} G(\underline{r}')B(\underline{r}')\left[\frac{\cos\phi'\cos\phi}{\pi|\underline{r}_i-\underline{r}'|^2}\right]dA(\underline{r})dA(\underline{r}') + \int_{A_i} \int_{\text{Source } \underline{r}'} S(\underline{r}')\left[\frac{\cos\phi'\cos\phi}{\pi|\underline{r}_i-\underline{r}'|^2}\right]dA(\underline{r})dA(\underline{r}') . \quad (2.8)$$

In principle this equation can be solved for $G(\underline{r})$ once $G(\underline{r}')$, $B(\underline{r}')$, and $S(\underline{r}')$ are specified. In general these are not known; however the integration over $\underline{r}'$ can be performed if it is assumed that the surfaces can be broken up into n small subareas over which these quantities remain constant. The integrations can then be carried out over each subarea and the results summed to give the total integral over $\underline{r}'$. It will also be assumed that A_i is small enough that $G(\underline{r}_i)$ remains constant over this area. Then the equation (2.8) becomes

$$G_i A_i = \sum_{\text{all surfaces}}\{G_n B_n \int_{A_i} dA(\underline{r}_i)\int_{A_n}\left[\frac{\cos\phi'\cos\phi}{\pi|\underline{r}_i-\underline{r}_n|^2}\right]dA(\underline{r}_n)\} + \sum_{\text{all source}} S_k \int_{A_i} dA(\underline{r}_i)\int_{A_k}\left[\frac{\cos\phi'\cos\phi}{\pi|\underline{r}_i-\underline{r}_k|^2}\right]dA(\underline{r}_k)\}. \quad (2.9)$$

Where G_i = Average current incident on A_i

G_n = Average current incident on A_n

B_n = Average albedo for A_n

S_k = Average source for A_k.

But,

$$\int_{A_i} dA(\underline{r}_i)\int_{A_n}\left[\frac{\cos\phi'\cos\phi}{\pi|\underline{r}_i-\underline{r}_n|^2}\right]dA(\underline{r}_n) = A_n F_{ni} \quad (2.10)$$

where F_{ni} is the view factor from A_n to A_i. Thus, equation (2.9) becomes

$$G_i A_i = \sum_{\text{all surfaces}} G_n B_n A_n F_{ni} + \sum_{\text{all source}} S_k A_k F_{ki}. \qquad (2.11)$$

Equation (2.11) can be written for each of the n subareas, resulting in n equations and n unknowns (n G_i's).

Once the currents are known, it is possible to determine the flux on each of the subareas. Since the flux is the population of neutrons at the point of interest, it may be considered as the sum of the incident current and reflected current from the subarea, or

$$Ph_i = G_i + RG_i \qquad (2.12)$$

where Ph_i is the flux and RG_i is the reflected current.

Rewriting gives

$$Ph_i = G_i[1 + B_i] \qquad (2.13)$$

where $B_i = \frac{RG_i}{G_i}$ is the albedo.

2.2 Rectangular Cavities

Equation (2.11) is general for any geometry; however, only in the special case of rectangular geometry can the view factors be found analytically. Since any modification to the thermal column can be done most easily in rectangular geometry, the advantage of this simplifying case will be taken in doing the optimization calculations.

Consider a rectangular cavity as shown in figure 2.2, with a source of neutrons incident on Face 1. The J's and K's are coordinates describing the position of a subarea on a particular

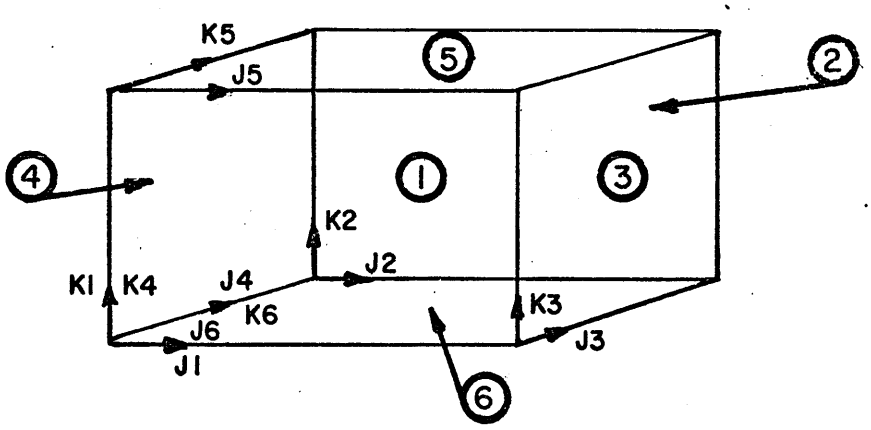

FIG. 2.2 RECTANGULAR CAVITY SHOWING RELATIONSHIP BETWEEN FACES AND COORDINATES

face; for example (J1, K1) means that the lower left hand corner of a subarea on face 1 is at the position (J1, K1) and that it extends from J1 to J1 +L and from K1 to K1 +L where L is the length of the side of the subarea. Also, take the subareas on all the faces to be the same size, so that the areas in equation 2.11 cancel out. Then, using computer program notation, equation 2.11 can be written for each of the faces as

$$GI(JI,KI) = \sum_{KN=1}^{HN} \sum_{JN=1}^{WN} GN(JN,KN)BN(JN,KN)F(L1,L2,L3) + \sum_{K1=1}^{H1} \sum_{J1=1}^{W1} S(J1,K1)F(L1,L2,L3)$$

where N = 1 to 6, except I

HN = maximum value of KN

WN = maximum value of JN

F = view factor

L1, L2, L3 = coordinates describing the relative positions of subareas.

For the view factor from a subarea on plane m to a subarea on a parallel plane, n:

L1 = 1 + |Jm-Jn|

L2 = 1 + |Km-Kn|

L3 = Distance between planes.

For the view factor from a subarea on plane m to a subarea on a perpendicular plane, n:

L1 = distance from line of intersection of planes to subarea on m

L2 = distance of separation of the two subareas along the line of intersection

L3 = distance from line of intersection of the planes to subarea on n.

Note that the equation for any face does not contain a term which is the sum over that face (e.g. face 1 does not contain a sum over the source). This is due to the fact that the subareas on a given face cannot see each other (i.e., the view factors are zero).

The solution to equation 2.14 is obtained by an iteration technique carried out on a digital computer. That is, initial values for the G's are given and used to calculate new values for the G's. The initial values are then replaced by the new values and again new values are calculated. This process is continued until the G's converge (i.e., the calculated values agree with the ones used to calculate them). A description of the computer program (HOLCAV) used to solve equation 2.14 is given in appendix B.

To solve equation 2.14 it is necessary to know the source distribution, the albedos, and the view factors. The source distribution used for optimizing the thermal column is discussed in Chapter 3. A derivation of the view factors and a description of the computer programs used to evaluate them are given in appendix A. The albedos were determined by John Madell with a Monte Carlo calculation and are taken from his thesis.

2.3. Discussion of Assumptions

The first assumption is that the neutrons have an infinite

mean free path in the cavity. For dry air the mean free path for 2200 m/sec neutrons is 1811 cm. The measured temperature in the thermal column is about 70°C (appendix D). At this temperature the saturation pressure of water is 234 mm Hg and the mean free path is 362 cm. A characteristic dimension for the proposed cavity is about 127 cm; therefore, the assumption of an infinite mean free path is valid.

The second assumption is that the albedo can be defined at a point. Since equation 2.11 is for small subareas, this requirement can be relaxed somewhat, in that now the albedo must be defined for a small area rather than for a point. This is the same as assuming that all the neutrons that return to the cavity from the i^{th} subarea were also incident on the i^{th} subarea. That is, neutrons do not enter the wall through one subarea, scatter within the wall, and come out through a different subarea. Madell investigated this problem by means of a Monte Carlo calculation, and found that his albedos were accurate to about one percent provided the average current over a subarea was within 10 percent of the currents incident on adjacent subareas. Except for the corners of the cavity, this condition is usually satisfied.

The third assumption is that the neutrons emerging from a surface do so according to Lambert's Law, that is the probability of being emitted in solid angle dw at an angle ϕ with the normal to the surface is

$$\frac{\cos\phi}{\pi} dw \ .$$

Pigford et al (3) have found that the actual distribution of neutrons being emitted from a graphite surface is a Placzek distribution (4), in which the neutrons emerge preferentially in the forward direction. This distribution is the one that should be used in calculating the view factors; however, its complicated form does not permit one to obtain analytical expressions for the view factors. Madell found that correcting to a Placzek distribution increased the calculated fluxes by one or two percent. For this reason the correction has not been applied in this work. This is also justified by the excellent agreement between calculated and measured fluxes (Chapter 3).

Chapter 3

Test of Model

3.1. Comparison with Experiment

Before applying the model developed in Chapter 1 to the optimization of the thermal column, it is necessary to test the accuracy with which it can predict neutron fluxes. The first test is a comparison of the fluxes calculated by the model with those measured by Madell in the hohlraum below the heavy water lattice facility (figure 2.1). The model of the hohlraum used in the calculation is shown in figure 3.1. Each face is subdivided into 12 inch by 12 inch subareas and assigned albedos taken from Madell's thesis. The source distribution, which is located on face 1, is also taken from Madell's thesis. The way in which the surfaces are subdivided is illustrated by face 1, shown in figure 3.2

The surface of interest in this calculation is the bottom of the pedestal located on face 5 (figure 3.1). Shown in figure 3.3 is a plot of the thermal flux on this surface. Since the flux is symmetric across the pedestal only half the surface is shown. The solid lines are the values calculated by HOLCAV, the dashed lines are the values calculated by Madell, and the points are the experimental values. The error in the experimental points is $\pm 0.83\%$.

The differences between Madell's values and those calculated

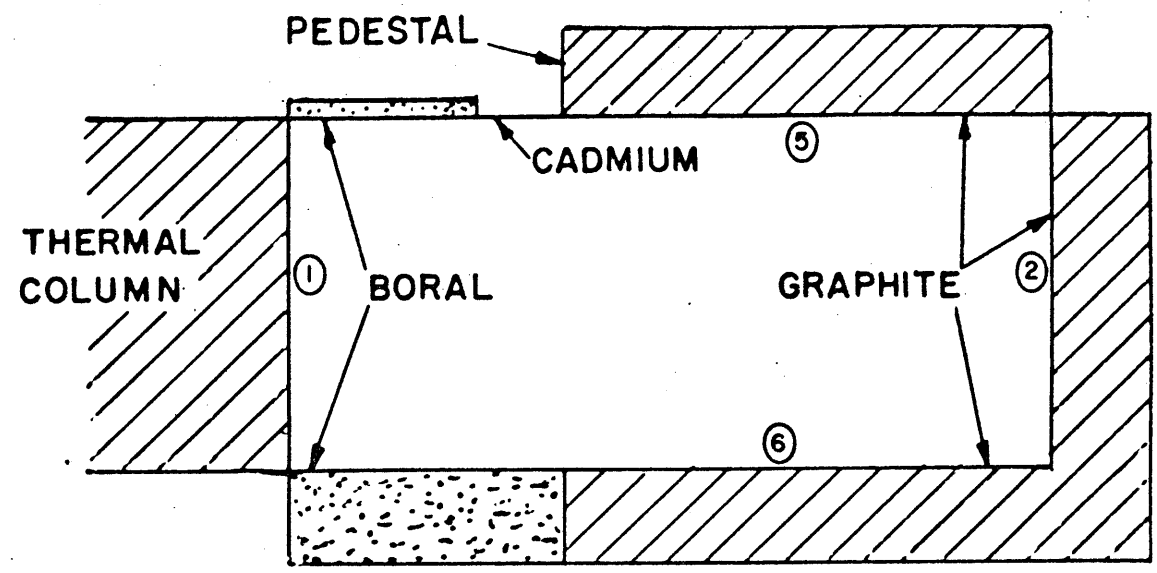

SIDE VIEW

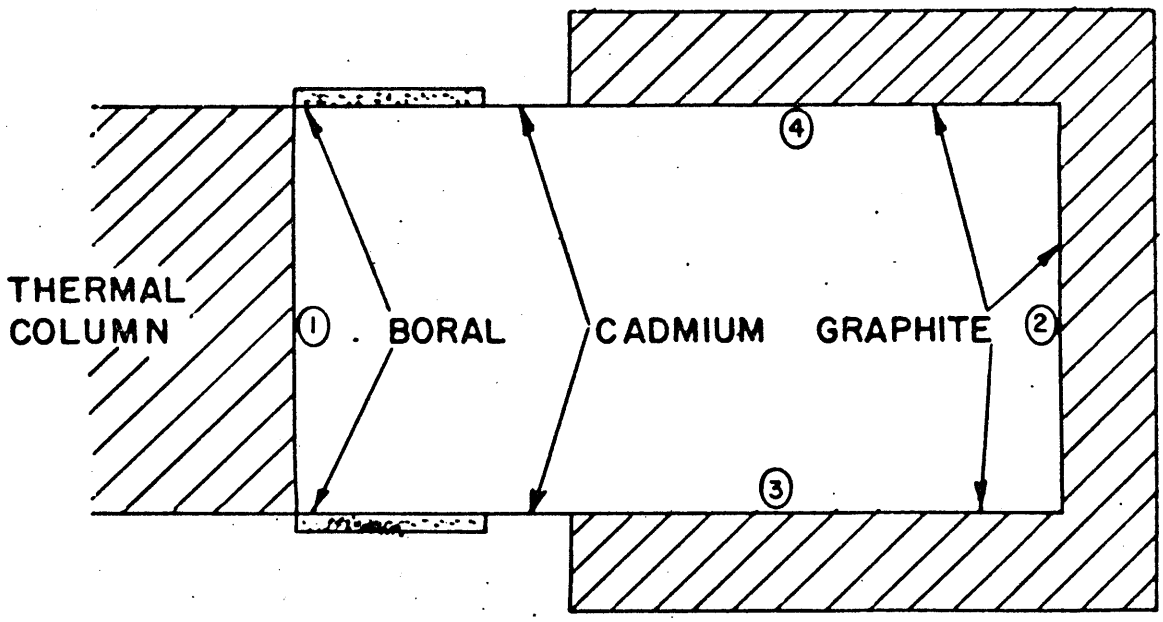

TOP VIEW

FIG. 3.1 HOHLRAUM, SHOWING RELATIONSHIP BETWEEN THE FACES

.02163	.08652	.10959	.10959	.08652	.02163
.03845	.17544	.25594	.25594	.17544	.03845
.04446	.22110	.32684	.32684	.22110	.04446
.03965	.18505	.25955	.25955	.18505	.03965
.02307	.10190	.13266	.13266	.10190	.02307

KI ↑ , → JI

SOURCE, 10^{10} n/cm^2. sec

.69560	.78780	.79090	.79090	.78780	.69560
.7878	.93520	.93520	.93520	.93520	.78780
.79090	.93520	.93520	.93520	.93520	.79090
.78780	.93520	.93520	.93520	.93520	.78780
.69560	.78780	.79090	.79090	.78780	.69560

KI ↑ , → JI

ALBEDOS

FIG. 3.2 HOHLRAUM, FACE I

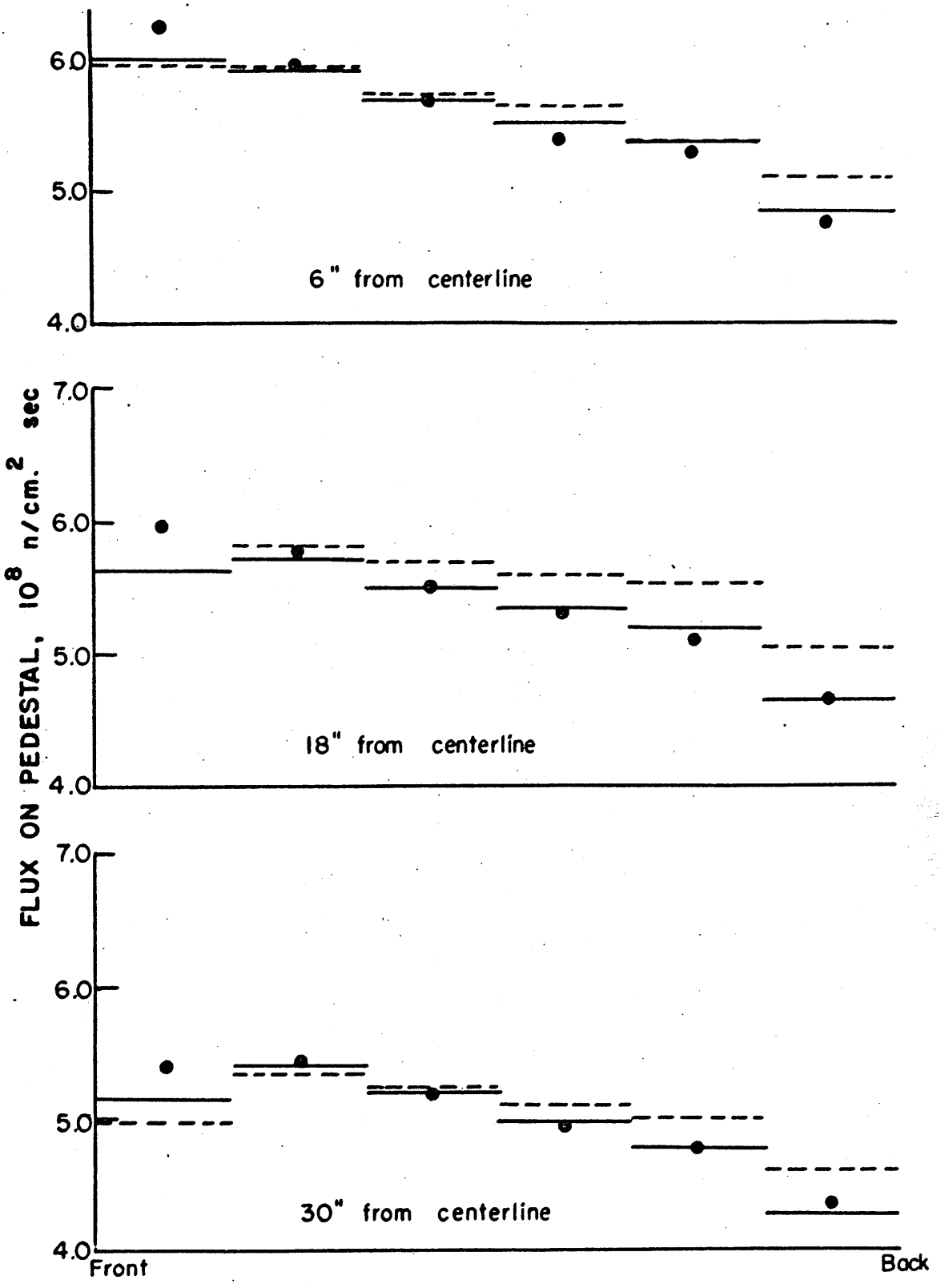

FIG. 3.3 FLUXES ON PEDESTAL

in this work are believed to be due to a correction that has been made to Madell's expressions for calculating the view factors.

As can be seen there is excellent agreement between the calculated and experimental values, except for the front edge. This is believed to be due to assigning too low of an albedo to these subareas. This strip lies along the edge of the pedestal and consequently the subareas were assigned average albedos for 12 inch squares on the edge of a plane. However, this edge is next to cadmium, which, although it is a strong absorber, apparently eliminates some of the edge effect. That is, neutrons may not leak out the edge as fast as one would expect because of backscatter by the cadmium, and consequently the albedo is higher than in the case of an edge with no border.

3.2 Lead Shutters

The calculations involving the lead shutters do not provide a true test of the model in that calculated results are not compared with experimental values. However, the investigation does prove useful for testing the computer program, and provides a problem for which the results of the model being discussed can be compared with those obtained by a Monte Carlo calculation (5).

The location of the lead shutters is shown in figure 2.1. These, along with a cadmium shutter, can be positioned in the one foot gap between the graphite reflector and the thermal column. The purpose of the shutters is to reduce the gamma and fast

neutron radiation in the heavy water lattice room and hohlraum when it is necessary to work in these areas. The purpose of this investigation is to determine: one, the effectiveness of the shutters in shielding the lattice room and hohlraum; two, how many thermal neutrons are lost due to leakage out the edges of the one foot gap.

The shielding effect of the shutters was determined experimentally, and is discussed in Appendix C.

Since the one foot gap is essentially a cavity, it is felt that the model discussed in Chapter 1 can be used to determine how many neutrons are lost through the sides, and the effect of putting a graphite lining on these edges. The model of the lead shutter region used in these calculations is shown in figures 3.4 and 3.5. Figure 3.4 shows the relationship between the faces for the present situation, and figure 3.5 shows the case of a 12 inch graphite lining on the edges of the cavity

For both cases the source on face one is taken as

$$\text{Source} = \frac{S}{4}\left[\frac{\pi}{86.10\text{in.}}\right]^2 \cos\left[\frac{\pi x}{86.10\text{in.}}\right]\cos\left[\frac{\pi y}{86.10\text{in.}}\right] \qquad (3.1)$$

where S = total number of neutrons/sec emitted by the source

x and y are the vertical and horizontal distances respectively from the center of face one to the position (x,y) on face one.

Thus, the source in neutrons/cm^2·sec for a subarea with a side of length L is

$$\text{Source (subarea)} = \frac{S}{4L^2}\left[\frac{\pi}{86.10\text{in.}}\right]^2 X \int_{\text{subarea}} \cos\left(\frac{\pi x}{86.10\text{in.}}\right)\cos\left(\frac{\pi y}{86.10\text{in.}}\right)dxdy \,. \qquad (3.2)$$

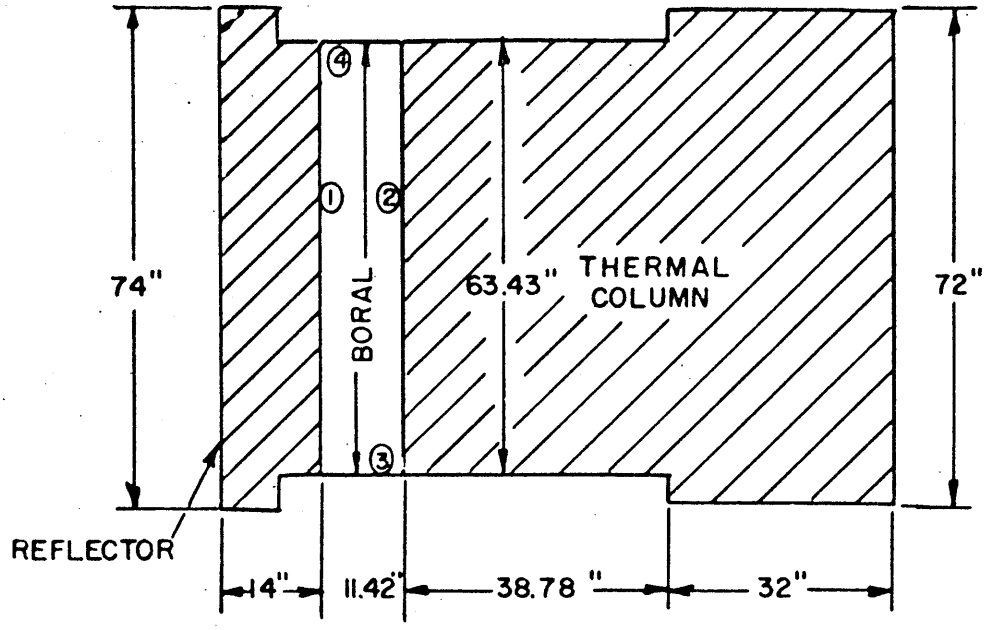

TOP VIEW

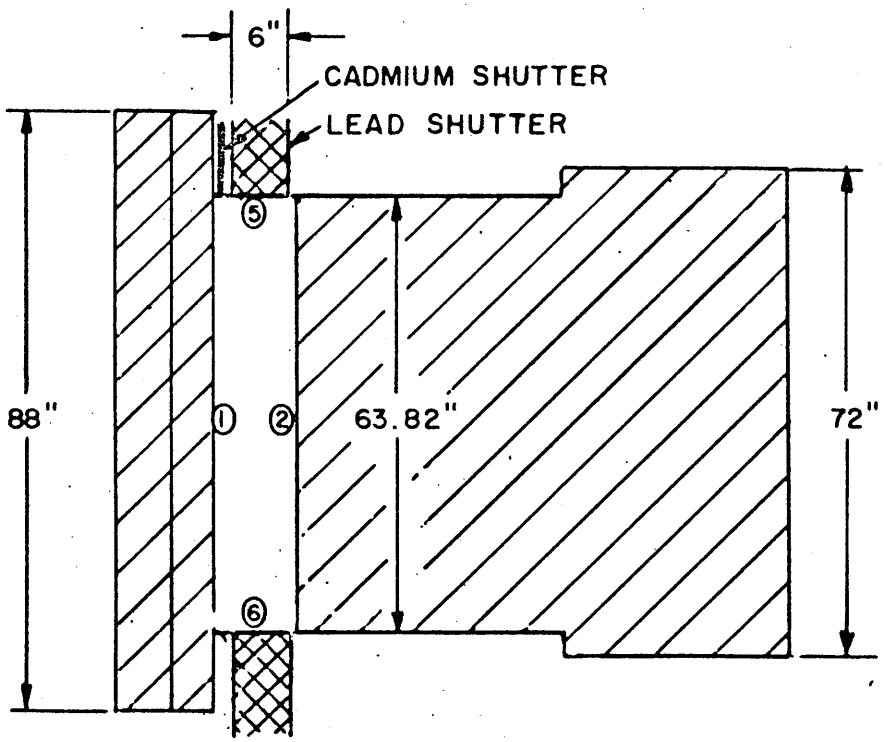

SIDE VIEW

FIG. 3.4 LEAD SHUTTER, NO LINING

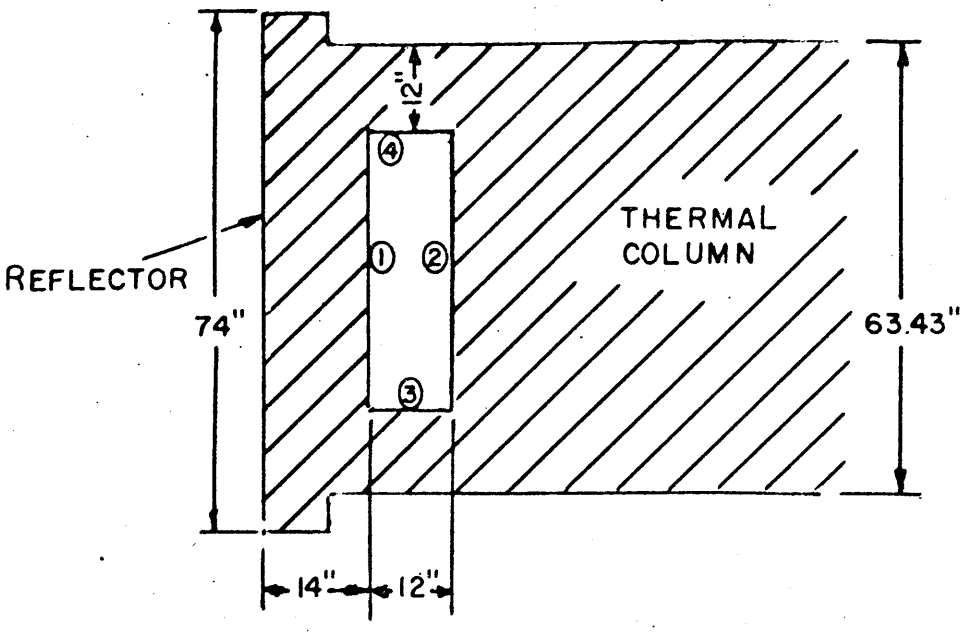

TOP VIEW

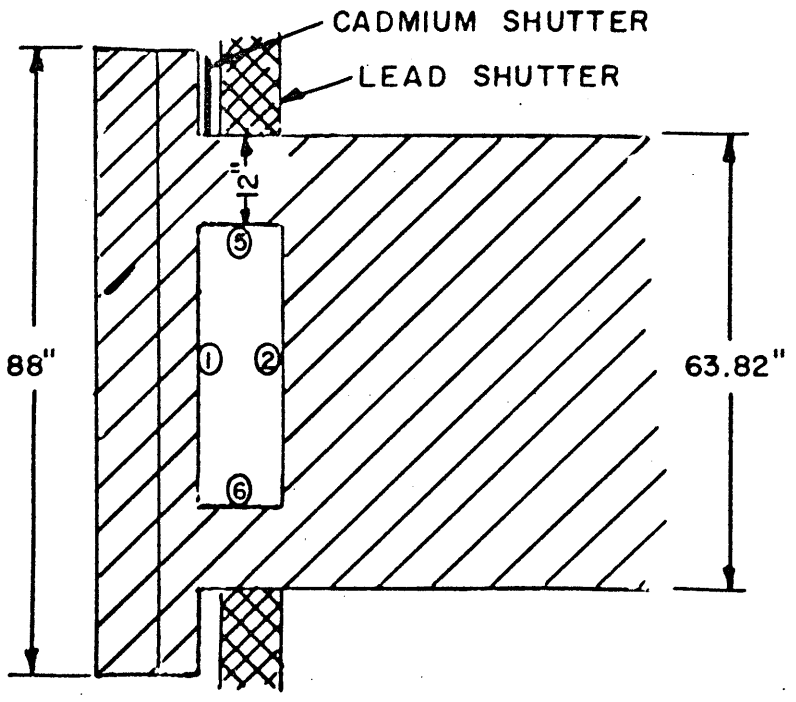

SIDE VIEW

FIG. 3.5 LEAD SHUTTER, 12 inch LINING

For the case of no lining L is taken as 6.333 inches, and for the case of 12 inch lining, L is taken as 3.911 inches.

In the case of no lining, two edges of the cavity are a combination of air, cadmium, and lead. In determining the albedo for a subarea on one of these faces, air and cadmium are assumed to have albedoes of zero; therefore, the albedo of the subarea is the albedo of lead weighted by its area fraction. The albedo for lead has been estimated using diffusion theory.

The other two edges of the cavity are boral. The albedos for these edges are taken from Madell's thesis.

Shown in figure 3.6 is a plot of the centerline flux across face 2 (the face of the thermal column). The upper curve is the case of a 12 inch graphite lining on the edges of the cavity, and the lower curve is the case of no lining. The lining reduces the size of the cavity and the number of neutrons entering it; however, the increase in albedo of the edges is so great that there is a net increase in flux on the thermal column face.

With no lining it is found that 68.7% of the neutrons which enter the cavity are lost through the edges and 20.6% are available for diffusion down the thermal column. The remaining 10.7% are reflected back into the reflector of the reactor. Heimberg analysed the same problem with a Monte Carlo calculation and found that 29.3% of the neutrons entering the cavity were available to the thermal column. The difference between his value and the value of 20.6% found by this model is due to the fact that he used lead on all four

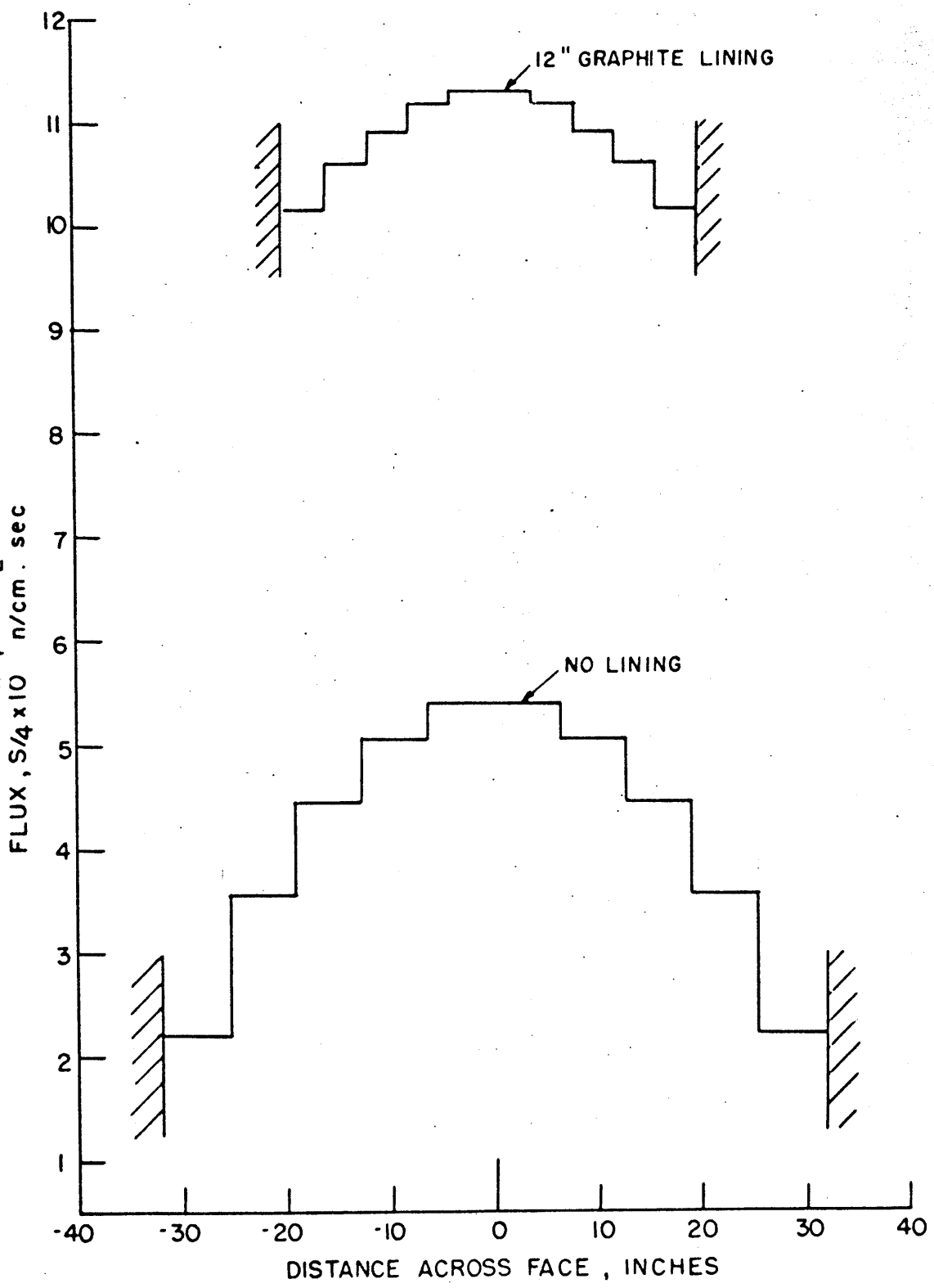

FIG. 3.6 FLUX ACROSS CENTERLINE OF THERMAL COLUMN FACE

edges of the cavity rather than boral on two edges and a mixture of lead, air, and cadmium on the other two edges. To determine the effect of doing this, the problem was recalculated by the view factor method using lead on all four edges. The number of neutrons available to the thermal column was found to be 30.5% which is in good agreement with Heimberg's value of 29.3%.

With the 12 inch graphite lining on the edges it is found that the leakage through these edges is reduced to 43.3% and the number of neutrons available to the thermal column increased to 28%. This fact along with the results of the experimental investigation of the shielding effects of the lead shutter (Appendix C) indicate that it may be advantageous to eliminate the lead shutters and line the edges of the one foot cavity with graphite. The optimum thickness of this lining is discussed in the next chapter. A small gap will still have to be left for the cadmium shutter, and provisions made for the insertion of a temporary lead shield wherever it is necessary to work in the hohlraum region.

Chapter 4

Optimization of Thermal Column

4.1 Empty Cavity

Shown in figure 4.1 is the thermal column with the proposed cavity as described in section 2.1. Face 1 is the edge of the graphite reflector surrounding the reactor and is the source of neutrons.

The aim of this section is to determine the wall thickness which will give the maximum thermal flux in the cavity. Increasing the wall thickness increases its albedo and reduces leakage from the cavity. From this it can be concluded that the maximum flux in the cavity will occur when the wall thickness is increased without limit. However, since the outside dimensions of the thermal column are fixed any increase in wall thickness has to be done on the inside of the cavity. This reduces the size of face 1 and the source of neutrons. Consequently it might be expected that an increase in wall thickness will result in a decrease in the flux in the cavity.

To determine the optimum wall thickness, the flux on face 2 has been calculated for four different wall thicknesses: zero inches, eight inches, 12 inches, and 16 inches. For each wall thickness, three end conditions have been used: (a) no end (face 2 albedo = 0), which gives the lowest possible flux; (b) infinite end (face 2 albedo = 1), which gives the highest possible flux; and (c) 32 inches of graphite, which is the actual situation.

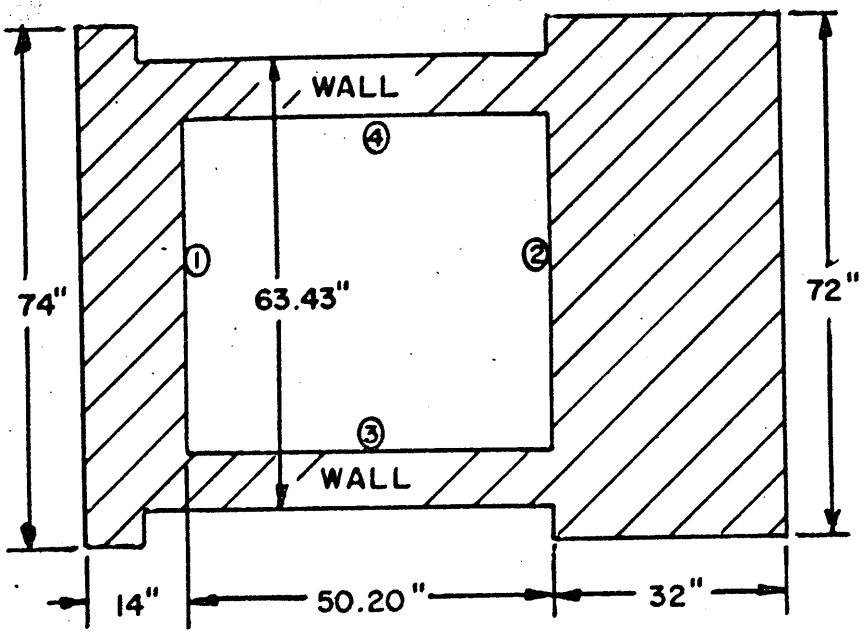

TOP VIEW

SIDE VIEW

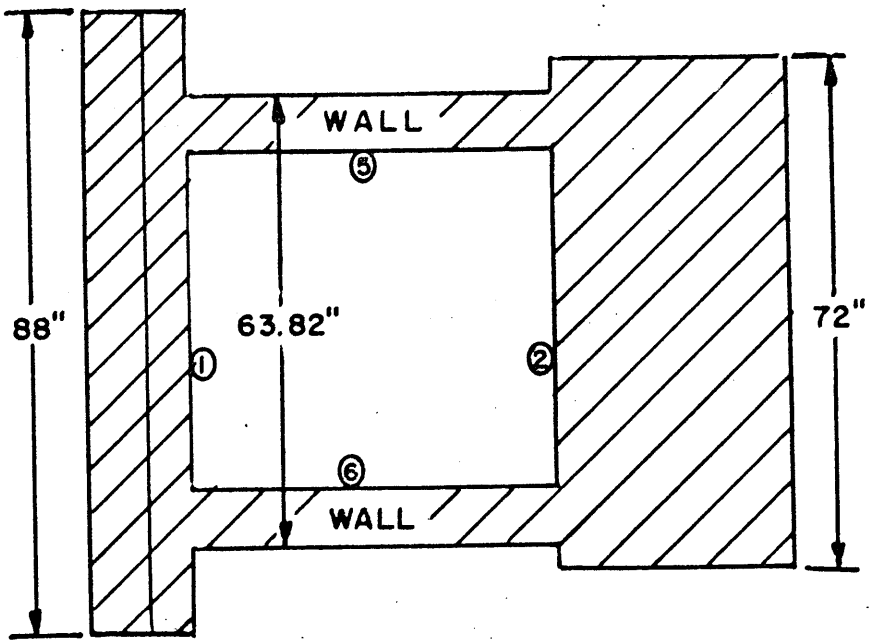

FIG. 4.1 MODIFIED THERMAL COLUMN

The source is the same as that used in the lead shutter problem, section 3.2. The subarea sizes used in the various cases are given in Table 4.1.

Table 4.1

Length of Subarea Edge

Wall Thickness, inches	L, inches
0	6.333
8	6.061
12	5.633
16	6.308

Shown in figure 4.2 is a plot of the flux on face two as a function of wall thickness and end condition. Shown is both the average flux and the peak flux. The curves have been normalized to the average flux for the case of no walls and no end. As is expected, for any wall thickness, the larger the albedo of face 2, the larger the flux. Also, the albedo of face 2 has a larger effect as the walls get thicker, because leakage out through the sides is smaller.

For the case of no end, the flux increases with wall thickness up to about 10 inches. At this point the reduction in source due to the reduction in cavity size becomes important and the curve begins to decrease slightly. For the cases of a 32 inch end and and infinite end, the flux continues to increase for wall thicknesses greater than 8 inches; however beyond 8 inches, the rate of increase drops off rapidly.

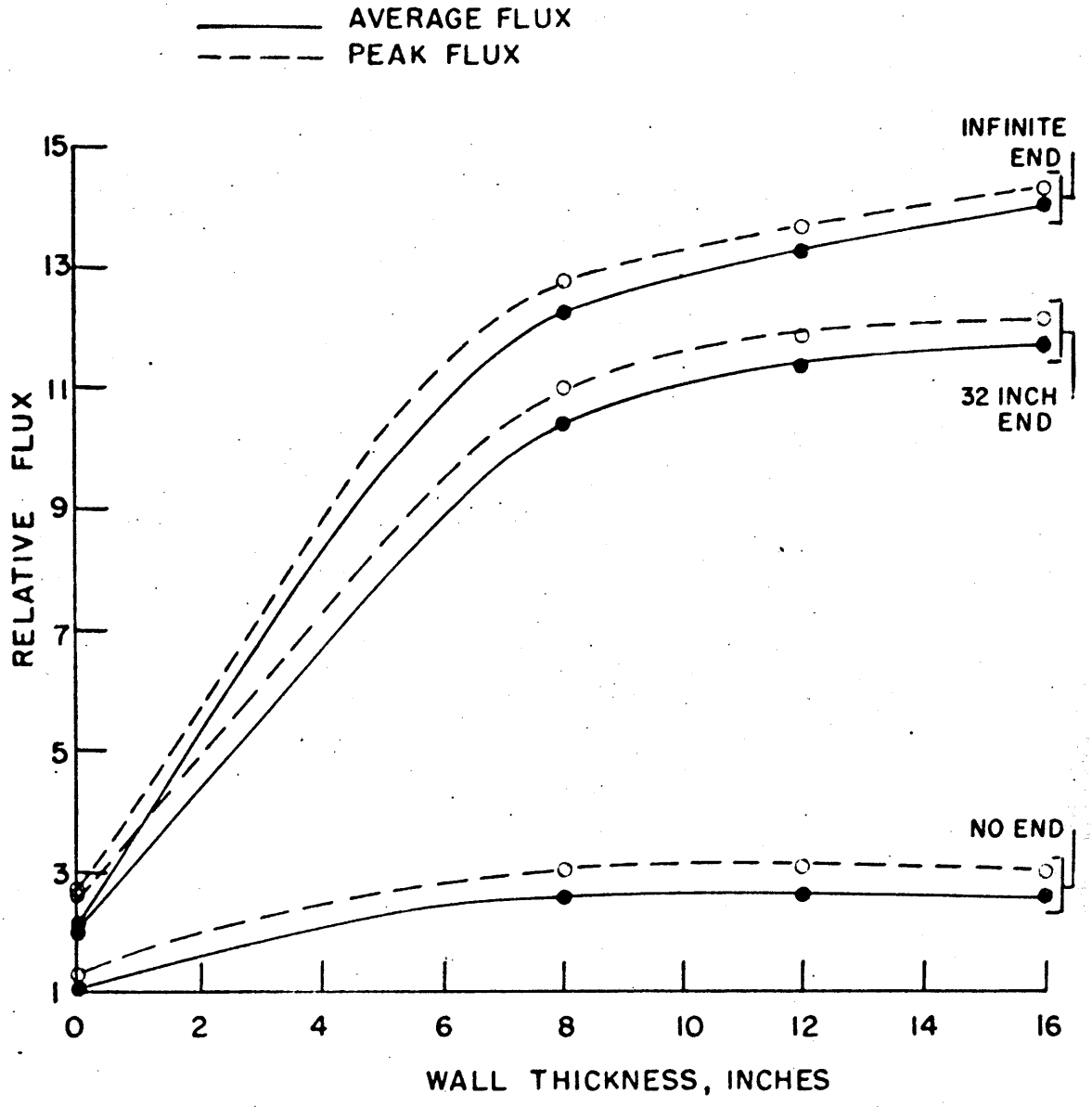

FIG. 4.2 FLUX ON FACE 2

Since it would be desirable to have as much space as possible for the location of a large cold neutron cryostat, the walls should be kept as thin as possible. Thus, it can be concluded that the optimum wall thickness is about 8 inches.

4.2 Comparison with a Solid Thermal Column

Since the object of the hohlraum is to increase the thermal flux in the thermal column, the flux calculated for face 2 should be compared with the flux at the same position in the present thermal column. The thermal column, shown in figure 3.4, can be considered in two sections. From diffusion theory, the flux for each section can be written as,

$$\phi_1 = A\cos\frac{\pi x}{\bar{a}}\cos\frac{\pi y}{\bar{b}}[\bar{e}^{\gamma_1 z}+K_1 e^{\gamma_1 z}], o<z<d \qquad (4.1)$$

$$\phi_2 = B\cos\frac{\pi x}{\bar{c}}\cos\frac{\pi y}{\bar{c}}\sinh\gamma_2(\bar{e}-z), \; d<z<e \qquad (4.2)$$

where $\bar{a}$ = extrapolated height of first section

$\bar{b}$ = extrapolated width of first section

d = length of first section

$\bar{c}$ = extrapolated height and width of second section

e = overall length of thermal column

$\bar{e}$ = extrapolated length of thermal column

$\gamma_1^2 = \frac{1}{L^2} + (\frac{\pi}{\bar{a}})^2 + (\frac{\pi}{\bar{b}})^2$

$\gamma_2^2 = \frac{1}{L^2} + 2(\frac{\pi}{\bar{c}})^2$.

A, B, and K_1 are constants determined from the boundry conditions,

$$\phi_1 = \phi_2 \text{ at } z = d \tag{4.3}$$

$$\frac{\partial \phi_1}{\partial \phi_z} = \frac{\partial \phi_2}{\partial z} \text{ at } z = d \tag{4.4}$$

$$\phi_1 = \phi_0 \text{ at } z = 0 \tag{4.5}$$

where ϕ_0 is the flux on the face of the thermal column calculated in the lead shutter problem, Section 3.2.

Applying these boundry conditions gives

$$K_1 = e^{-2\gamma_1 d}\left[\frac{\frac{\gamma_1}{\gamma_2}\text{Tanh}\gamma_2(\bar{e}-d)-1}{\frac{\gamma_1}{\gamma_2}\text{Tanh}\gamma_2(\bar{e}-d)+1}\right] \tag{4.6}$$

$$B = A\left(\frac{2}{\pi}\right)^2\left[\frac{e^{-\gamma_1 d}+K_1 e^{\gamma_1 d}}{\sinh\gamma_2(\bar{e}-d)}\right]\left[\frac{\sin(\bar{c}/\bar{a}-1)\pi/2}{\bar{c}/\bar{a}-1} + \frac{\sin(\bar{c}/\bar{a}+1)\pi/2}{\bar{c}/\bar{a}+1}\right] X\left[\frac{\sin(\bar{c}/\bar{b}-1)\pi/2}{\bar{c}/\bar{b}-1} + \frac{\sin(\bar{c}/\bar{b}+1)\pi/2}{\bar{c}/\bar{b}+1}\right]. \tag{4.7}$$

and

$$A = \left[\frac{4}{\pi^2(1+K_1)}\right]\sum_i \phi_i\left[\sin\frac{\pi Xai}{\bar{a}} - \sin\frac{\pi Xii}{\bar{a}}\right]\left[\sin\frac{\pi Yai}{\bar{b}} - \sin\frac{\pi Yii}{\bar{b}}\right] \tag{4.8}$$

where $\phi_i = \phi_o$ for the i^{th} subarea on the thermal column face

Xii, Yii = Lower limits of X and Y for i^{th} subarea

Xai, Yai = Upper limits of X and Y for i^{th} subarea.

Using, a = 63.82 inches

b = 63.43 inches

c = 72.00 inches

d = 38.78 inches

e = 70.78 inches

$\bar{a}$ = 65.24 inches

$\bar{b}$ = 64.85 inches

$\bar{c}$ = 73.42 inches

$\bar{e}$ = 71.49 inches

$L = 54.1cm.$

$\gamma_1 = 0.082885/in.$

$\gamma_2 = 0.076591/in.$

gives

$K_1 = 5.2975 \times 10^{-5}$

$A = S(1.6388 \times 10^{-4}) n/cm^2 \cdot sec$

$B = S(9.7303 \times 10^{-7}) n/cm^2 \cdot sec.$

where S is defined in Section 3.2.

Therefore, the flux in the thermal column can be written as,

$$\phi = S(1.6388 \times 10^{-4} \frac{n}{cm^2 \cdot sec}) \cos(\frac{\pi x}{65.24\ in}) \cos(\frac{\pi y}{64.85in}) X[e^{0.082885z} + 5.2975 \times 10^{-5} e^{0.082895z}], 0<z<38.78in$$

$$\phi = S(9.7303 \times 10^{-7} \frac{n}{cm^2 \cdot sec}) \cos(\frac{\pi x}{73.42in}) \cos(\frac{\pi y}{73.42in}) X \sinh[0.076591(71.49in - z)], 38.78in<z<70.78in \quad (4.9)$$

and the average flux at z = 38.78 inches as

$$\Phi = S(2.8775 \times 10^{-6}) n/cm^2 \cdot sec. \quad (4.10)$$

The average flux at the same position (Face 2) of a cavity having eight inch thick walls is

$$\Phi = S(9.3090 \times 10^{-5}) n/cm^2 \cdot sec; \quad (4.11)$$

thus, the hohlraum increases the flux in the thermal column by a factor of 32.35.

4.3 Effect of Coolant Pipes

It is proposed to locate the coolant pipes of the reactor in the region presently occupied by the lead shutters, as shown in figure 4.3.

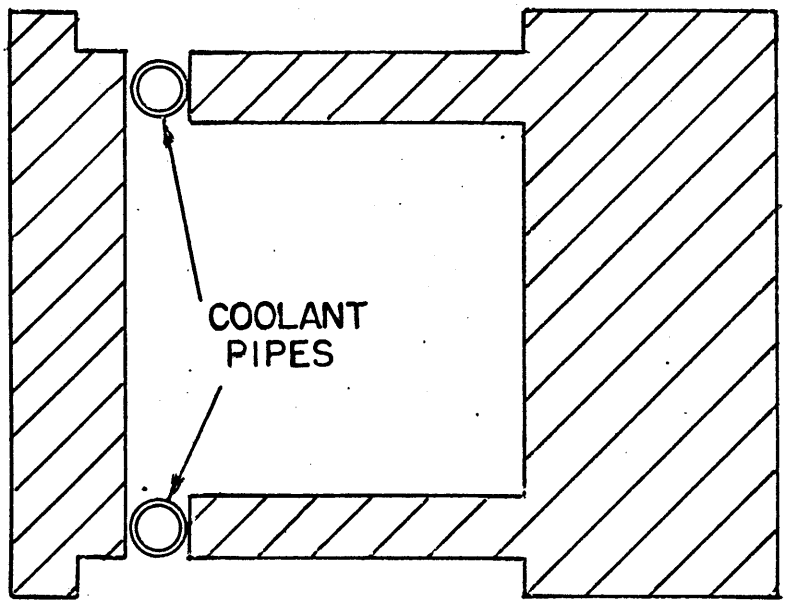

FIG. 4.3 LOCATION OF COOLANT PIPES

The pipes are eight inch diameter aluminum pipes and the coolant is light water.

The purpose of this section is to determine the effect of the pipes on the flux in the thermal column hohlraum.

To determine the effect of the coolant pipes it is necessary to know the combined albedo of the light water and the aluminum. The albedo of the water is taken as

$$Bw = \frac{1-2\frac{d}{L}\coth(t/L)}{1+2\frac{d}{L}\coth(t/L)} \qquad (4.12)$$

where D = diffusion Coefficient = 0.141cm

L = diffusion Length = 2.75 cm

t = thickness = 8 inches

the value of the water albedo becomes

Bw = 0.81398.

Since the aluminum pipe is thin, diffusion theory cannot be applied; however, the effect of the aluminum can be conservatively estimated by multiplying the albedo of the water by the factor

$$e^{-2\Sigma_t t} \qquad (4.13)$$

where Σ_t = total cross section = 0.09850/cm

t = pipe thickness = 5/16 inch.

Application of this factor reduces the albedo to 0.69615.

The case with 8 inch thick walls and a 32 inch thick end has been recalculated with the coolant pipes located as shown in figure 4.3. The average flux on face two has been found to be

$$\Phi = S(8.6986 \times 10^{-5}) n/cm^2 \cdot sec \qquad (4.14)$$

which is 6.55% lower than the case with no coolant pipes.

4.4 Plane Object in Cavity

Up to this point, the calculations involving the optimization of the thermal column have been limited to an empty cavity. In the real situation the cold neutron cryostat will be located in the cavity. The purpose of this section is to investigate the effect of an object in the hohlraum on the flux in that region.

The model discussed in Chapter 2, with some modifications, is applicable to the special case of a two dimensional object in a cavity. Although such a special case cannot give a true representation of the real situation, it can give in a simple manner some indication of how an object such as the cold neutron cryostat will affect the flux in the thermal column cavity.

The model used for analysing the plane object problem is illustrated in figure 4.4. The two dimensional plane object is oriented so that its faces are towards face 1 of cavity 1 and face 2 of cavity 2. The original, empty, cavity is divided into two cavities, the dividing plane being the one containing the two dimensional object. The fluxes on the surfaces of the cavities are calculated as follows.

The subareas on face 2 of cavity 1 that are covered by the plane object are assigned albedos corresponding to the material of the object. The subareas not covered by the object are assigned fictitious albedos. With a source of neutrons at face 1, the fluxes on the surfaces of cavity 1 are calculated

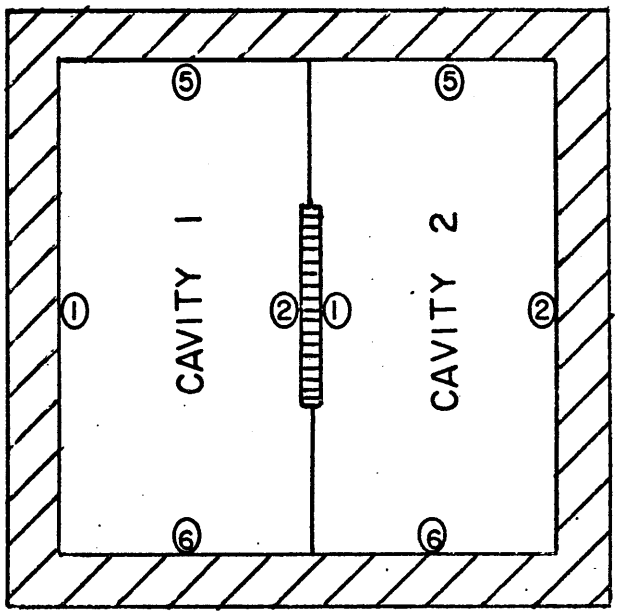

FIG. 4.4 PLANE OBJECT IN CAVITY

by the method described in Chapter 2.

Next the subareas on face 1 of cavity 2 that are covered by the plane object are assigned albedos corresponding to the material of the object, and the subareas that are not covered are assigned albedos of zero. Fictitious values are not used because neutrons incident on these subareas must be reflected in cavity 1 before they can re-enter cavity 2. However, this is the current incident on the part of face 2 cavity 1 that is not covered by the object and is taken as the source for cavity 2,

$$SOM(J1,K1,2) = GM2(J2,K2,1) \tag{4.15}$$

where, SOM(J1,K1,2) = Source for a subarea located at (J1,K1) on face 1 of cavity 2.

GM2(J2,K2,1) = Current incident on a subarea located at (J2,K2) on face 2 of cavity 1.

J2 = J1, excluding area covered by object

K2 = K1, excluding area covered by object.

With this source the fluxes on the surfaces of cavity 2 are calculated, again using the method of Chapter 2.

New fictitious albedos for face 2 of cavity 1 are then calculated using

$$BM2(J2,K2,1) = \frac{GM1(J1,K1,2)}{GM2(J2,K2,1)} \tag{4.16}$$

where BM2(J2,K2,1) = Albedo for a subarea located at (J2,K2) on face 2 of cavity 1

GM1(J1,K1,2) = Current incident on a subarea located on face 1 of cavity 2

GM2(J2,K2,1) = Current incident on a subarea located at (J2,K2) on face 2 of cavity 1.

J2 = J1, excluding area covered by object

K2 = K1, excluding area covered by object.

Using the new fictitious albedos, the above procedure is repeated until the solution converges. This iterative technique is carried out on a digital computer using the program TARGET, which is a modification to the program HOLCAV. TARGET is described in Appendix B.

In carrying out the calculations, two limiting cases are considered: (1) a purely reflecting object, albedo = 1; and (2) a purely absorbing object, albedo = 0. For both cases the walls of the cavity are taken as eight inches thick, the end as 32 inches thick, and the source the same as that used in the lead shutter problem, Section 3.2.

Shown in figure 4.5 is a plot of the fluxes on the surfaces of the object as a function of the object size. For each case three curves are shown: (1) the flux on the front surface (facing the source),(2) the flux on the back surface (away from the source), and (3) the average flux for both surfaces.

In general the results are as expected. Introduction of the object into the cavity causes the flux to become asymmetric; that is, the flux is higher on the face towards the source than on the face away from the source. This asymmetry becomes greater as the object gets larger because increasing the size of the object reduces the number of neutrons reaching cavity 2, and consequently the flux on the face away from the source.

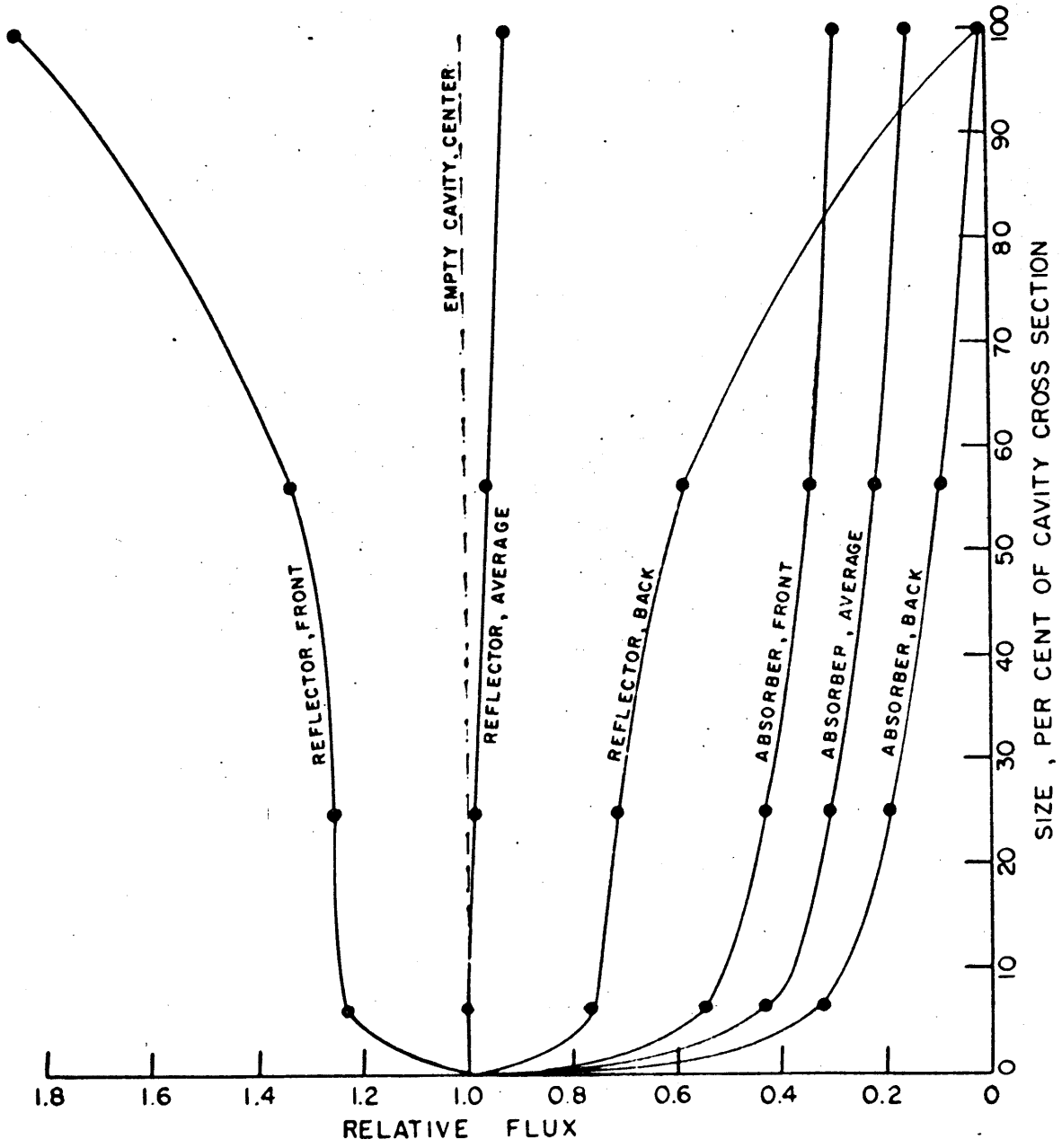

FIG. 4.5 FLUX ON SURFACE OF PLANE OBJECT

Also, for the absorber the flux decreases monotonically with increasing size.

Probably the most interesting result is that for a reflector the average flux drops less than 10% as the object size increases from zero to 100% of the cross sectional area of the cavity. Since the cold moderator will be heavy water which is a good scatterer, it will behave similarly to the reflector. This means that for a fixed wall thickness changing the size of the cold moderator will have little effect on the number of neutrons available for slowing down, but will affect the position at which they enter the cold neutron source.

4.5. Effect on Lattice Facility

As shown in figure 2.1, the lattice facility hohlraum is located at the end of the thermal column. Because of the nature of the experiments carried out in the lattice facility, it is necessary that the cadmium ratio in the hohlraum be maintained as high as possible. Since removing graphite from the thermal column reduces the amount of moderator between the core and the hohlraum, it might be expected that the cadmium ratio in this region will be reduced. The purpose of this section is to investigate the effect of the proposed thermal column cavity on the cadmium ratio in the lattice facility hohlraum.

Consider an infinite slab of graphite. From diffusion theory, the epithermal and thermal fluxes in the slab can be

written as

$$\phi_E = \phi_{EO} e^{-\gamma_E z}, \tag{4.17}$$

$$\phi_T = \phi_{TO} e^{-\gamma_T z}, \tag{4.18}$$

where

ϕ_{EO} = epithermal flux at z = o

ϕ_{TO} = thermal flux at z = o

γ_E = epithermal attenuation length

γ_T = thermal attenuation length.

Writing the cadmium ratio as

$$CR = 1 + \frac{\phi_T}{\phi_E} \tag{4.19}$$

gives

$$CR(z) = 1 + \frac{\phi_{TO}}{\phi_{EO}} e^{\lambda z} \tag{4.20}$$

or

$$[CR(z)-1] = [CR_o-1]e^{\lambda z} \tag{4.21}$$

where $\lambda = \gamma_T - \gamma_E$

CR_o = cadmium ratio at z = o.

In general, λ can be determined from the neutron diffusion properties of graphite; however, it is felt that a more accurate estimate of the effect of the proposed cavity can be obtained by evaluating λ from existing data for the present thermal column. These data are listed in Table 4.2. The cadmium ratio at z = 26 inches has been measured as part of this work and is discussed in Appendix D. Using these values, λ is found to be 0.046488/in.

Table 4.2

Measured Cadmium Ratios

z, inches	CR	Foil
0(core tank)	34(6)	Au, $\frac{1}{16}$" dia., 10 mils thick
26	111	Al-Au(0.072%), 30 mils dia., $\frac{1}{8}$" thick
84.78	1700(7)	Au, $\frac{1}{8}$" dia., 10 mils thick

Since the graphite will be removed from the thermal column in conjunction with the installation of the new reactor core, it is necessary to know CR_o for the new core. From Andrews Addae's (8) calculations this has been estimated to be 55. With the cavity in the thermal column, there will be 46 inches of graphite between the core tank and the lattice facility hohlraum. Using these values gives a cadmium ratio of 459 which is a factor of 3.7 lower than the present value; however, the new value is sufficiently high for the experiments carried out in the lattice facility (9).

Another concern is the thermal flux available to the lattice facility hohlraum when the cold neutron cryostat is located in the thermal column cavity. The cold moderator will be a sphere of D_2O ice on the order of one foot in diameter; thus, it will occupy about 5% of the cross sectional area of the cavity. As part of the work discussed in Section 4.4 the thermal flux has been calculated at the hohlraum end of the cavity for the case of an object occupying 6.25% of the cross

sectional area. The average thermal flux has been found to be

$$\Phi = S(9.1811 \times 10^{-5}) n/cm^2 \cdot sec \qquad (4.22)$$

which is 32 times higher than the flux at the same position in a solid thermal column, and is the same as that found for an empty cavity. Thus, it is concluded that the cold moderator will not greatly affect the thermal flux available to the lattice facility.

4.6. Summary

It has been found that the thermal neutron flux in the thermal column can be greatly enhanced by removing graphite from the thermal column; thus, creating a cavity with graphite walls. The flux increases with wall thickness; however, beyond a thickness of eight inches the per cent increase drops off. Since it is desirable to have as much space as possible for the location of the cold neutron source, the optimum wall thickness is taken as eight inches.

In the ideal case of an empty cavity with no absorbers in the walls, the thermal flux is increased by a factor of 32 over that of a solid thermal column. In the real case, with the light water coolant pipes located in the walls of the cavity, the gain is reduced to a factor of 30.

The effect of the cold neutron source on the flux has been investigated with the simple model of a plane reflecting object in the cavity. It has been found that the cold moderator will not greatly affect the magnitude of the flux incident on

it, but will cause an asymmetry in the flux distribution. The flux incident on the surface of the cold moderator facing the reactor will be on the order of 60% higher than the flux incident on the surface facing away from the reactor.

The effect of the cavity and cold moderator on the flux available to the lattice facility has also been investigated. It has been found that the cadmium ratio in the lattice facility will be reduced from its present value of 1700 to a value of about 460. This latter value is expected to be high enough for the experiments carried out in the lattice facility. It has also been found that placing the cold moderator in the cavity will not reduce the thermal flux available to the lattice facility.

In the optimization of the thermal column the diffusion of neutrons through the walls of the cavity has been neglected. Considering the wall to be a slab of graphite eight inches thick and approximately 50 inches wide, the attenuation length is found to be 2.5 inches. Thus, approximately 90% of the neutrons which enter the wall are absorbed or leak out within a distance equal to the length of a subarea (about 6 inches). Therefore, the number of neutrons reaching the end of the cavity due to diffusion through the walls is negligible.

Chapter 5

Cold Neutron Cryostat

5.1. Description of Cryostat

The present cold neutron cryostat is located in a 14 inch diameter hole in the thermal column, as shown in figure 5.1.

The upper 60 inches of the assembly is a magnetite shield block which is shown in detail in figure 5.2. The helium supply and return lines are one inch diameter stainless steel tubes located in $2\frac{1}{2}$ inch diameter pipes. The outer pipes act as vacuum pump lines for the cryostat and as vacuum insulation for the helium lines. Located in the center of the shield block is a 3 inch diameter beam tube. In the upper part of the beam tube is a 29 inch long stainless steel shield plug with a one inch diameter hole along its axis. Positioned in the hole is a 58 inch long collimator, constructed of cadmium sheathed in aluminum. Also located in the shield block are four $\frac{1}{2}$ inch diameter instrumentation tubes.

The lower 79 inches of the assembly is the vacuum region of the cryostat and is shown in detail in figure 5.3. The vacuum jacket is a $13\frac{3}{4}$ inch diameter aluminum cylinder with a hemispherical end. The helium supply and return lines are one inch diameter aluminum tubes, supported from the shield plug by thin walled stainless steel tubes which also act as thermal insulation between the helium lines and shield plug. The

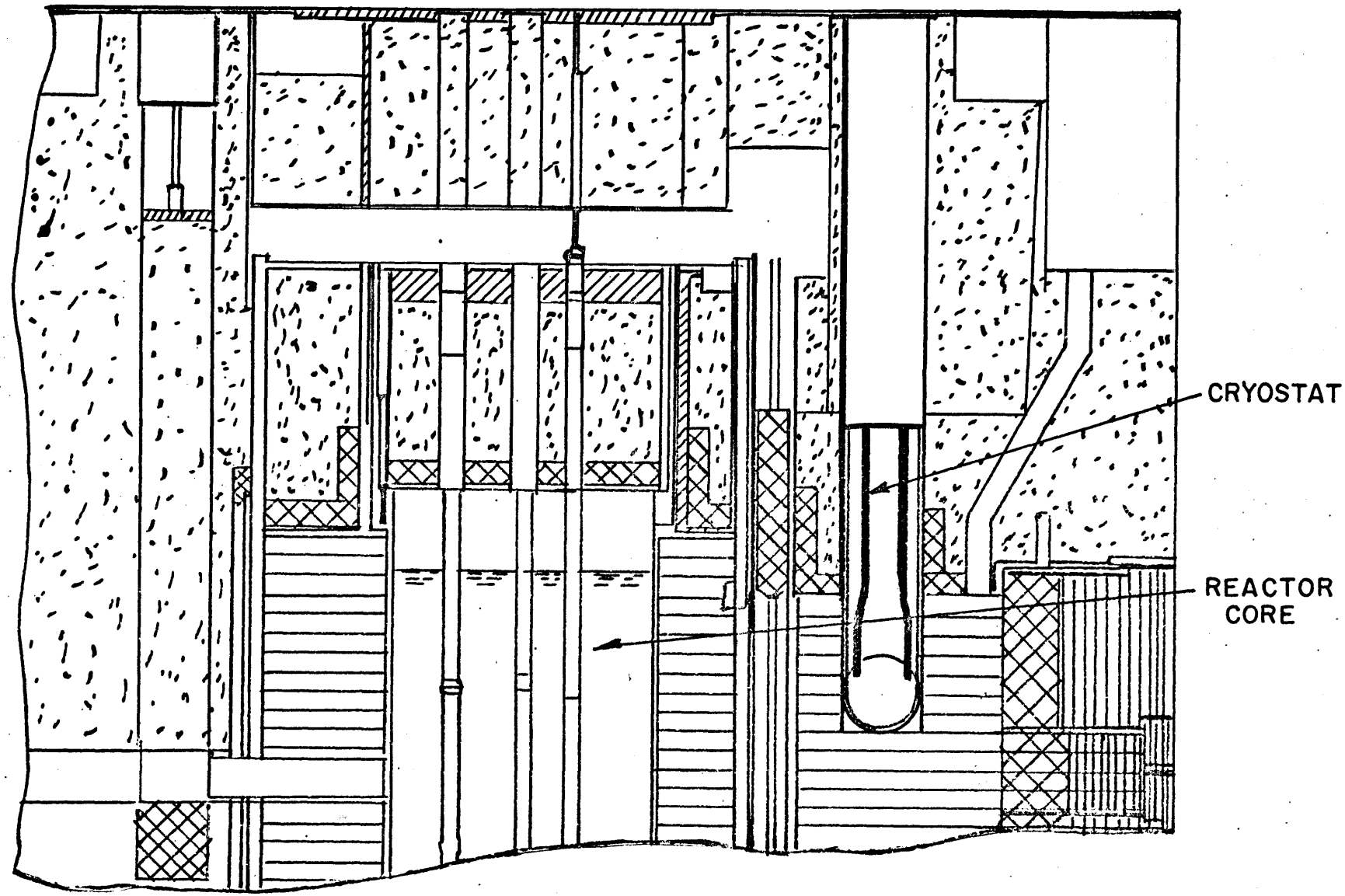

FIG. 5.1 COLD NEUTRON CRYOSTAT

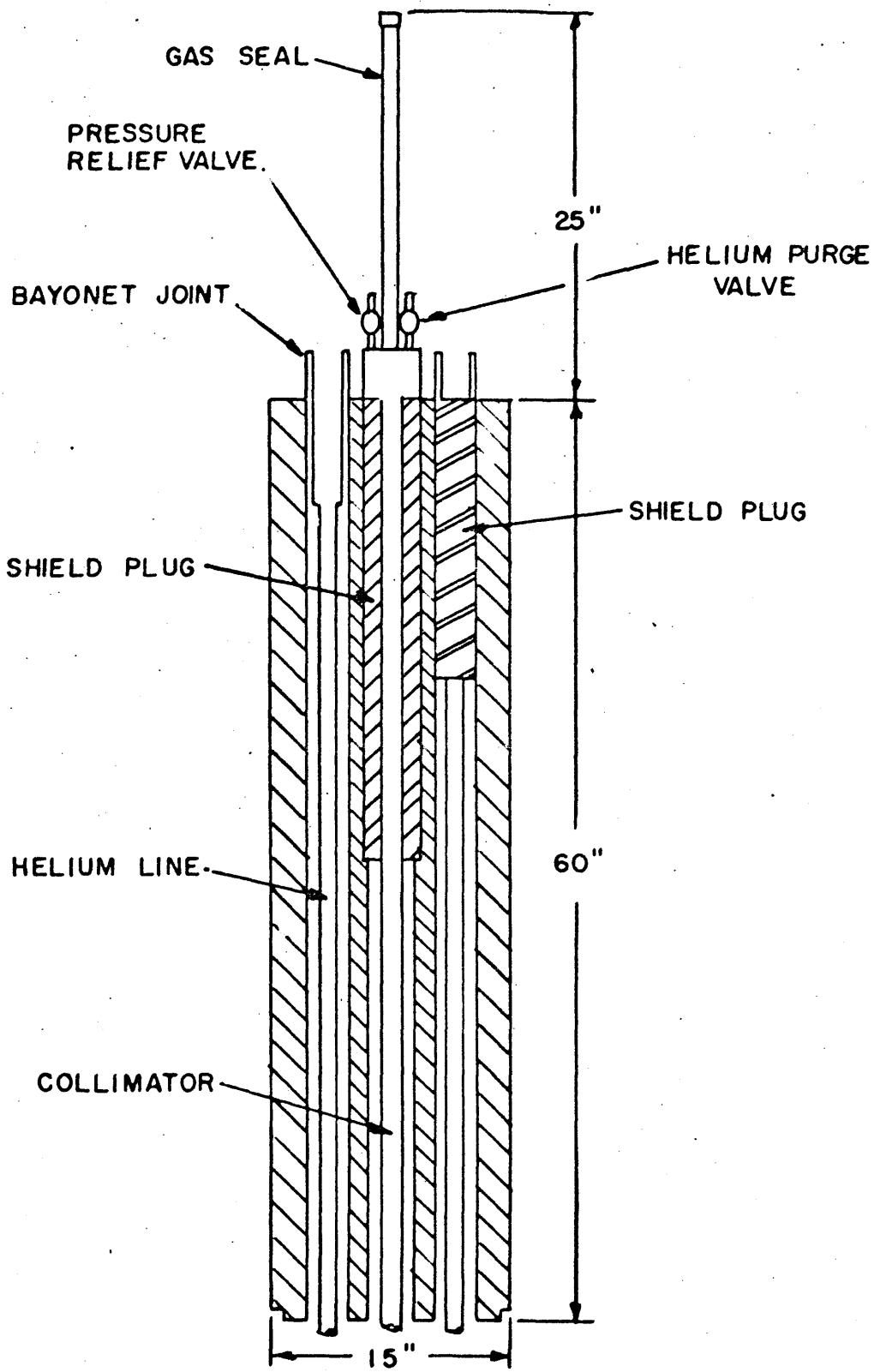

FIG. 5.2 UPPER SHIELD BLOCK

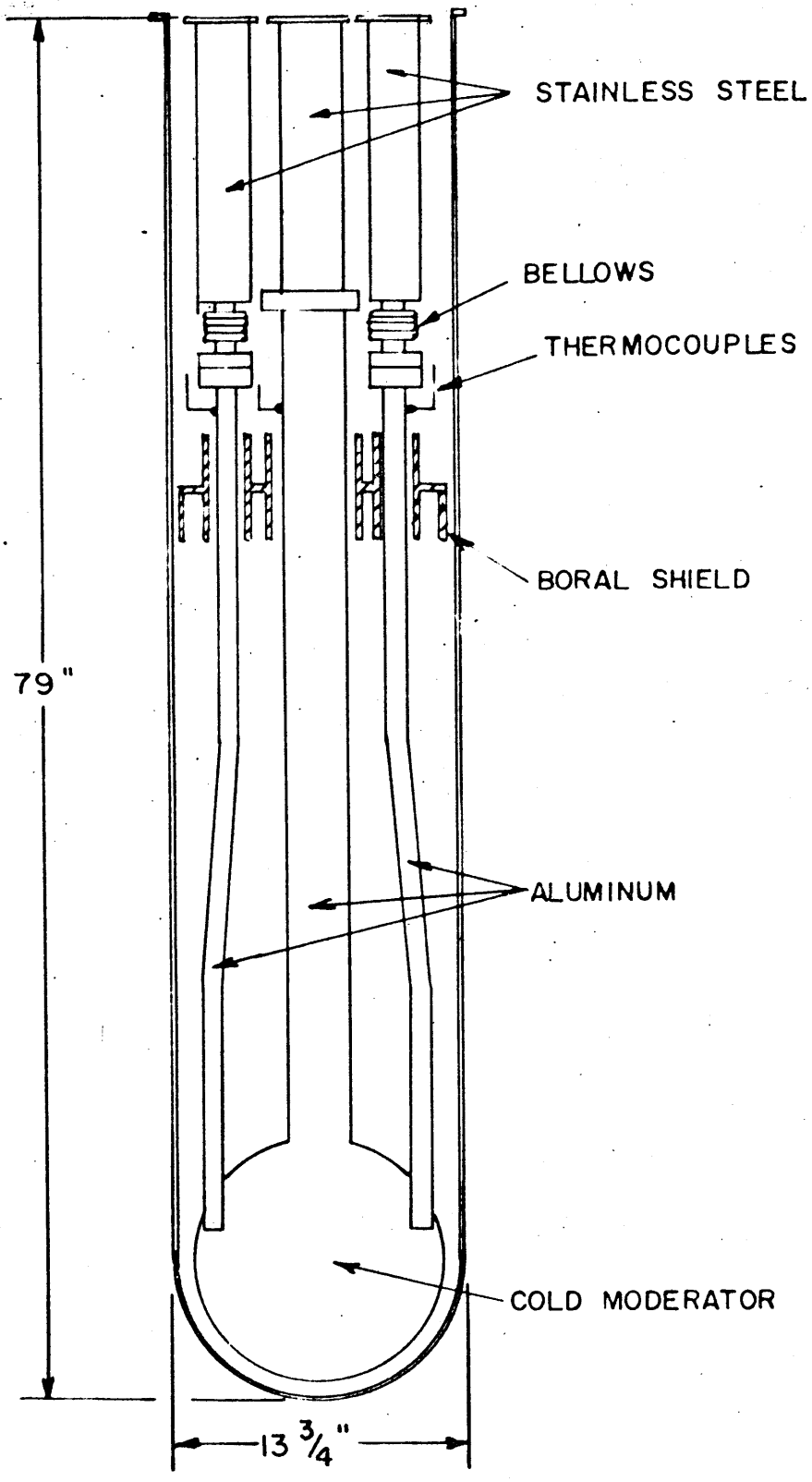

FIG. 5.3 VACUUM REGION

transition from stainless steel to aluminum helium lines is made through flanges with indium foil gaskets for seals. The temperatures of the helium lines are monitored with chromel-alumel thermocouples located near the upper ends of the aluminum sections. Stainless steel bellows compensate for the contraction of the lines during cool down.

The vertical beam port is a 3 inch diameter aluminum tube which supports the cold moderator. The upper $17\frac{1}{2}$ inch stainless steel section serves as thermal insulation between the shield block and cold moderator. The transition from stainless steel to aluminum is made with a flange and a silver plated stainless steel O-ring. The seal between the bottom of the shield plug and the stainless steel tube is made with a neoprene O-ring. The temperature of the beam tube is also monitored with a chromel-alumel thermocouple located near the upper end of the aluminum section.

Suspended approximately 30 inches below the bottom of the shield block is a boral shield which provides neutron shielding for the upper assembly.

The cold moderator is D_2O ice and is contained in a 12 inch diameter aluminum sphere shown in figure 5.4. Cooling for the cold moderator is provided by cold gaseous helium which passes through four $\frac{1}{4}$ inch diameter aluminum tubes. These tubes are wound in an 8 inch diameter spherically shaped coil. Three cold neutron beams are available from the cold moderator: one vertical beam, and two horizontal beams. The two horizontal beams are filtered through beryllium cylinders $1\frac{1}{2}$ inches

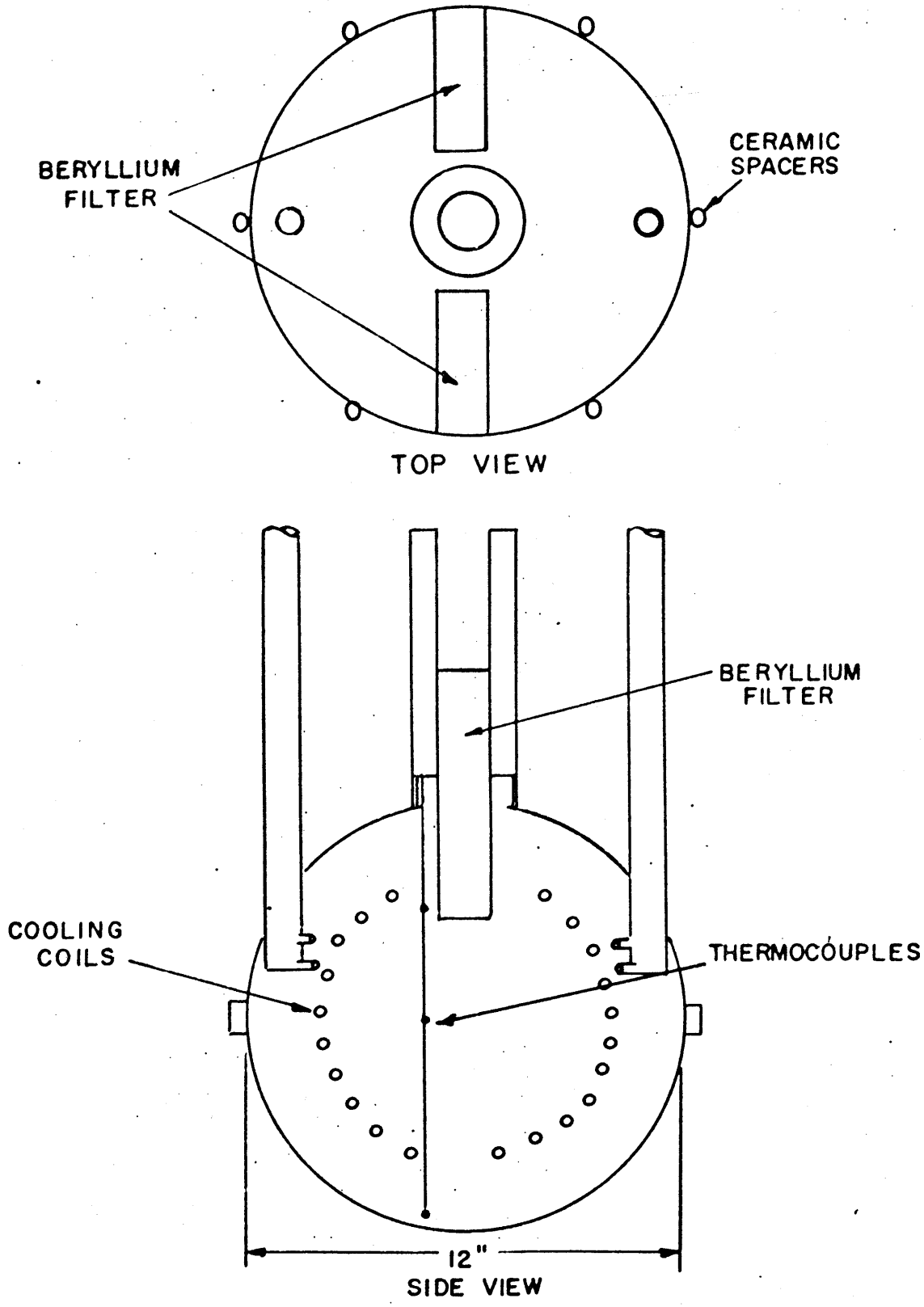

FIG. 5.4 COLD MODERATOR

in diameter and 4 inches long. These filters penetrate the cold moderator to a depth of 4 inches. The vertical beam is filtered through a beryllium filter $1\frac{1}{2}$ inches in diameter and 7 inches long. The penetration depth of this filter is adjustable. Six ceramic spacers prevent direct contact between the sphere and vacuum jacket.

The beryllium filter assembly for the vertical beam is shown in figure 5.5. The assembly is constructed of concentric aluminum cylinders. The outer cylinder is sized to fit the vertical beam tube and to seat on the small step in the beam tube just above the cold moderator. The inner cylinder contains a step on which the sleave around the beryllium filter seats. The penetration depth of the filter is adjusted by varying the length of the sleave. Three chromel-alumel thermocouples used to monitor the temperature of the cold moderator are supported by a small aluminum tube in the filter assembly.

The cooling helium for the cryostat is supplied by a helium liquifying plant (10). The layout of the helium transfer lines, designed by Ed Barnett, is shown in figure 5.6. Both the supply and return lines are vacuum insulated one inch diameter stainless steel tubes. Flexible sections in the lines allow for coupling and decoupling the lines from the cryostat, and for contraction of the lines during cool down. The lines are coupled to the cryostat through bayonet joints. A valving system located near the liquid helium dewar permits the directing of helium flow to either the cold neutron cryostat or the in-core cryostat(10).

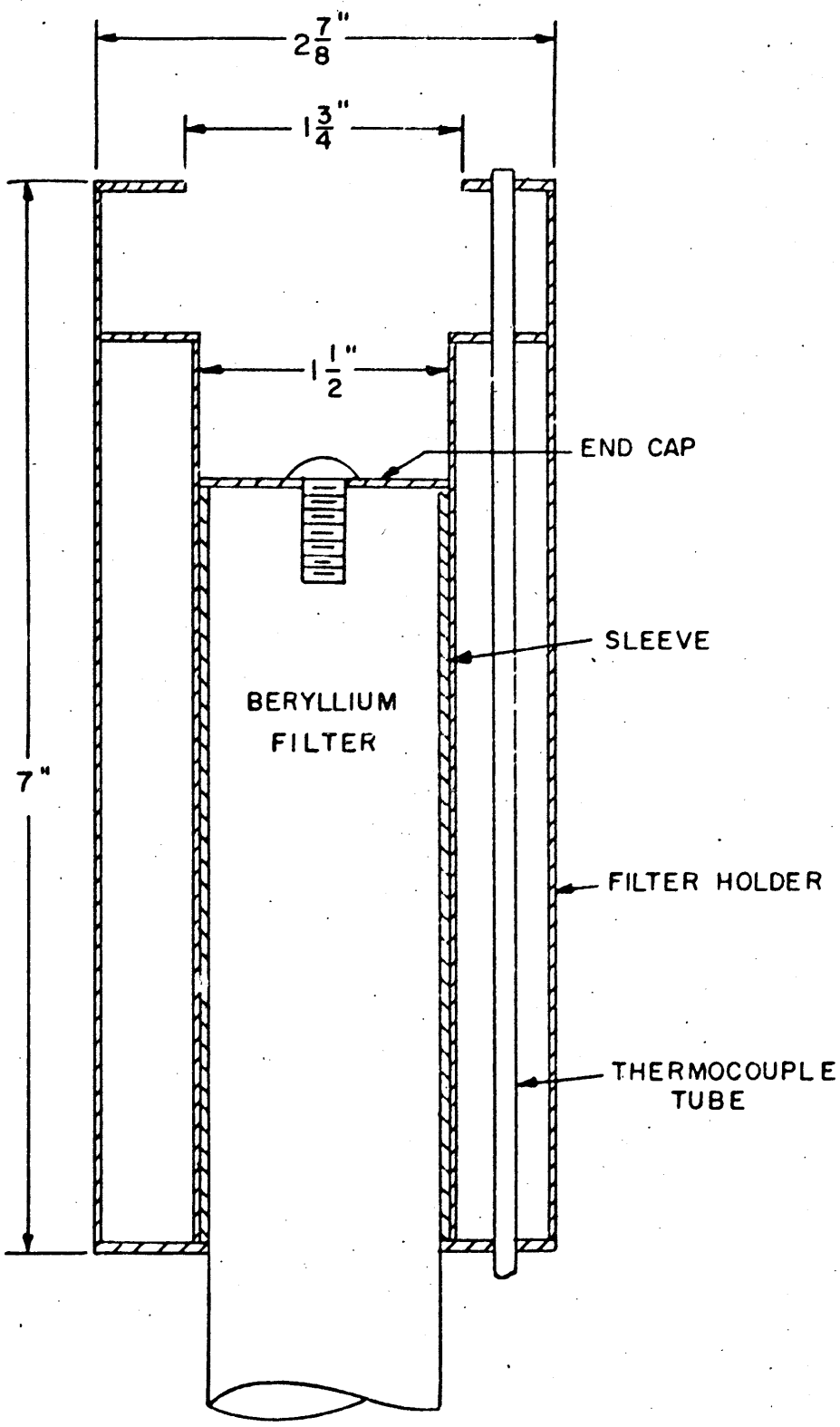

FIG. 5.5 BERYLLIUM FILTER ASSEMBLY

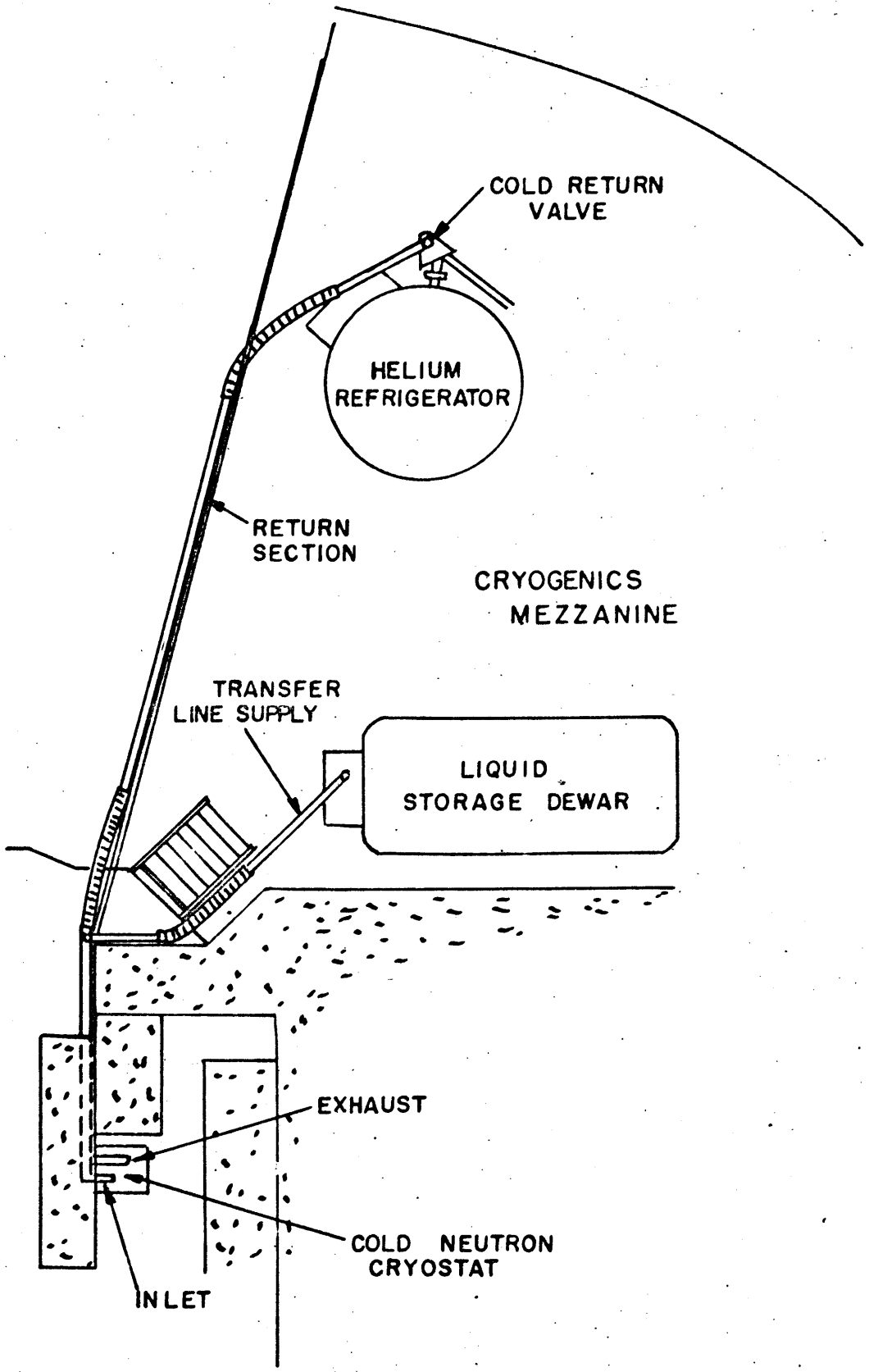

FIG. 5.6 HELIUM SUPPLY SYSTEM

5.2. Cryostat Heating

The cold moderator increases the number of cold neutrons by shifting the neutron spectrum to a lower temperature; consequently, one would like the temperature of the moderator to be as low as possible. Since the temperature to which the moderator can be cooled is limited by the amount of heat which must be removed by the coolant helium, one of the important considerations in the design of the cold neutron source is the total heat load generated in the cryostat.

In determining the total heat load the following sources of heat are considered: (1) heat generated in the moderator and structural parts due to core gamma rays, graphite capture gamma rays, fast neutrons, and cryostat gammas; (2) radiant heat transfer and free molecular conduction to the cold sphere, the helium lines, and the beam tube; (3) thermal conduction through supporting members to the helium lines and the beam tube. The calculation of the heat load is discussed in Appendix D and summarized in Table 5.1. As part of this work the thermal flux and cadmium ratio in the thermal column have been measured. A discussion of the measurements is given in Appendix D.

The total heat load in the cryostat is 111.6 watts. The expected output of the helium liquifying plant is 100 liters of liquid helium per hour or 27.55 lbm/hr. (18). The temperature rise of the coolant helium is given by

Table 5.1

Cryostat Heat Load

Watts

	Core Gammas	Graphite Gammas	Fast Neutrons	Cryostat Gammas	Radiant Heat Tran.	Free Mol. Conduction at 10^{-4} Torr	Thermal Conduc-tion	Total
He Supply Line	0.786	0.001	———	0.001	5.070	0.011	1.247	7.116
He Return Line	0.786	0.001	———	0.001	5.070	0.011	1.222	7.091
Beam Tube	3.943	0.003	———	0.005	14.552	0.027	4.038	22.568
Aluminum Sphere	5.055	0.004	———	0.006	9.869	0.022	———	14.956
Cooling Coils	0.878	0.001	———	0.001	———	———	———	0.880
D_2O Ice	58.832	0.040	0.098	0.004	———	———	———	58.974
							Total	111.585

$$\Delta T = \frac{Q}{\dot{M}\, C_p} \tag{5.1}$$

where, Q = total heat load = 111.6 watts

$\dot{M}$ = mass flow rate = 27.55 lbm/hr

C_p = specific heat = 1.25 Btu/lbm · °R.

Using these values gives

ΔT = 6.142 °K.

Since the effectiveness of the cold neutron source is dependent on the temperature of the cold moderator, it is important to know the temperature distribution in the D_2O ice. The temperature rise between the helium and the ice is given by

$$T = \frac{Q}{Ai}\left[\frac{r_i}{k_A}\ln\left(1+\frac{t}{r_i}\right)+\frac{1}{h}\right] \tag{5.2}$$

where, Q = total heat load on cooling coils

A_i = inside surface area of coils

= 214.1 square inches

r_i = inside radius of coils = 0.1363 inches

t = wall thickness of coils = 0.020 inches

k_A = thermal conductivity of aluminum

= 128 Btu/hr · ft · °R

h = heat transfer coefficient and is given by

$$h = 0.023\left(\frac{k_H}{2r_i}\right)\left[\frac{2\dot{m}}{\pi r_i \mu_H}\right]^{0.8}(Pr)_H^{0.4} \tag{5.3}$$

with, k_H = thermal conductivity of helium

= 0.0158 Btu/hr·ft·°R

μ_H = viscosity of helium = 0.00891 lbm/ft·hr .

Pr = Prandtl number of helium = 0.72

$\dot{m}$ = mass flow rate for one coil = 6.89 lbm/hr.

By using these values, h becomes

$$h = 72 \text{ Btu/hr}\cdot\text{ft}^2\cdot{}^\circ\text{R}.$$

The heat load on the coils is the total heat load on the cryostat minus the heat load on the supply and return lines; or 97.4 watts. Thus, the temperature rise between the helium and ice is

$$\Delta T = 1.726\ {}^\circ\text{K}.$$

The temperature at a radius r in the ice is given by

$$T = T_c + \frac{q''' a^2}{6k}\left[1-\left(\frac{r}{a}\right)^2\right], \quad 0<r<a \tag{5.4}$$

$$T = T_c + \frac{\left(1-\frac{a}{r}\right)}{\left(1-\frac{a}{b}\right)}\left\{(T_1-T_c) + \frac{q''' b^2}{6k}\left[1-\left(\frac{a}{b}\right)^2\right]\right\} + \frac{q''' a^2}{6k}\left[1-\left(\frac{r}{a}\right)^2\right], \quad a<r<b \tag{5.5}$$

where T_c = Ice temperature at coils

q''' = volumetric heat generation in ice, taken as constant.

a = radius of coils = 4 inches

k = thermal conductivity of ice = $1.28 \frac{\text{Btu}}{\text{hr}\cdot\text{ft}\cdot{}^\circ\text{R}}$

b = radius of sphere = 6 inches

T_1 = temperature at surface of sphere and is given by

$$(T_1-T_c) + \frac{q''' b^2\left(1-\frac{a}{b}\right)}{6k}\left[1+\frac{a}{b} - \frac{2b}{a}\right] = \frac{\sigma A_3 F_{31} b^2\left(1-\frac{a}{b}\right)}{A_1 ka}\left[T_3{}^4-T_1{}^4\right] \tag{5.6}$$

with A_3 = surface area of vacuum jacket

F_{31} = view factor from vacuum jacket to sphere

σ = Stefan-Boltzman constant

T_3 = Temperature of vacuum jacket = 343°K.

The inlet temperature of the coolant helium is expected to be about 20°K. The temperature rise between the helium and the ice is approximately 2°K; therefore, T_c has been estimated to be 22°K. The volumetric heat generation is calculated from Appendix D to be 65.18 milliwatt per cubic inch. By using these values and equation (5.6) the surface temperature of the sphere is calculated to be about 26°K.

A plot of the temperature distribution in the D_2O ice is shown in figure 5.7. Shown are the case for: 1. cooling at the surface of the sphere, 2. cooling with the coils at r = 4 inches, and 3. cooling with the coils at r = 3 inches. As can be seen, the case for cooling at r = 4 inches gives the most uniform ice temperature with a maximum ΔT of about 4°K.

5.3. Helium Pressure Drop

Another important consideration in the design of the cold neutron source is the coolant helium pressure drop across the cryostat. Under normal operating conditions, the liquid helium from the helium refrigerator is used to cool the in-core cryostat. The helium discharged from this cryostat is cold gas expected to be at a temperature between 10 and 20 degrees Kelvin. This gas is then used to cool the cold neutron cryostat before returning to the helium liquifying plant. With this in mind the cold neutron cryostat has been designed to operate

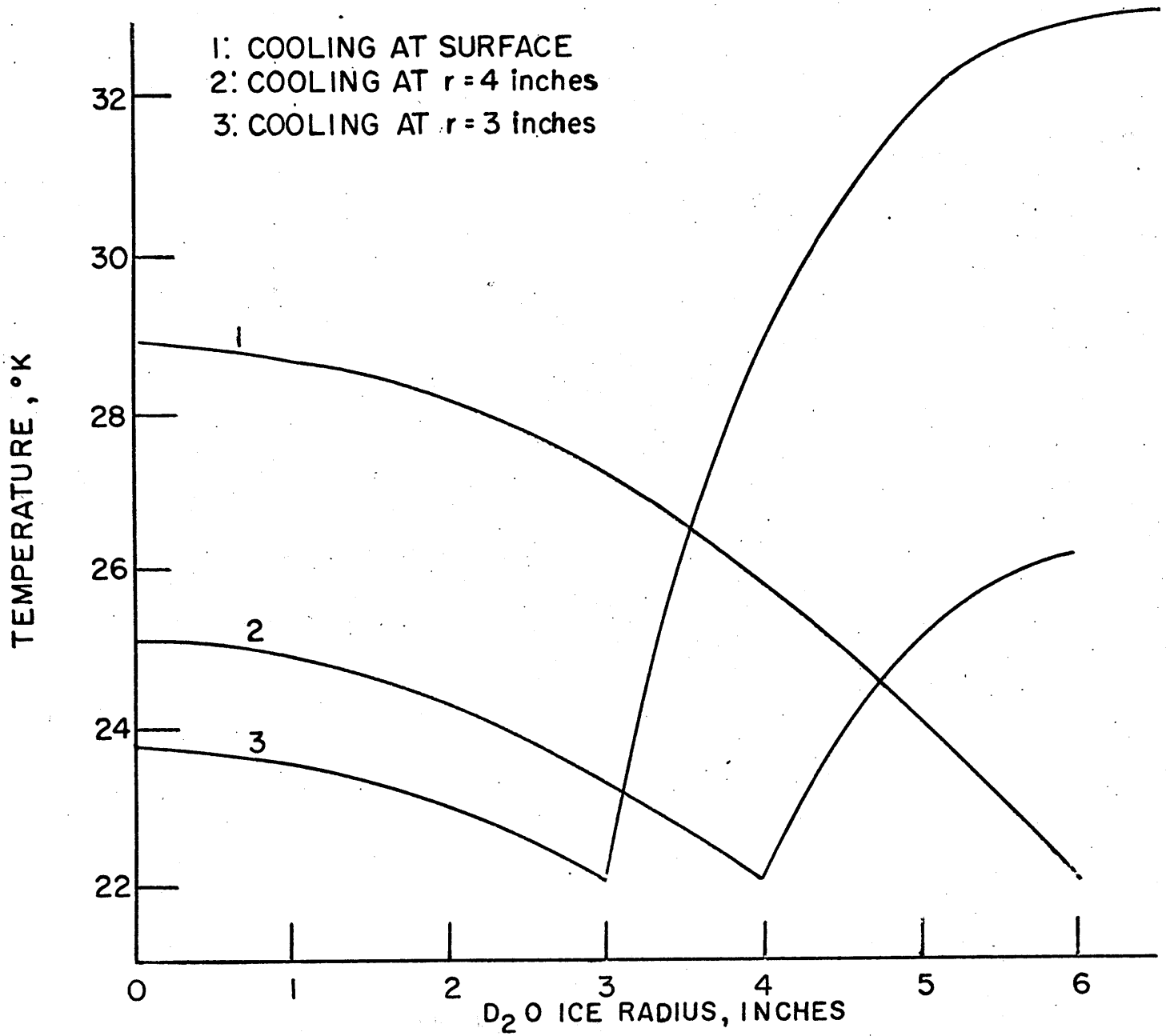

FIG. 5.7 TEMPERATURE DISTRIBUTION IN D_2O ICE

with cold helium gas as the coolant.

As shown in figures 5.1 to 5.4, the helium gas is fed to the cold moderator through a one inch tube 130 inches long. At the cold moderator it enters a header which separates the flow into four $\frac{1}{4}$ inch coils, each approximately 60 inches long. After passing through the cooling coils, the helium is collected in a plenum and returned to the transfer lines through another one inch tube 130 inches long.

The detailed calculations of the pressure drop are given in Appendix E and summarized in Table 5.2.

Table 5.2

Helium Pressure Drop

	ΔP, Psi
Supply Line	0.0146
Return Line	0.0146
Coils and Headers	0.3785

As shown by equation 5.2, the ice temperature is reduced as the surface area of the coils increases; thus, dictating a large number of small diameter tubes. However, since the driving pressure head of the helium refrigerator is limited to about 3-5 psi., it is necessary to minimize the pressure drop acrossed the cooling coils, or to use larger diameter tubes. The final design of the cooling coils has been a balance between the required heat transfer and the available pressure drop.

Chapter 6

Cryostat Testing

6.1.Out of Pile Testing

The cold neutron cryostat was constructed at the M. I. T. Nuclear Reactor Machine Shop. Throughout the construction all welded joints were leak checked with a helium leak detector. All welds indicating leaks were rewelded except for a small leak located in the header section of the cooling coils. This leak was discovered after the sphere had been assembled and repairing it would have required complete reconstruction of the sphere. However, with a low temperature epoxy it was possible to reduce the leak to 10^{-9} cubic centimeters per second of helium at standard temperature and pressure. This was felt to be acceptable since the leak was from the header into the sphere and not into the vacuum space. Because of the small size of the leak it is unlikely that D_2O will leak into the header.

When construction of the aluminum section had been completed, a test was conducted to determine the manner in which the moderator (water) would freeze. The sphere was filled approximately 85% full of distilled water and cooled by passing liquid nitrogen through the coils. Four thermocouples were located in the sphere, as shown in figure 6.1. The bottom of the sphere was insulated with a rubber insulating material.

The water temperature as a function of time is shown in

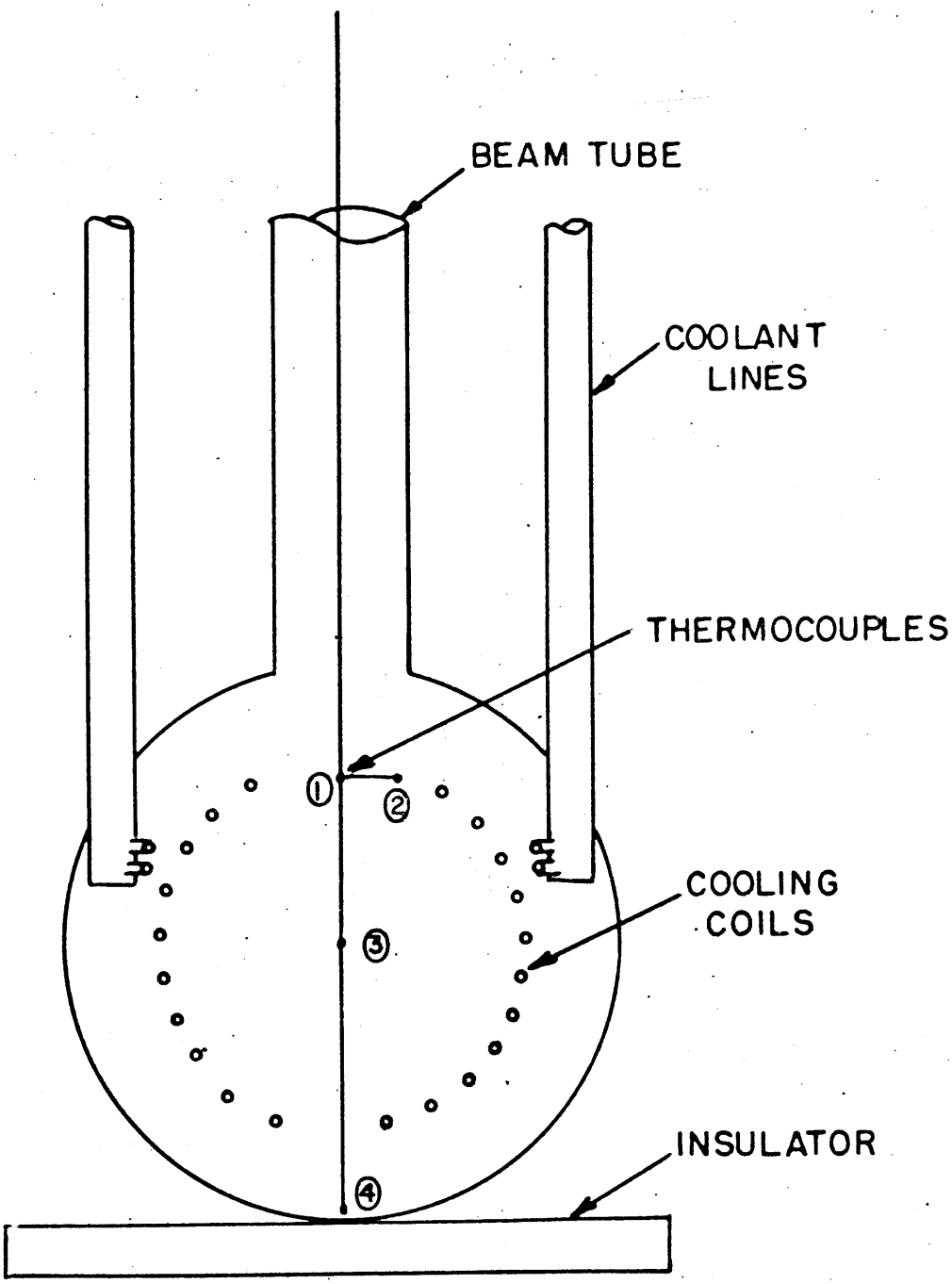

FIG. 6.1 FREEZING TEST

figure 6.2. For the first 35 minutes of cooling the colder and more dense water is on the bottom of the sphere. During the next 10 minutes there is a reversal of the temperature distribution due to the density inversion of water at 4° C. After 100 minutes of cooling the temperature distribution comes into equilibrium at the freezing point. The first point to freeze is the side, near the cooling coils. This is followed by the bottom, then the center, and finally the top. Such a freezing pattern is ideal because it allows the ice to expand upward without damaging the sphere.

This sequence of freezing was verified by visual observation through the 3 inch beam port. Ice first formed around the cooling coils and grew to form a layer around the surface of the sphere. It then grew from the sides and bottom towards the center and top. It is believed that the top was the last to freeze because of heat conduction down the beam tube.

The cryostat was next assembled outside the reactor building for preliminary testing. In the original design a large bellows was located in the 3 inch beam tube to compensate for thermal contraction of the helium lines during cool down; however, no bellows were located in the helium lines themselves. With such an arrangement any differential contraction of the helium lines due to a temperature difference between them results in a sideward deflection of the sphere. Since there is only about $\frac{3}{4}$ inch between the sphere and vacuum jacket it is necessary to limit the amount of deflection to prevent thermal short with the vacuum jacket and to prevent

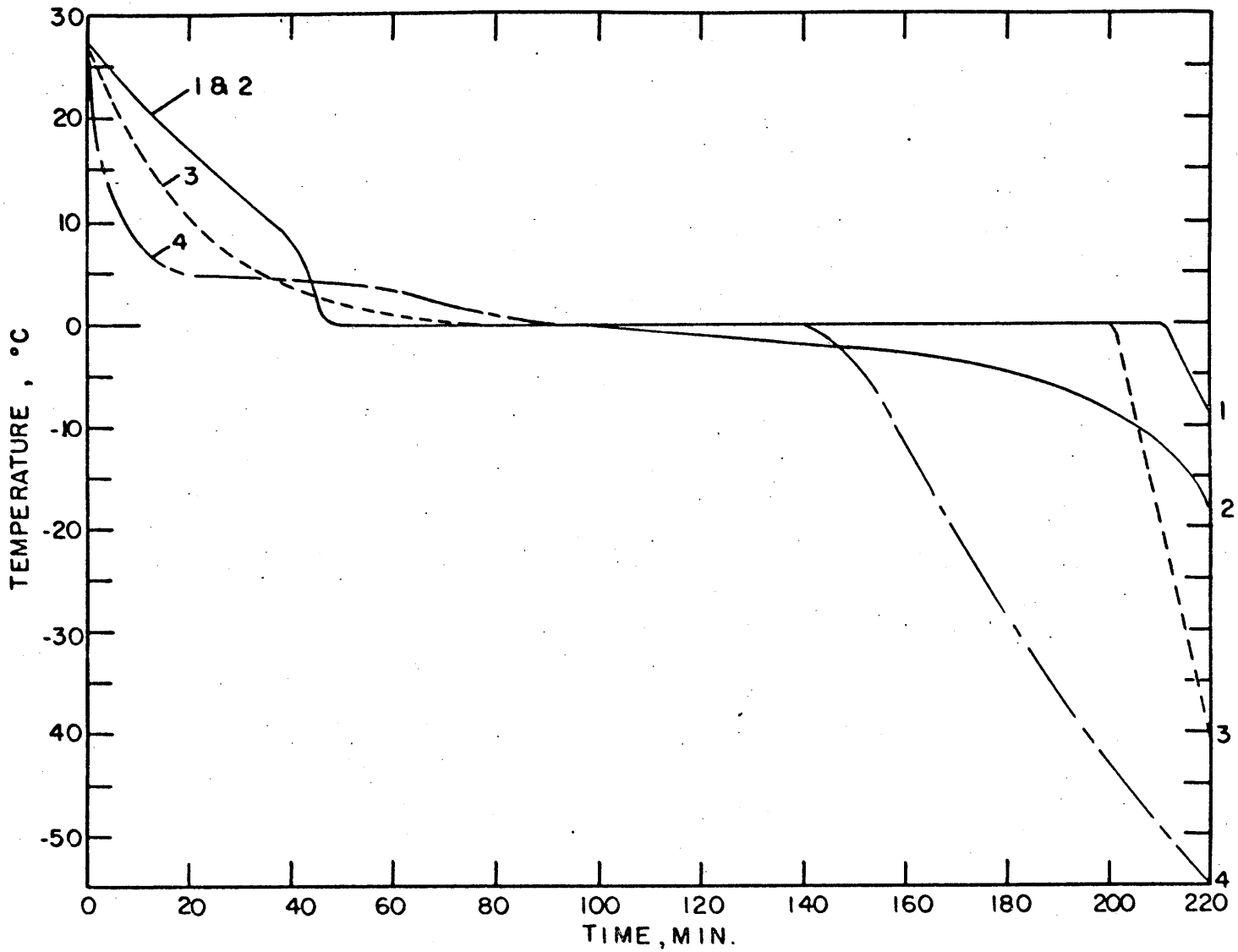

FIG.6.2 WATER TEMPERATURE

excess stresses in the helium lines. With this in mind tests were run to correlate helium line temperature difference with sphere deflection. The results are shown in figure 6.3. As can be seen in the figure, to maintain the deflection less than $\frac{3}{4}$ inch, it is necessary to maintain the temperature difference between the helium inlet and outlet less than 160°C. Because of this restriction in the operation of the cryostat and the possibility of damaging the facility, the bellows in the 3 inch port was replaced by two bellows, one in each of the helium lines. With this arrangement the moderator sphere is supported by the beam tube, and each helium line can contract and expand independent of the other.

As shown in figure 5.1, the lower aluminum section of the cryostat is connected to the upper stainless steel section by flanges. One of the major problems encountered in the out of pile testing was that of achieving helium leak proof connections. The flanges were designed for metal O-ring seals; however, these proved to be unsatisfactory for preventing helium leaks. The problem was temporarily solved by replacing the O-rings with 60 mil diameter indium solder. This solder made the system leak tight at room temperature.

At this point the vacuum jacket was put in place and the cryostat evacuated to approximately 20 microns pressure with a mechanical vacuum pump. Again the sphere was filled approximately 85% full of distilled water and cooled with liquid nitrogen; however, when the coolant lines reached a temperature of about -50°C the vacuum was lost, indicating a leak. Cooling was continued, but after about 30 minutes, temperature readings

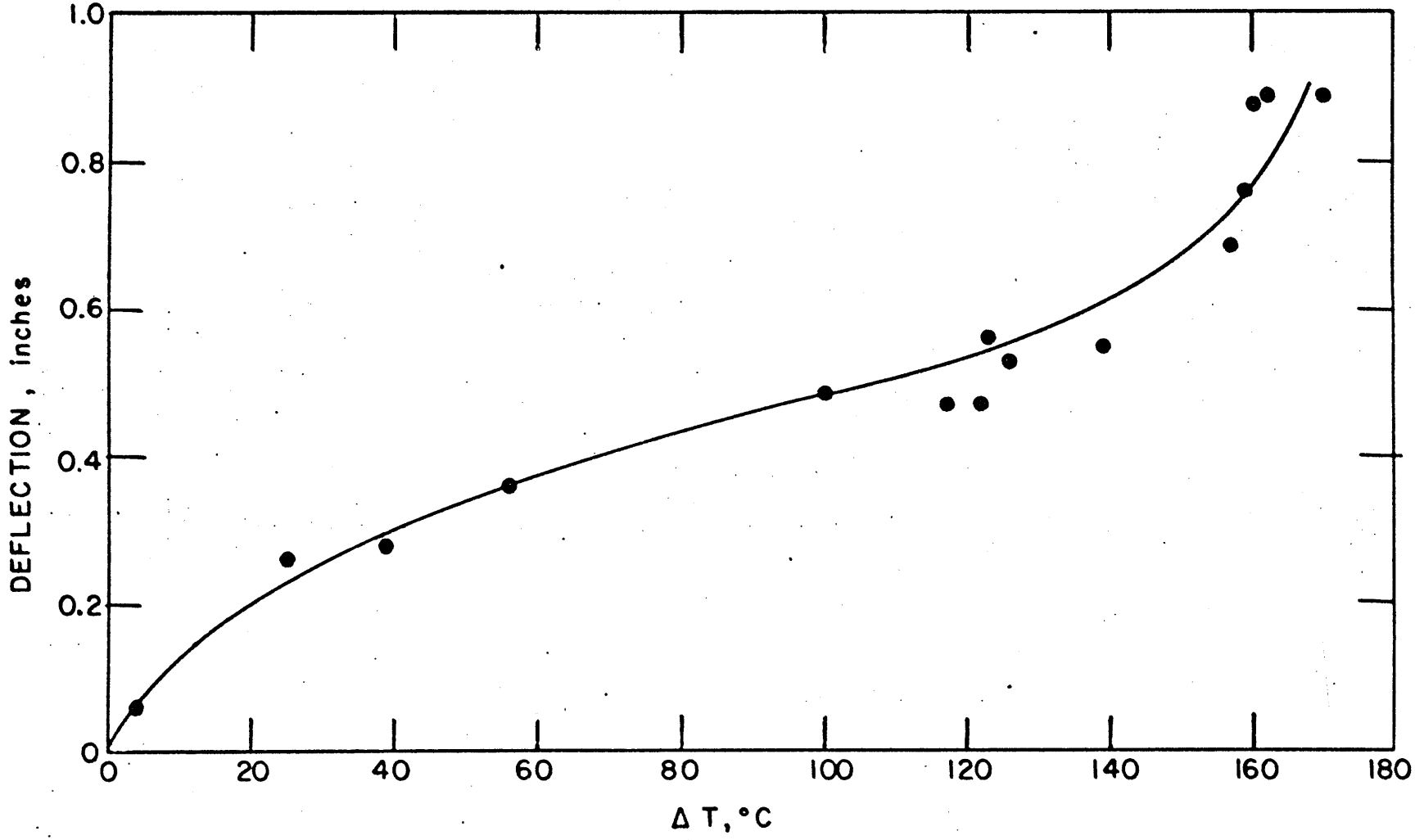

FIG. 6.3 SPHERE DEFLECTION

plus visual observation indicated that the top of the water was freezing, and the liquid nitrogen flow was stopped. Once the coolant lines warmed up, the vacuum was regained. It should be noted that approximately 3 hours after shut down all the water in the sphere was frozen.

After removing the vacuum jacket a vacuum was drawn on the coolant lines. By cooling the flanges down with liquid nitrogen it was determined that this is where the leaks occurred on cooling.

Having determined the location of the cold leaks, the cryostat was reasembled inside the reactor building. Again stainless steel O-rings and indium solder proved to be useless for maintaining helium tight flanges when cooled down with liquid nitrogen.

The indium solder was then replaced by gaskets cut from 10 mil thick indium foil. After four cycles of cool down the flanges were found to be helium leak tight even when cooled to liquid nitrogen temperature.

It should be noted that the flange on the beam tube contains a stainless steel O-ring coated with silver. This flange was also cooled down four times and found to be helium leak tight at liquid nitrogen temperature.

Again the vacuum jacket was put into place and the cryostat evacuated to about 20 microns pressure with a mechanical vacuum pump. With the sphere empty the cryostat was cooled down with liquid nitrogen. During cool down the pressure fell to about 15 microns indicating there were no cold leaks.

Distilled water was then placed into the sphere and cooled with liquid nitrogen. The water temperature as a function of time is shown in figure 6.4 It can be seen that the temperature distribution follows a similar pattern as that shown in figure 6.2 except for the sudden drop in the top temperature after 36 minutes of cooling. Visual observation through the beam tube indicated that there still was water at the top. In this test the thermocouples were approximately one inch off the centerline of the sphere; thus, the top thermocouple was probably reading a temperature similar to thermocouple 2, figure 6.1. As can be seen in figure 6.3 this thermocouple indicated freezing long before the top center freezes; however, in this test the liquid nitrogen flow was stopped to prevent freezing from the top down and possible damage to the sphere.

The above tests gave no definite conclusions as to the manner in which the water will freeze; however, in the thermal column it might be expected that the freezing pattern will be quite different from the above results because of the induced heating due to gamma and neutron irradiation. If it should tend to freeze on the top first, cooling can be stopped and the ice allowed to melt. The water may then be withdrawn from the sphere. It can then be put back into the sphere in small quantities and the ice formed in layers.

6.2. In Pile Testing

Before the cryostat could be inserted into the thermal

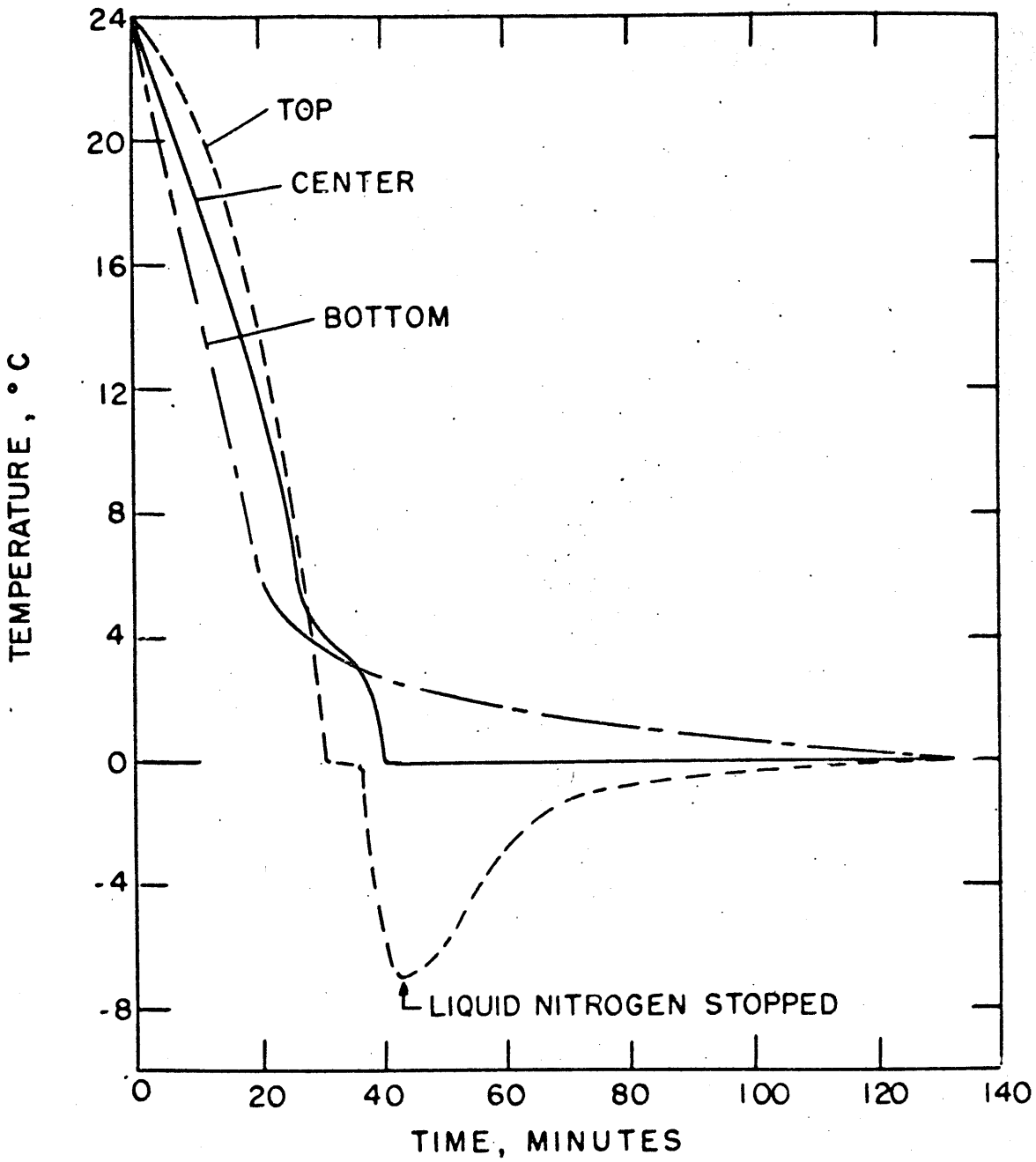

FIG. 6.4 WATER TEMPERATURE

column it was necessary to remove some of the graphite. This was done by sawing a 14 inch diameter vertical hole in the thermal column, as shown in figure 5.1. The thermal column is made up of horizontal layers of graphite stringers approximately 4 inches thick. The hole was cut by sawing through one layer at a time and removing the cut stringers after each layer was cut. To prevent the saw from plugging up with sawdust it was necessary to drill a one inch diameter vertical hole in the saw cut. This gave space for the sawdust to go and prevented plugging of the saw teeth. During the operation, the maximum radiation level over the hole was about 75 mr/hr. The graphite stringers varied from about 100 to 400 mr/hr on contact.

After the out of pile testing had shown that the cryostat was helium leak tight, it was inserted into the thermal column. Because of the close fit between the shield plug and the hole in the concrete shielding some difficulty was encountered in installing the cryostat; however, after grinding off the high spots on the shield plug it was possible to get the cryostat into place.

During the installation the hemispherical end of the vacuum jacket was dented near the point where it is welded to the cylindrical part. Because of this a vacuum was drawn on the cryostat immediately after installation to determine whether or not a leak had developed. After approximately one hour the pressure was 30 microns and falling; therefore, it was felt that no leaks had developed and the reactor was brought up to power. After about one and a half hours the cryostat, without D_2O, had heated up to approximately 155°F and due to

outgasing the pressure had risen to about 60 microns. Once the surfaces in the vacuum region completed outgasing the pressure dropped to about 20 microns and was maintained at that level for nine days. At this point it was felt that the vacuum jacket was tight and the vacuum space was back filled with helium gas.

During the first three weeks after installation, the temperatures in the cryostat were monitored frequently. The average recorded temperatures, with no D_2O in the sphere, are given in Table 6.1.

Table 6.1

Empty Cryostat Temperatures, °F

	20 Micron Vacuum	Helium in Vacuum Space
Sphere Top	176 ± 1	151 ± 1
Sphere Center	176 ± 1	152 ± 2
Sphere Bottom	175 ± 1	151 ± 1
Helium Inlet	160 ± 1	136 ± 3
Helium Outlet	162 ± 1	130 ± 1
Beam Tube	163 ± 1	133 ± 1

By using this information, the inner aluminum heating rate is estimated to be approximately 6.3×10^{-3} watt/cm^3. The calculated value (Appendix D) is 10.9×10^{-3} watts/cm^3. This indicates that the calculated heat loads due to gamma and neutron irradiation may be conservative by a factor of about 1.7

With D_2O in the sphere, helium in the vacuum space, and no coolant flowing through the cooling coils, the surface temperature of the D_2O is estimated to be about 188°F. This is based on the calculated heating rate of about 60 watts in the D_2O. Assuming only conduction in the D_2O, a conservative estimate of its centerline temperature is about 230°F; therefore, the D_2O will boil if no cooling is supplied. Should the calculated heating rate be conservative by a factor of 1.7, the surface temperature and centerline temperature will be about 173°F and 199°F respectively.

Because of the possibility of boiling the D_2O, special precautions have been taken to assure safe operation of the cryostat. A $\frac{1}{8}$ inch diameter aluminum tube has been placed into the beam tube. The tube extends from the gas seal to the bottom of the sphere (figure 5.1). The tube will be used for putting the D_2O into the sphere and will permit quick withdrawal of the D_2O in the case of an emergency. The center thermocouple in the sphere has been connected to a temperature recorder in the control room and to the reactor alarm system. The alarm has been set at 180°F. A safety release valve has also been installed in the gas seal. This has been set to release at an overpressure of about 10 Psi, which is the vapor pressure of a D_2O at a temperature of about 193°F.

To prevent excess evaporation and possible boiling of the D_2O, CO_2 is circulated through the cooling coils. The CO_2 is supplied from a bottle of liquid CO_2 and discharged to the reactor ventillation system.

Because of the possibility of boiling, and to prevent excess build up of tritium in the D_2O, it is planned to remove the D_2O from the cryostat when it is not being used for a neutron source.

6.3. Flux Measurements

As part of the in pile testing of the cryostat, neutron energy distribution measurements in the sphere were made by using the time of flight method. The layout of the equipment used for the measurements is shown in figure 6.5. The chopper is located in the vertical beam at the top of the thermal column. The flight path from the chopper to the BF_3 detector is an aluminum tube filled with helium. The length of the flight path is 94 inches. The pulses from the BF_3 detector are fed to a 256 channel analyser. A detailed description of the time of flight equipment used for these measurements is given in references 24 and 32.

For these measurements the chopper speed was 600 RPM and the channel width 16 microseconds. By varying the chopper speed, it was found that the measurements were independent of chopper speed for speeds greater than about 600 RPM. It was also found that the channel number of the peak varied inversely with the channel width, as is expected.

Shown in figure 6.6 is the neutron spectrum in the warm graphite of the thermal column. This spectrum was measured with the sphere empty. The vertical error flags represent the

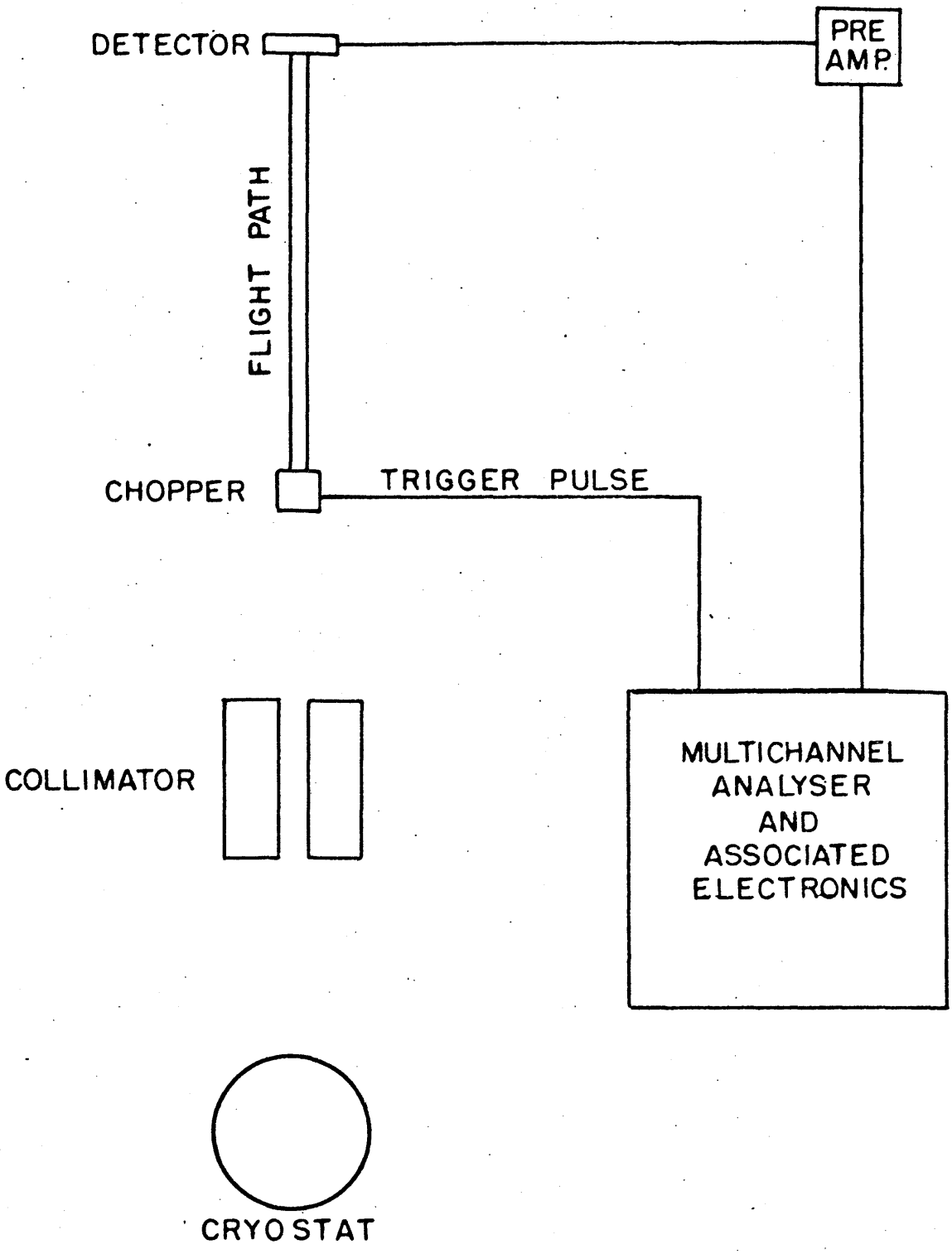

FIG. 6.5 SPECTRUM MEASURING EQUIPMENT

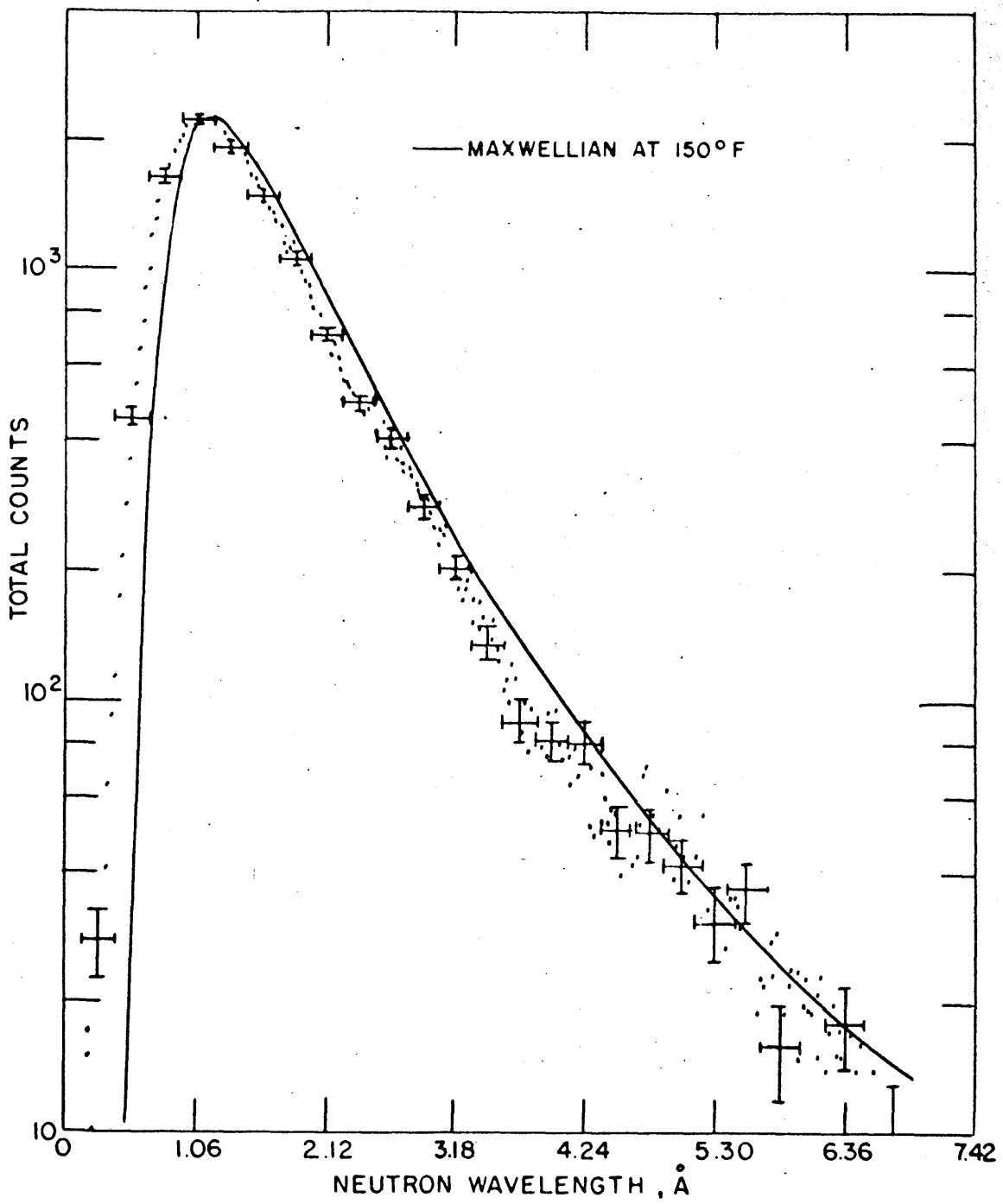

FIG. 6.6 NEUTRON SPECTRUM IN GRAPHITE THERMAL COLUMN

error due to counting statistics. The horizontal error flags represent the resolution of the detection system. This error is due to the uncertainty in flight path length, the finite opening time of the chopper, and the finite width of the channels in the multichannel analyser. Also shown is the maxwellian distribution at the measured temperature of the sphere, 150°F.

Shown in figure 6.7 is the neutron spectrum with warm (95°F) D_2O in the sphere. For this measurement a one inch diameter re-entrant port penetrated the D_2O to a depth of four inches from the surface, or two inches from the center. The spectrum has been normalized to the same counting time and reactor power as that used for the graphite spectrum. The error flags represent the same quantities as in the graphite spectrum. Also shown is the maxwellian at the measured temperature of the D_2O, 95°F.

The measured neutron distribution follows the maxwellian distribution quite closely. The shift toward shorter wavelengths (higher energies) is almost within the uncertainties of the measurement; however, the shift is in the direction expected from the effect of the 1/v dependent neutron absorption in the aluminum and moderator.

Two cold spectra were measured using D_2O ice, one at 3°C and one at -40°C. The measurements were limited to these temperatures because of a vacuum leak which developed during the cool down of the cryostat. For both measurements a one inch diameter re-entrant port penetrated the sphere to a depth

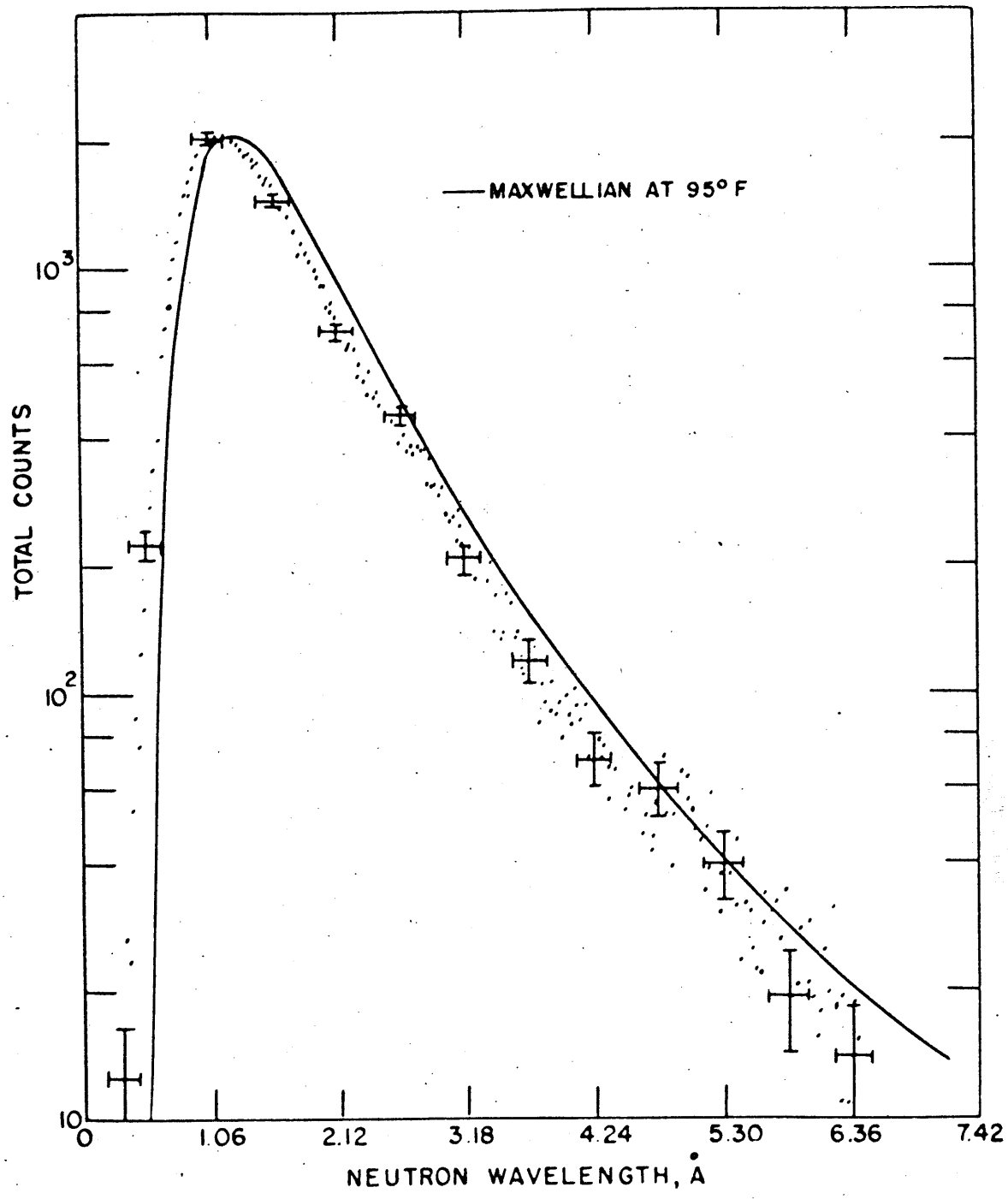

FIG. 6.7 NEUTRON SPECTRUM IN WARM D_2O

of 4 inches from the surface.

The spectrum at 3°C is shown in figure 6.8, and the spectrum at -40°C in figure 6.9. Shown with the experimental data are the maxwellian distributions at the corresponding temperatures. Again the measured neutron distributions are shifted toward shorted wavelengths because of the 1/v dependent neutron absorption of the aluminum and moderator.

For comparison, the measured spectra are all shown in figure 6.10. In this figure, the "best fit" curves to the data are shown. The warm D_2O and graphite data are the same within the uncertainty of the measurements. There appears to be an increase in long wavelength neutrons for D_2O ice at 3°C; however, since the uncertainty of the data falls within the uncertainty of the graphite data the observed increase may not be a real effect. The uncertainty of the data for D_2O ice at -40°C falls outside of the uncertainty of the graphite data; therefore, the observed increase in long wavelength neutrons is expected to be a real effect.

The measured gain for 3.18 Å neutrons is about 1.5, and for 5.30 Å neutrons about 1.8. This pattern of increasing gain with increasing wavelength is expected from the results of section 7.2. It should be noted that the spectra in the this chapter are neutron density spectra as compared with neutron flux spectra shown in section 7.2. This is due to the fact that the neutron absorption in the detector is 1/v dependent.

The measured neutron spectra shown in this section have been normalized to the same counting time, 230 minutes, and the

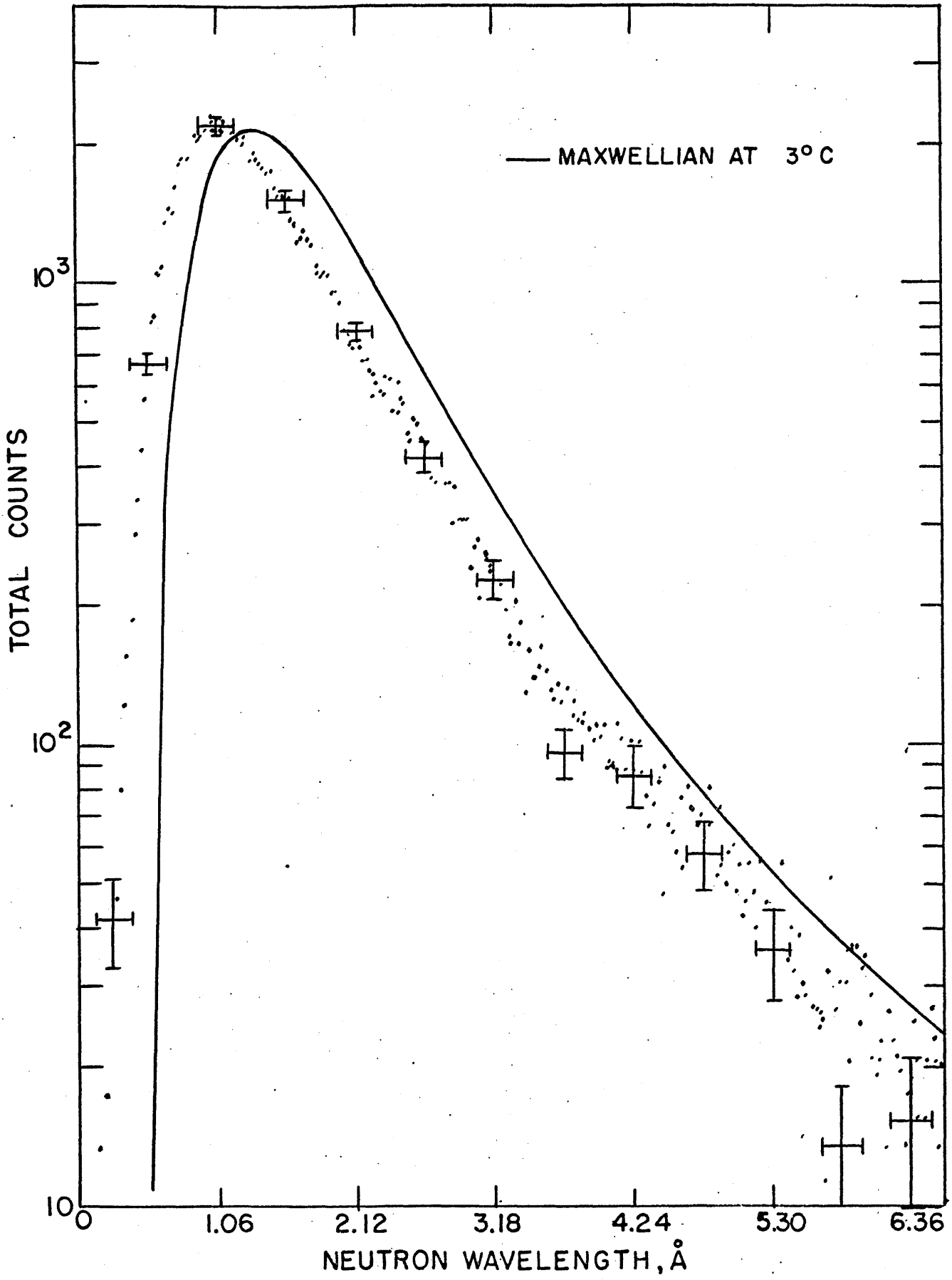

FIG. 6.8 NEUTRON SPECTRUM IN D_2O ICE AT 3°C

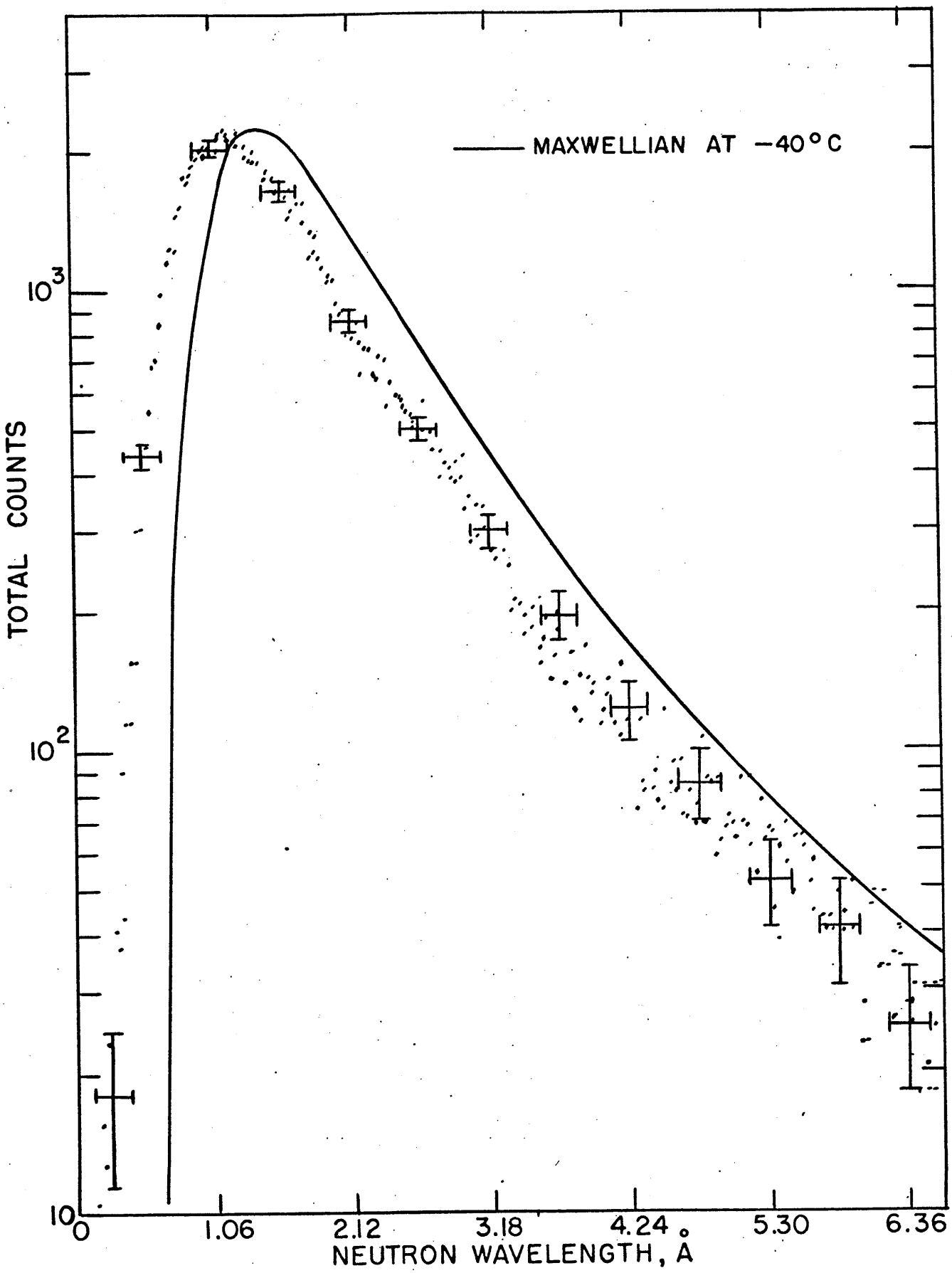

FIG. 6.9 NEUTRON SPECTRUM IN D_2O ICE AT −40°C

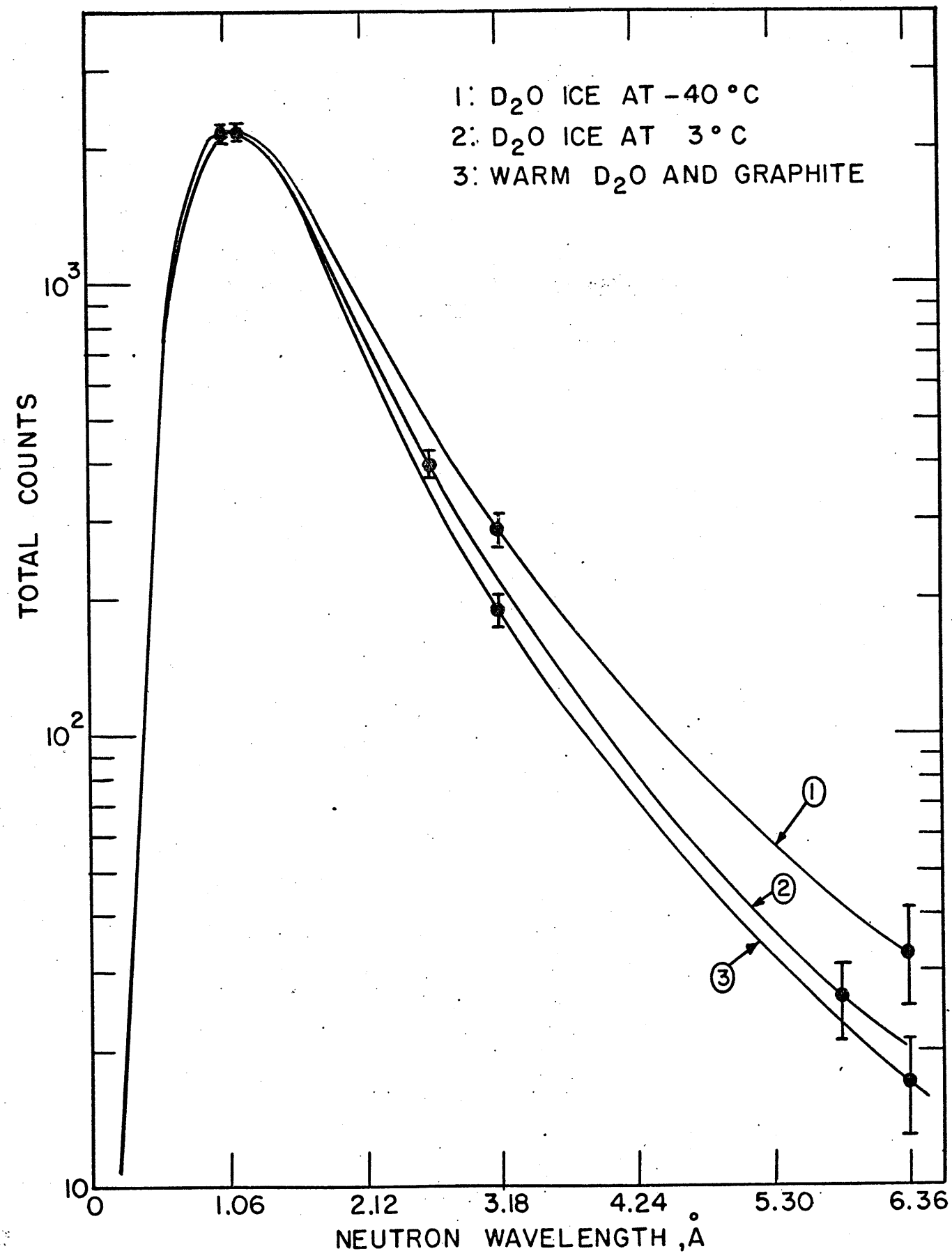

FIG. 6.10 MEASURED NEUTRON SPECTRA

same reactor power, 4.88 Mw. No corrections have been applied to the data.

The detector efficiency is about 5% for 1 Å neutrons and varies as 1/v. By using this, the intensity of 1 Å neutrons at the detector is estimated to be approximately $8X10^3$ n/cm^2. sec.

A comparison between measured spectra and calculated spectra is given in section 7.3.

Chapter 7

Flux Calculations in Cold Moderator

7.1 Method of Calculation

Calculations of the neutron flux have been carried out as a part of this design in an attempt to predict the effectiveness of the cold moderator. To date very little theoretical work has been published on the subject of cold neutrons; consequently, no rigorous theory exists for determining the effectiveness of a cold moderator in slowing down neutrons to subthermal energies (19).

In this work it has been assumed that the problem can be treated the same as the thermalization of neutrons in a warm moderator, and the calculations have been carried out using the computer program Thermos (15) with the Brown-St. John scattering Kernel. Thermos solves the integral transport equation with isotropic scattering. The Brown-St. John scattering Kernel takes into account chemical binding effects by assigning to the scattering nucleus an effective mass which is larger than the mass of the nucleus itself.

The model used for the calculations is shown in figure 7.1. Regions 1 and 3 are cold moderator. Region 2 represents the cooling coils and is taken as a homogeneous mixture of aluminum, helium; and cold moderator. Region 4 is graphite at the temperature of the thermal column and contains a slowing down source near its outer edge. This region is not meant to

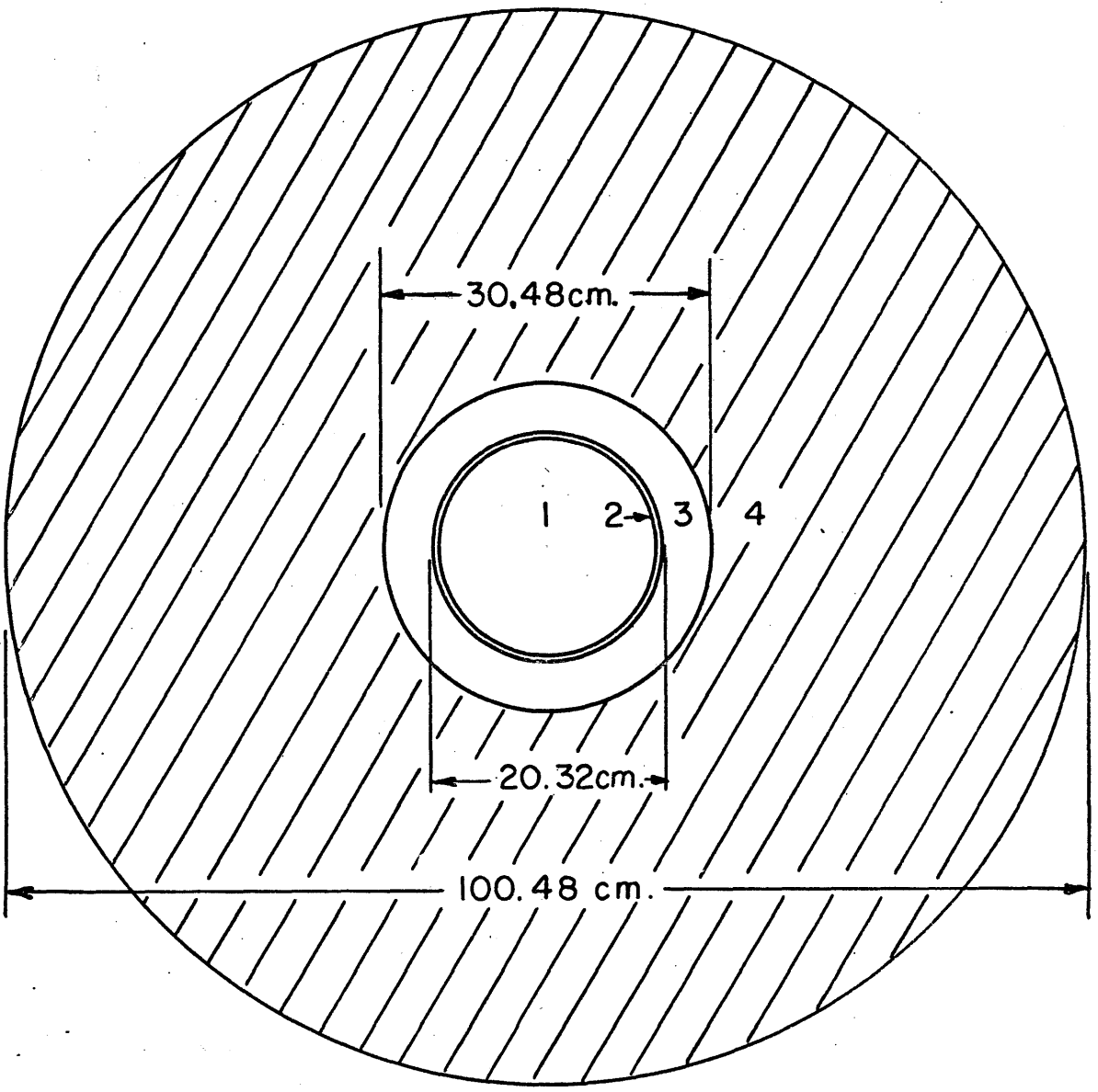

FIG. 7.1. MODEL OF COLD MODERATOR

represent the thermal column, but has been chosen so as to give a thermal neutron spectrum at the edge of the cold moderator which is nearly a maxwellian at the temperature of the thermal column.

Thermos has been written for an infinite cylinder, which one would expect to over predict the magnitude of the fluxes in a sphere of the same radius. A conservative correction has been made by reducing the radius of the infinite cylinder so that its buckling, neglecting extrapolation length, is the same as that for a sphere,

$$Rc = \frac{2.405}{\pi} Rs \qquad (7.1)$$

where Rc = effective radius of infinite cylinder

Rs = radius of sphere.

The energy range has been taken as zero to 0.3019 ev which corresponds to velocities of zero and 7600 m/sec respectively. Between zero and 2400 m/sec 30 velocity groups have been used with spacings of 80 m/sec. Between 2400 m/sec and 7600 m/sec 20 velocity groups have been used with spacings of 260 m/sec.

The low temperature cross sections for H_2O and D_2O have been taken from references 21 and 22. The cross sections for the remaining isotopes have been taken from reference 23.

7.2 Results

For a comparative basis the neutron spectrum in a solid graphite cylinder has been calculated. The spectrum at the

center of the cylinder is shown in figure 7.2. Also shown is the maxwellian distribution at the temperature of the thermal column, 343°K. The excellent agreement between the curves indicates that the neutrons are well thermalized in the graphite.

Shown in figure 7.3 is the gain in cold neutrons as a function of position in the cold moderator. For all cases, the gain is defined as

$$\text{Gain} = \frac{\text{Flux of neutrons with velocities<1000m/sec in cold moderator}}{\text{Flux of neutrons with velocities<1000m/sec in warm moderator}} \qquad (7.2)$$

Curve 1 is the case for solid D_2O ice at 20°K with no correction for buckling. Curve 3 shows the effect of correcting for buckling as given by equation (7.1).

The purest D_2O available at the reactor contains about 0.22 volume per cent H_2O. The effect of adding this amount of H_2O is shown by curve 2

The actual cold moderator contains aluminum cooling coils as shown in figure 7.1. The effect of the cooling coils is shown by curve 4.

For the above cases the effective masses of deuterium and hydrogen in D_2O and H_2O ice have been taken the same as those of the liquids; that is, 3.60 and 1.88 respectively. In the low temperature ice, one would expect the atoms to be more tightly bound than in the liquid and thus have a higher effective mass. The effect of using a larger effective mass

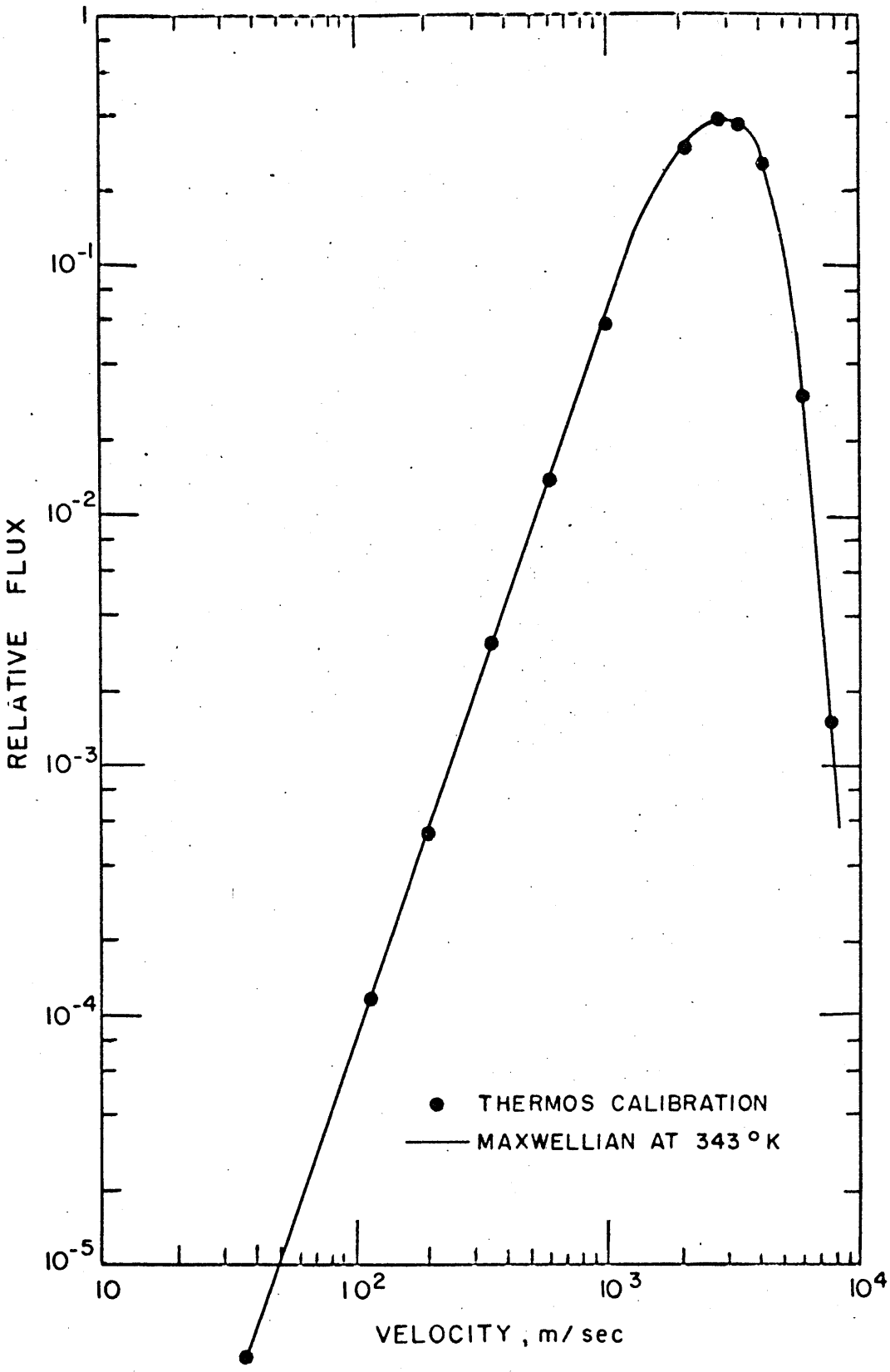

FIG. 7.2 NEUTRON SPECTRUM IN GRAPHITE

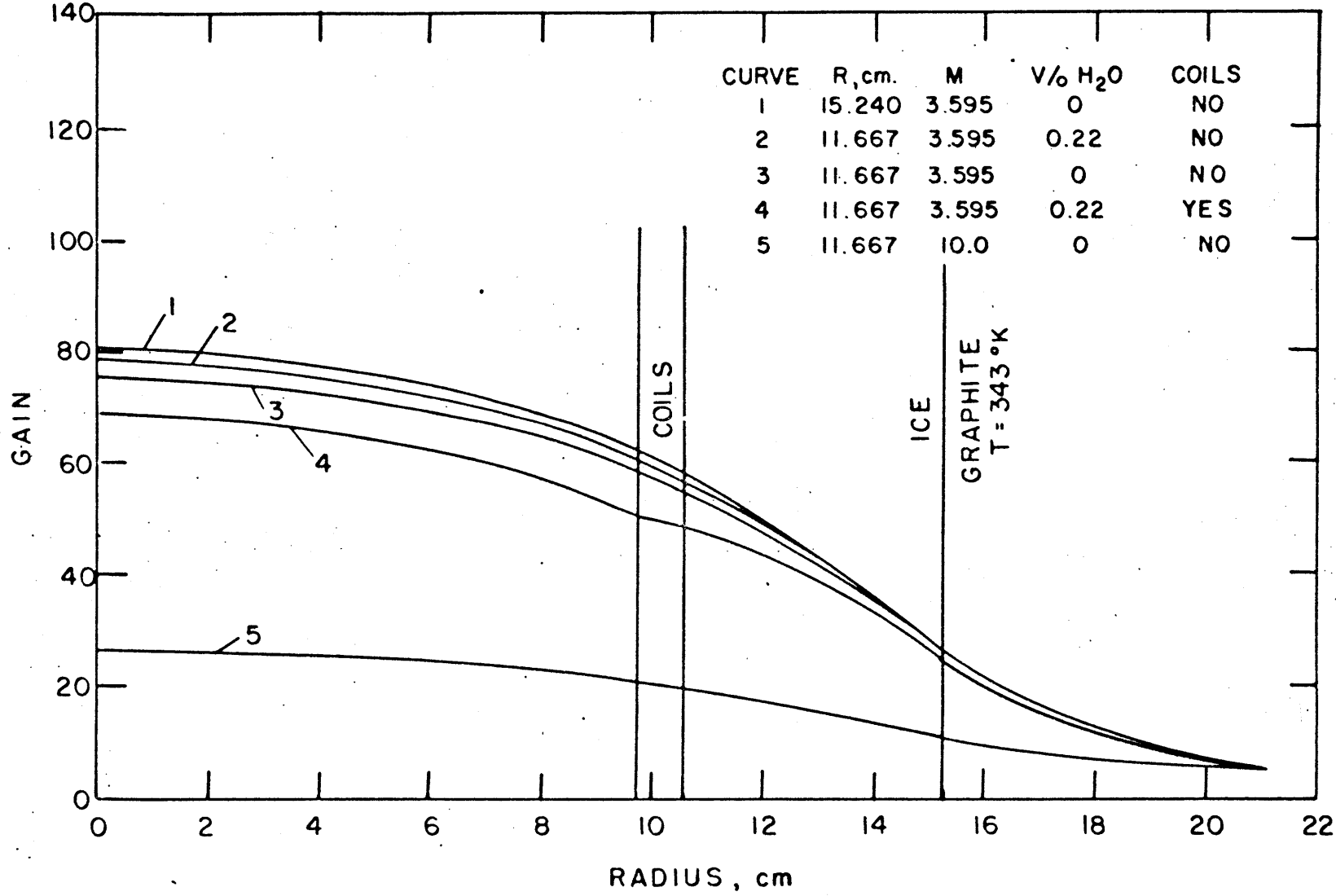

FIG. 7.3. COLD NEUTRON ($\lambda \geq 3.96$ Å) GAIN

is shown by curve 5, where M has been taken as 10 for D_2O ice. Because of the large effect, it was decided to estimate as accurately as possible the effective masses of H_2O and D_2O ice. In the Brown-St. John scattering Kernel the effective mass is defined in terms of the mass of the scattering nucleus (H or D) and the translational and rotational energies of the molecule. Using the method of Brown-St. John (20) and data obtained from reference 25 the effective masses of H_2O and D_2O ice have been estimated to be 2.29 and 4.39 respectively.

The results of using these effective masses is shown by curve 2 of figure 7.4. Shown for comparison is the gain calculated using the effective masses of the liquids. For both cases the volume per cent of H_2O is one per cent. The estimated effective masses give a gain which is about 8% lower than the value obtained using the effective masses of the liquids.

By using two group diffusion theory, Cavanaugh (24) has shown that for a mixture of H_2O-D_2O ice in the form of a cylinder, 5.7 cm in radius, the maximum gain in cold neutrons occurs with about 25 volume per cent H_2O. With this in mind, Thermos has been used to calculate the cold neutron gain in a spherical moderator, 12 inches in diameter, as a function of H_2O concentration. The results are shown in figures 7.5 and 7.6. In all cases the effective masses of D_2O and H_2O ice have been taken the same as those of the liquids.

Figure 7.5 shows the gain as a function of distance in the cold moderator. As is expected, for low H_2O concentrations,

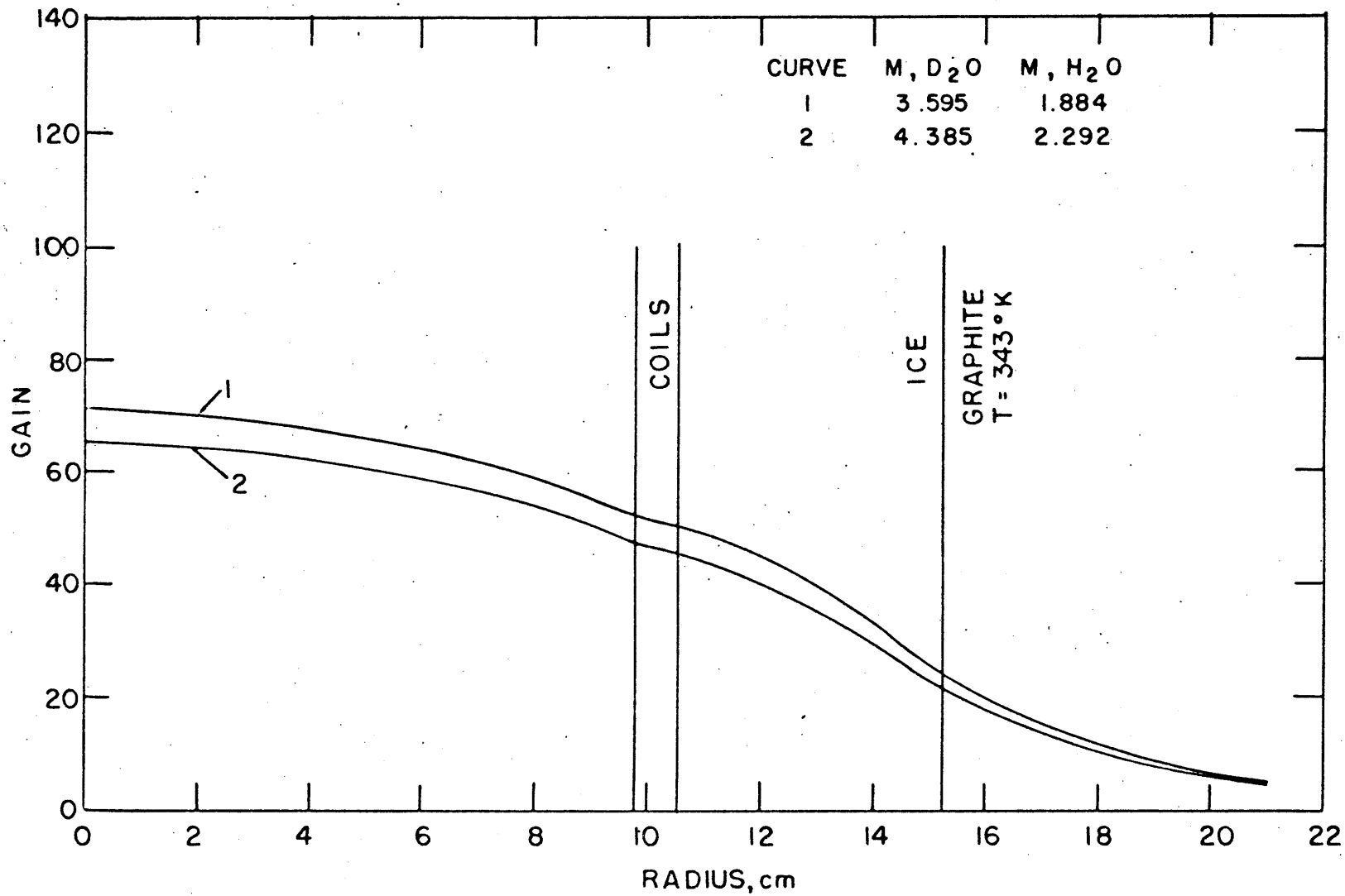

FIG. 7.4. COLD NEUTRON ($\lambda \geq 3.96$ Å) GAIN

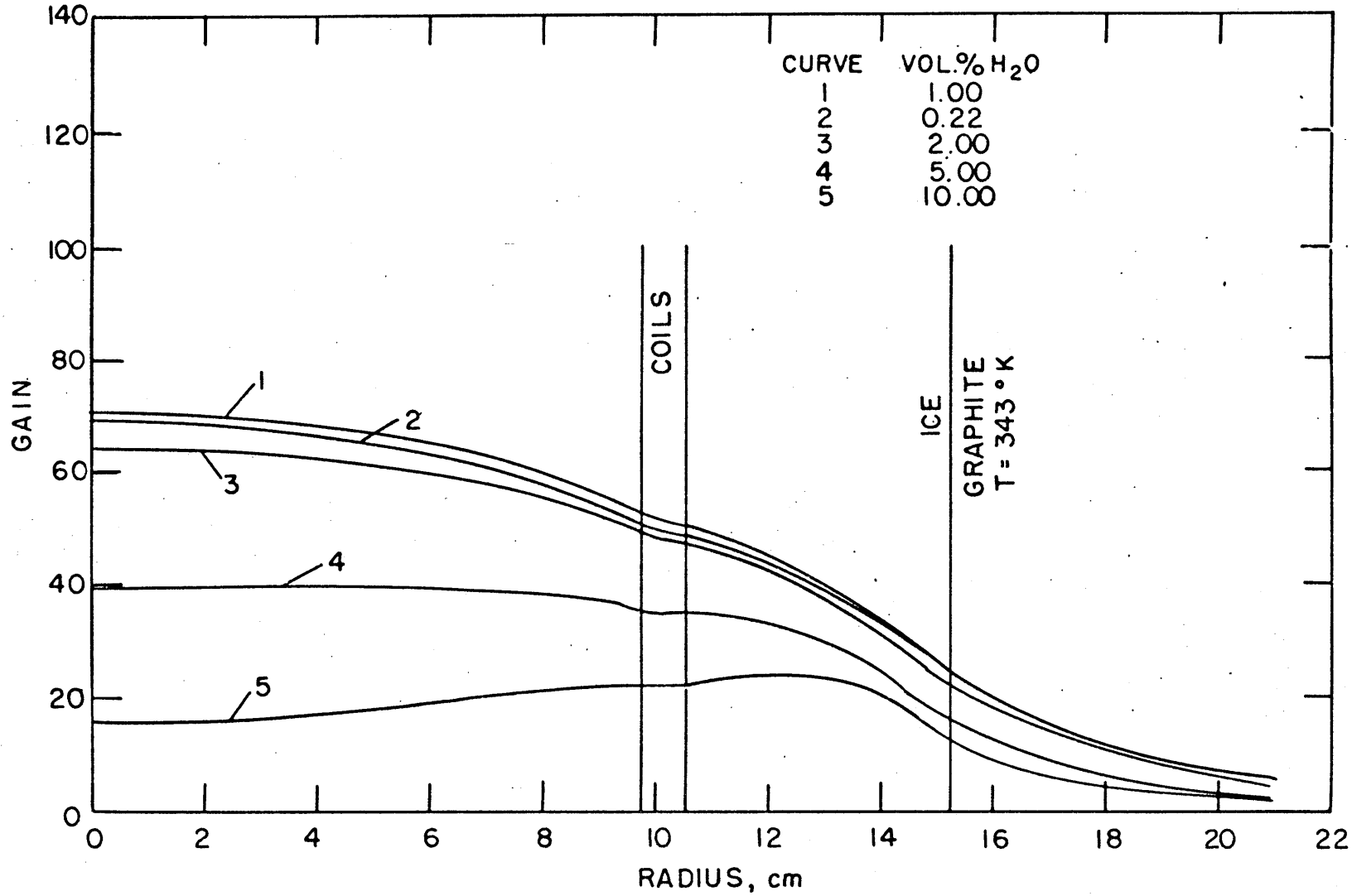

FIG. 7.5. COLD NEUTRON ($\lambda \geq 3.96$ Å) GAIN

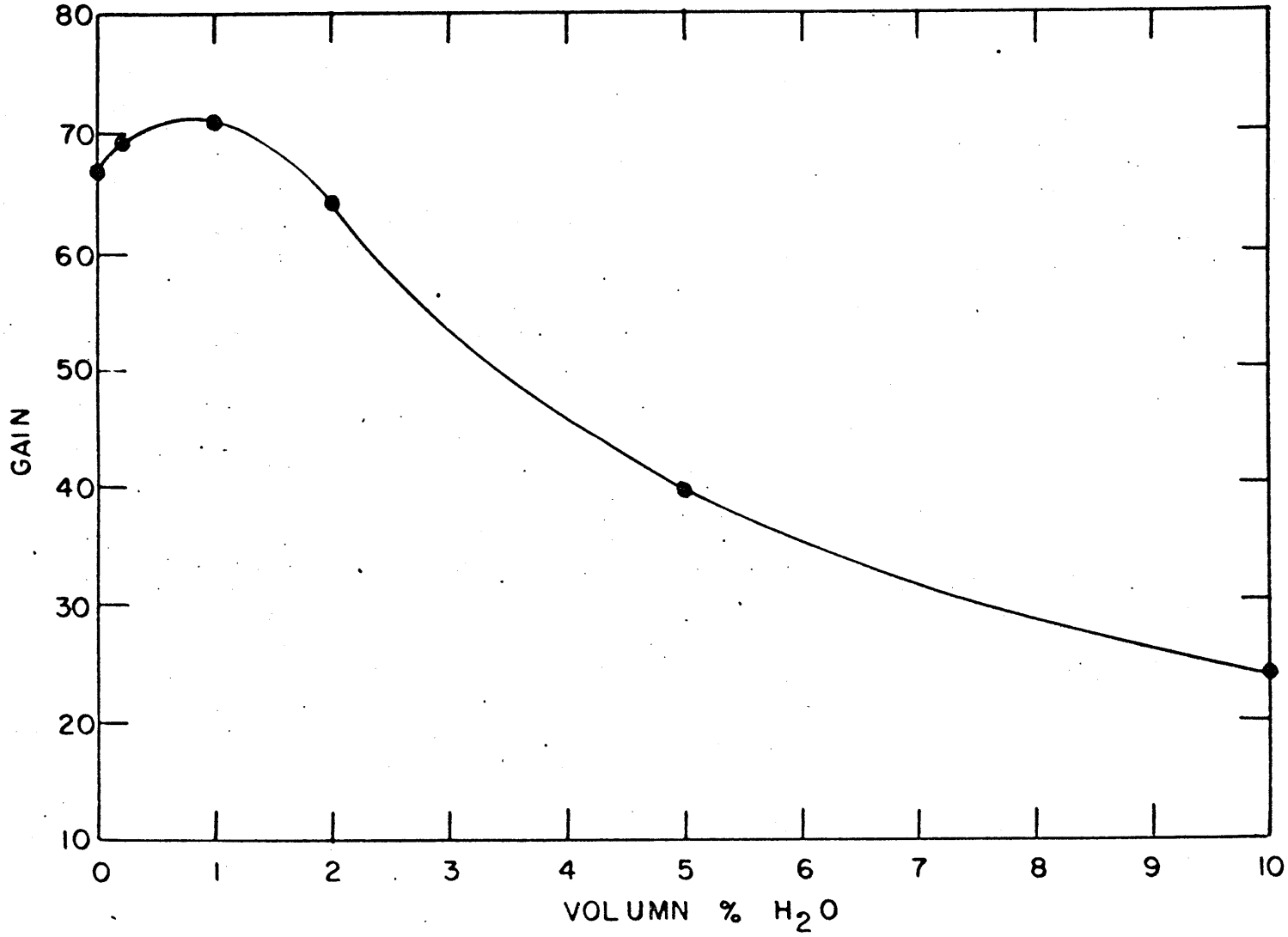

FIG. 7.6. COLD NEUTRON ($\lambda \geq 3.96$Å) GAIN

the gain continuously increases as the depth into the moderator increases; however, for H_2O concentrations above a certain limit the absorption causes the gain to decrease thus giving a peak near the edge of the moderator.

Shown in figure 7.6 is the cold neutron gain as a function of H_2O concentration. For each concentration the maximum gain is shown. As can be seen the maximum gain occurs at an H_2O concentration of one volume per cent. These results, combined with those of Cavanaugh, may indicate that the optimum H_2O concentration is a function of the moderator size.

The results are what one might expect. For low concentrations of H_2O, its high slowing down power is more important than its high absorption and the gain is increased. However, once the concentration exceeds about one volume per cent, the absorption becomes important and the gain decreases.

Shown in figure 7.7 is the neutron spectrum at the center of the cold moderator for the case of one volume per cent H_2O and the cooling coils included. For this spectrum the estimated effective masses have been used. Also shown is the maxwellian distribution at the temperature of the ice, 20°K. As can be seen the cold moderator does not completely shift the spectrum to one that is characteristic of the moderator temperature. The peak of the calculated curve occurs at a velocity of 800 m/sec or a wavelength of 4.95 Å. This corresponds to a temperature of 26°K.

Shown in figure 7.8 is the cold neutron gain as a function of wavelength for the spectrum shown in figure 7.7. It should be noted that the gain for any wavelength longer than about

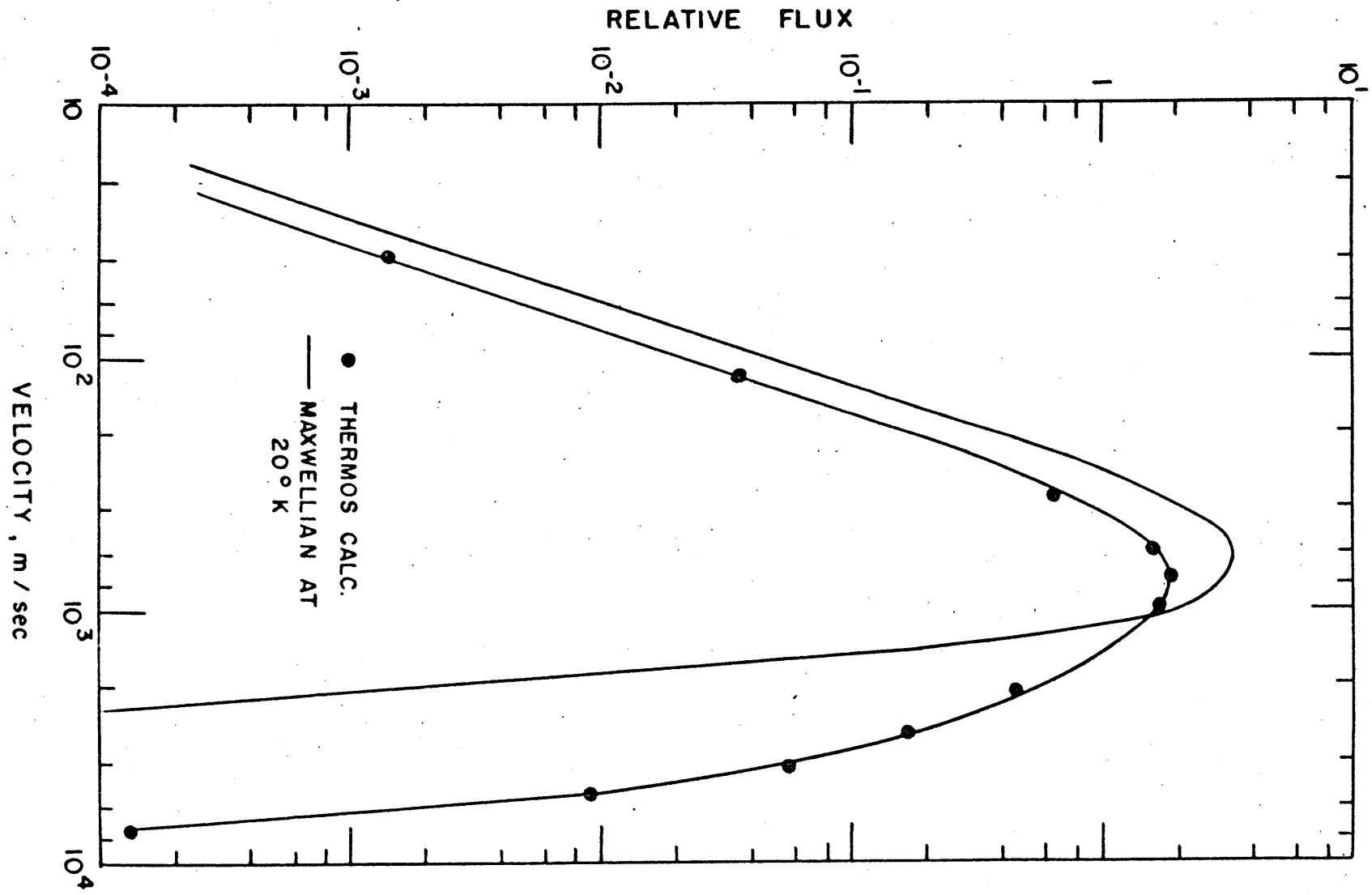

FIG. 7.7. NEUTRON SPECTRUM IN COLD MODERATOR

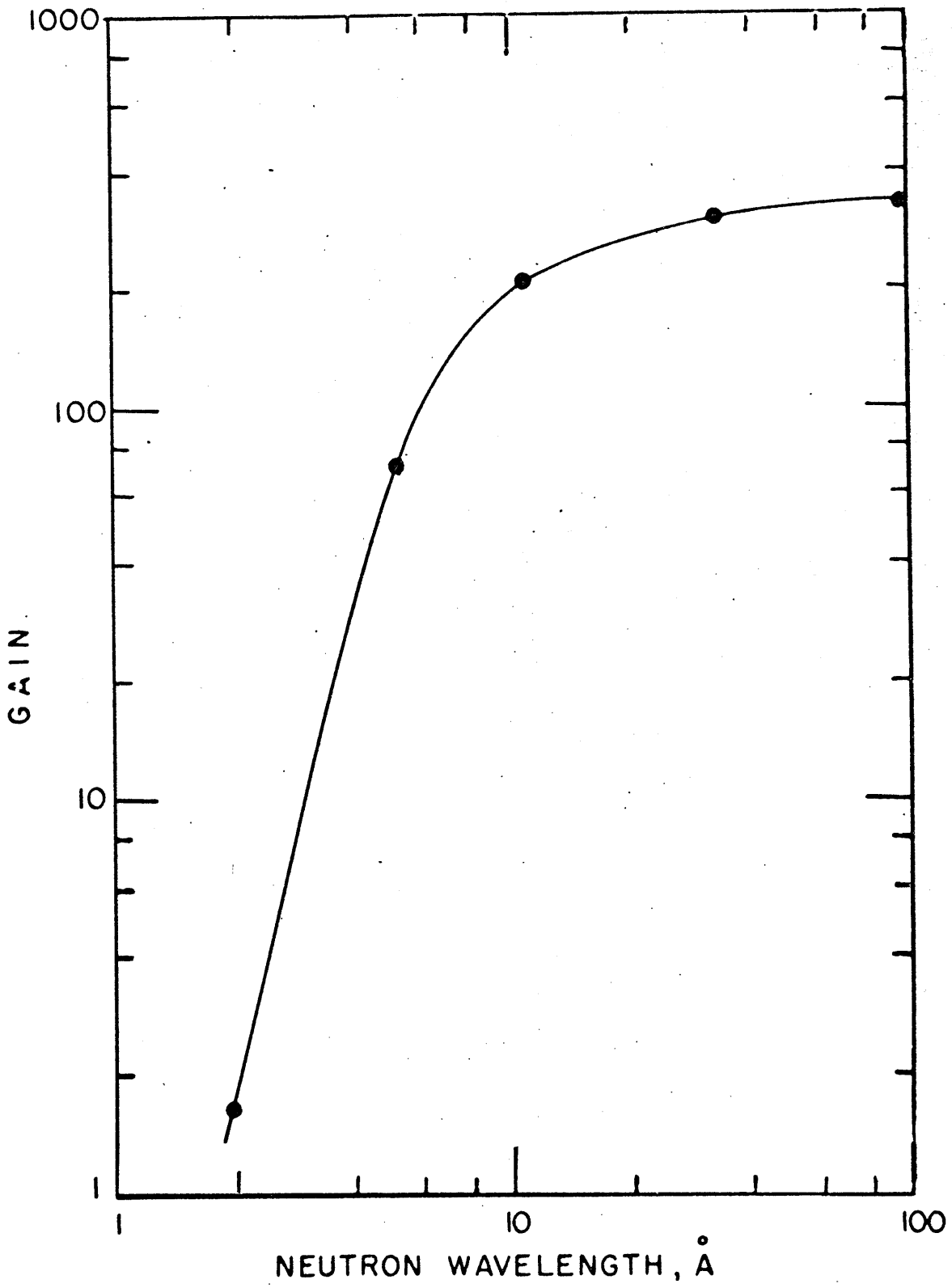

FIG. 7.8. COLD NEUTRON GAIN

6 Å is greater than 100 as compared with a flux weighted gain of about 65 for all neutrons with wavelengths greater than 3.96 Å. This is due to the fact that the flux of neutrons with a wavelength that is longer than about 20 Å is less than $\frac{1}{10}$ the peak flux (4.95Å).

Shown in figure 7.9 is the cold neutron gain as a function of cold moderator size. The calculations have been done using pure D_2O with an effective mass equal to that of the liquid, and the cooling coils not included. As is expected there is an initial rapid increase in gain due to more complete moderation as the volume gets larger. At a volume of about 30 liters the gain levels off indicating that no additional moderation can be achieved by increasing the volume beyond this point. The volume of the present cold moderator is about 15 liters, which gives a gain that is approximately 93% of that obtainable with a volume of 30 liters.

Van Dingenen (29) shows similar results as those shown in figure 7.9. His calculations are based on a maxwellian distribution for the moderated neutrons and for D_2O give a maximum cold neutron gain at a radius of about 20 centimeters. This is in good agreement with the results shown in figure 7.9.

Webb (27) shows measured cold neutron gains as a function of wavelength for a cylinder of liquid hydrogen 8 centimeters in diameter. Except for magnitude the gain follows the same trend as that shown in figure 7.8

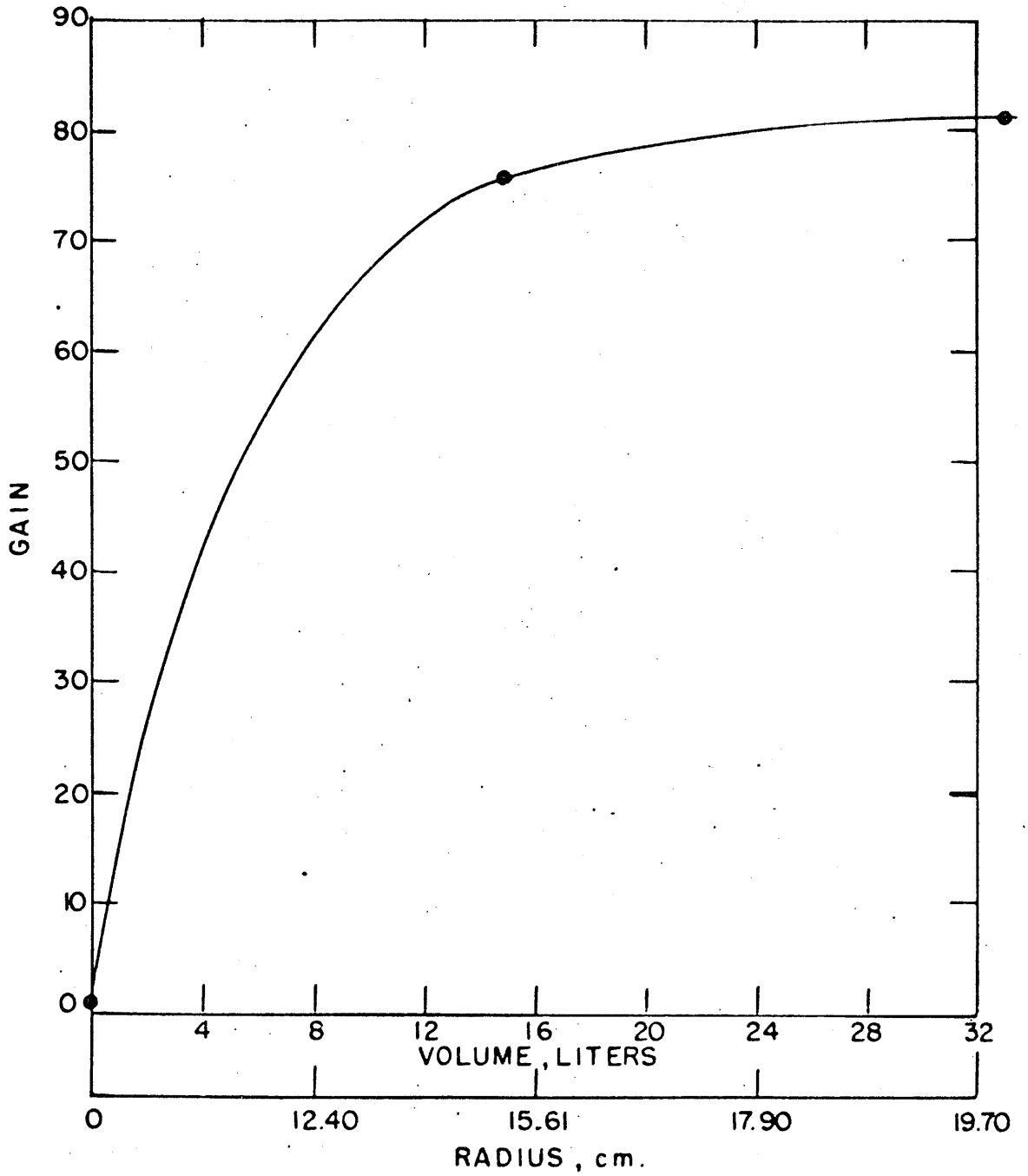

FIG. 7.9 COLD NEUTRON GAIN

7.3. Comparison with Experiment

The calculated neutron spectra as a function of neutron wavelength are shown in figure 7.10. If the neutron energy distribution in the cold moderator could be characterized by a maxwellian distribution at the temperature of the moderator, one would expect all the neutrons to be shifted toward longer wavelengths. However, the calculations indicate that in the real situation of a finite cold moderator located in a flux of thermal neutrons there is very little shift in the short wavelength neutrons (less than about 1 Å). This is in agreement with the experimental results of section 6.3. As can be seen in figure 6.10 there is no apparent shift in the neutron spectrum for wavelengths less than about 1 Å and that the shift becomes greater as the wavelength increases. This trend is the same as that shown in figure 7.10. It should also be noted that the calculated spectra falls below the maxwellian distribution for the long wavelength neutrons. This again agrees with the results presented in section 6.3.

The calculated neutron spectrum using the effective masses of the liquids and the estimated effective masses of the ices is shown in figure 7.10. For short wavelengths the spectrum is independent of the effective mass; however, for wavelengths greater than about 1 Å, the smaller effective mass gives a greater shift towards longer wavelengths. This is expected because of the higher slowing down power of a lighter nucleus.

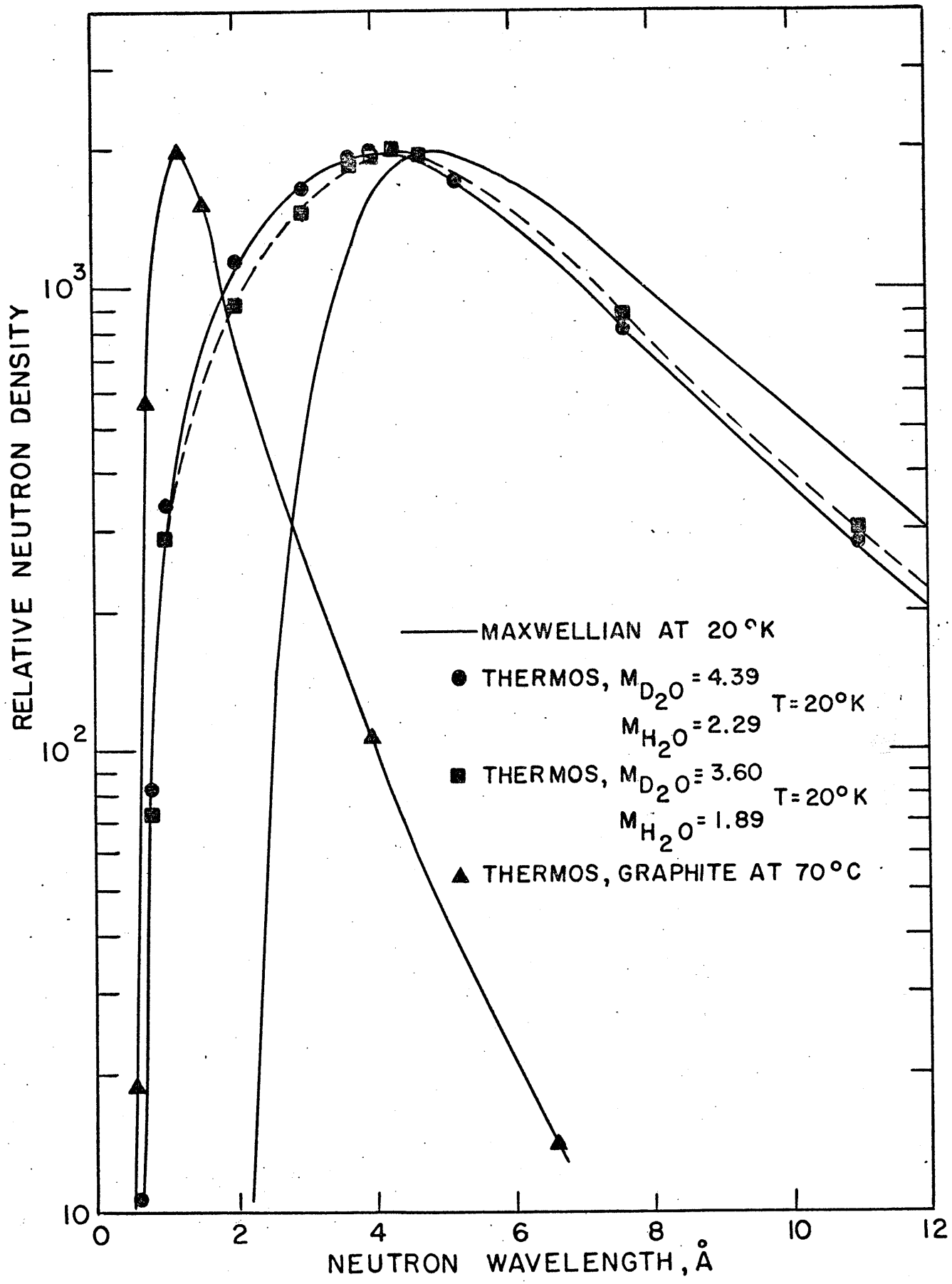

FIG. 7.10 NEUTRON WAVELENGTH DISTRIBUTIONS

Shown in figure 7.11 is the measured and calculated neutron spectrum in the warm graphite. For long wavelengths the calculated spectrum nearly falls within the uncertainty of the measured spectrum. The apparent shift towards shorted wavelengths is expected because of the 1/v dependent neutron absorption in aluminum which was not accounted for in the thermos calculation.

For long wavelengths both the measured and calculated neutron spectra have a shape which is very nearly the same as a maxwellian distribution. Assuming the shape is maxwellian, the cold neutron gain at a given wavelength can be written as

$$G(T) = \left(\frac{T_o}{T}\right)^{3/2} \exp\left\{\left[\frac{1-\frac{T_o}{T}}{1-\frac{T_o}{T_1}}\right] \ln\left[\left(\frac{T_1}{T_o}\right)^{3/2} G(T_1)\right]\right\} \qquad (7.3)$$

where $G(T_1)$ = gain at Temperature T_1

T_o = Temperature of warm spectrum.

From the data in section 6.3 the gain in 5 Å neutrons at -40°C is estimated to be about 1.77. By using this and equation (7.3) the gain in 5 Å at 20°K is estimated to be about 52. The calculated gain in 5 Å neutrons at 20°K is approximately 65, or about 25% higher than the gain estimated from the experimental data.

The shapes of the neutron spectra calculated with Thermos agree reasonably well with the measured spectra; however, the calculated cold neutron gains appear to be too high. This is expected to be due to using too small of an effective mass in the Thermos calculations.

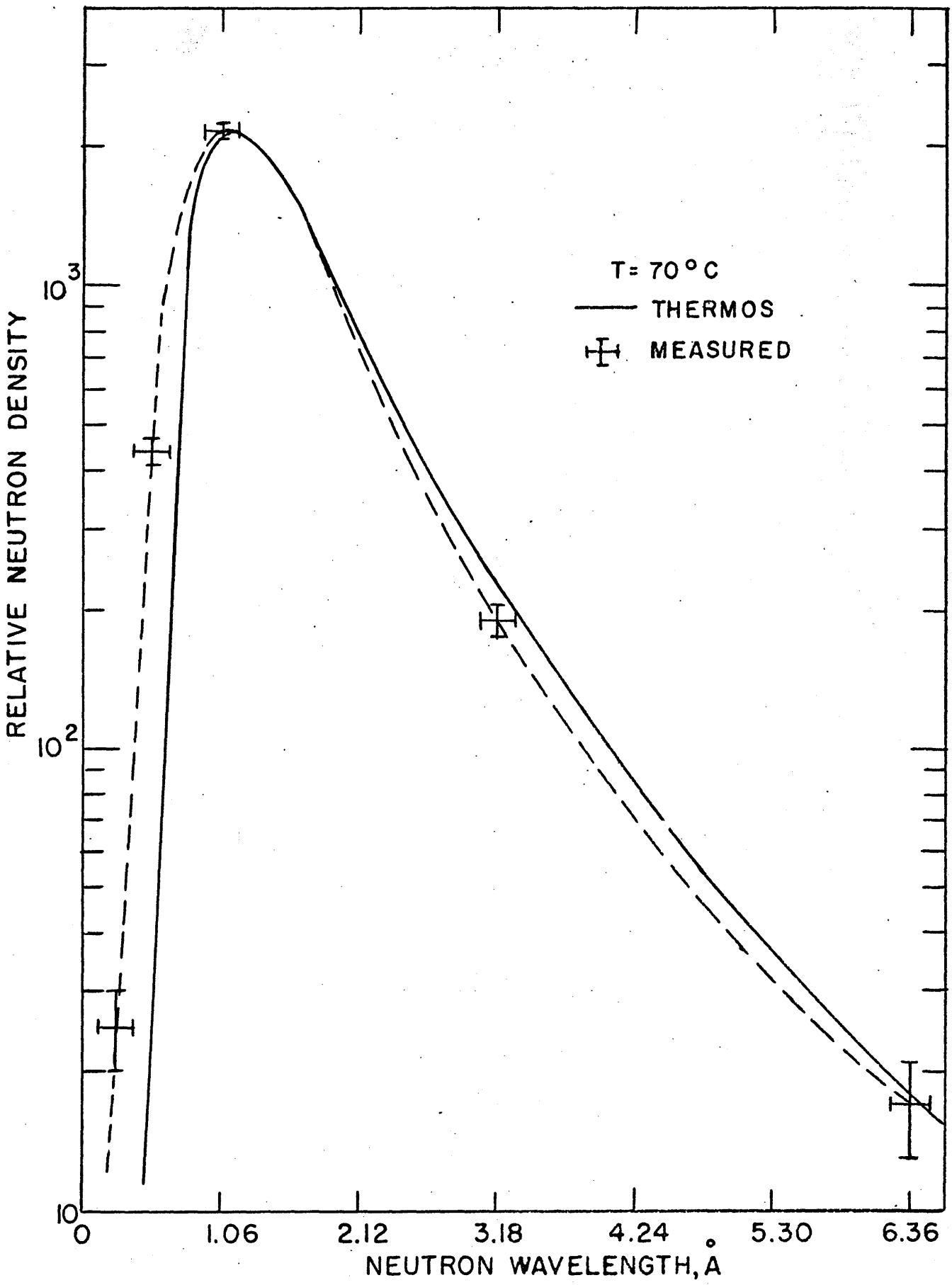

FIG. 7.11 NEUTRON SPECTRUM IN WARM GRAPHITE

Chapter 8

Conclusions and Recommendations for Future Work

8.1. Conclusions

A new design for the MIT reactor thermal column has been developed to optimize the number of thermal neutrons available for slowing down in the cold neutron cryostat. It has been found that by creating a cavity in the thermal column with graphite walls approximately eight inches thick, the thermal flux can be increased by a factor of about 30. Since the cold moderator is a good scatterer, its presence in the cavity will not greatly reduce the magnitude of the thermal flux incident on it, but will cause the incident flux on the reactor side of the cryostat to be approximately 60% higher than the incident flux on the side away from the reactor.

The effect of such a cavity on the lattice facility, located at the end of the thermal column, has also been investigated. It has been found that the cavity will reduce the cadmium ratio in the lattice facility from a value of about 1700 to approximately 460; however, it is felt that this value is sufficiently high for the experiments carried out in this facility.

The model used for the above calculations has been compared with experimental results and Monte Carlo calculations. The agreement with both has been very good; therefore, it is felt that the predicted effects of a cavity in the thermal column

are reasonably accurate.

A large volume cold neutron cryostat has been designed, built, and tested in the present reactor thermal column. The cold moderator is a one foot diameter sphere of D_2O ice cooled with cold gaseous helium. The preliminary testing indicates that the predicted gamma and neutron heating in the cryostat may be high by a factor of about 1.7. It has been found that good temperature and vacuum monitoring instrumentation is necessary to assure proper operation of the cryostat. It has also been found that to prevent excess stresses in the aluminum sphere and cooling coils it may be necessary to freeze the D_2O ice in layers.

Neutron energy spectra have been measured using the time of flight technique. Due to a vacuum leak which occurred during cool down, the cold moderator temperature was limited to a -40°C; however, even at this relatively high temperature, a definite increase in long wavelength neutrons was observed.

Expected neutron energy spectra in the cold moderator have been determined using the thermalization code THERMOS with the Brown St. John scattering Kernel. It has been found that the code predicts the trends observed in the measured spectra; however, it over estimates the observed gain in long wavelength neutrons. Since the calculations are very sensitive to the effective mass used in the scattering Kernel, it is felt that the discrepancy between theory and experiment is mainly due to using too small of an effective mass for the D_2O ice.

8.2. Recommendations for Future Work

The major source of heating in the cold moderator is the core gamma rays. In the present thermal column this heating is tolerable because of the shielding provided by the graphite between the reactor core and the cryostat. However, with the proposed cavity in the thermal column most of this graphite will be removed and the core gamma heating may be excessive. To reduce this heating to a tolerable level, it may be necessary to locate a bismuth shield in the graphite reflector of the reactor between the core and the cryostat.

The initial tests indicate that the cold neutron cryostat is effective in increasing the number of long wavelength neutrons. Since the goal of these measurements was only to prove that the cold moderator does indeed increase the number of cold neutrons, no corrections were made to the data. To determine exact cold neutron gains it will be necessary to correct the measured neutron spectra for such things as counter efficiency, flight path attenuation, chopper transmission, and neutron leakage current from the cold moderator. It will also be necessary to have a spectrometer designed specifically for low energy neutrons. Since the neutrons of interest are those having energies less than that of the beryllium cut-off, it would be desirable to eliminate the higher energy neutrons through the use of a beryllium filter.

The initial testing also indicates that some modifications must be made on the cryostat. The following are suggested:

Redesign the sample holder, 3" shield plug, and gas seal to permit easy insertion and withdrawal of the D_2O, and to allow for freezing the D_2O in layers.

Use clad thermocouples in the sphere to prevent contamination of the moderator.

Develop an ozone detector to be located in the vacuum jacket.

Set up a permanent instrumentation panel to allow for easy and continuous monitoring of temperatures, vacuum pressure, and helium flow.

Once a good spectrometer has been developed and experience has been gained in operating the cryostat, the following measurements are recommended:

Measure neutron spectrum as a function of distance in the cold moderator to determine optimum location of a re-entrant port.

Use cold neutron beam from cryostat to measure low temperature cross sections of D_2O and H_2O.

With the above information determine an effective mass for the moderator which will give agreement between theory and experiment.

Appendix A

Calculation of View Factors

This appendix discusses the calculation of the view factors used in the computer program for calculating the thermal neutron fluxes on the surfaces of a cavity lined with a reflective material. Section A.1 gives the derivation for view factors for square subareas on parallel planes, section A.2 gives the derivation for view factors for square subareas on perpendicular planes, and section A.3 discusses the computer program used to calculate the view factors.

A.1. View Factors for Parallel Planes

Consider two subareas, A_1 and A_2, on parallel planes, as shown in figure A.1. C is the perpendicular distance between the planes; A is the distance between the nearest vertical edges of the subareas; B is the distance between the nearest horizontal edges of the subareas, and L is the length of the sides of the subareas.

Consider now a differential area dA_1 located at (x,y) on subarea A_1, and a differential area dA_2 located at (s,t) on subarea A_2. The view factor from dA_1 to dA_2 is given by (1).

$$A_1 d^2(F_{12}) = \frac{\cos\phi_1 \cos\phi_2}{\pi r^2} \, dA_2 dA_1 \qquad (A.1)$$

where ϕ_1 is the angle between the normal to dA_1 and r

ϕ_2 is the angle between the normal to dA_2 and

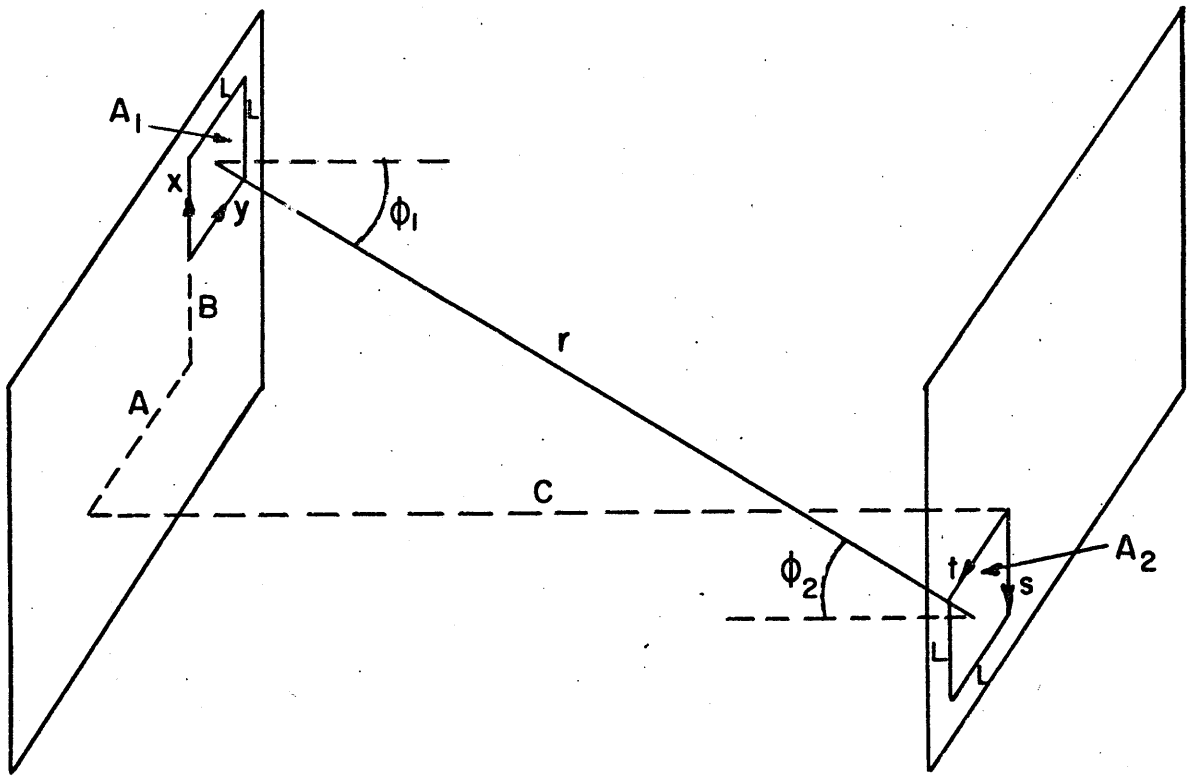

FIG. A.I SUBAREAS ON PARALLEL PLANES

r is the distance between dA_1 and dA_2.

Integrating the above equation over A_2 gives the view factor between dA_1 and A_2, or

$$A_1 \frac{d(F_{12})}{dA_1} = \int_{A_2} \frac{\cos\phi_1 \cos\phi_2}{\pi r^2} \, dA_2. \tag{A.2}$$

Let $u = A+y+t$

$v = B+X+S$

Then, $r^2 = u^2+v^2+C^2$

$\cos\phi_1 = C/r = C/[u^2+v^2+C^2]^{1/2}$

$\cos\phi_2 = C/r = C/[u^2+v^2+C^2]^{1/2}$

$dA_2 = dsdt = dvdu$.

Substituting into equation (A.2) gives

$$A_1 \frac{d(F_{12})}{dA_1} = \frac{C^2}{\pi} \int_{A+y}^{A+y+L} du \int_{B+X}^{B+X+L} \frac{dv}{[u^2+v^2+C^2]^2} . \tag{A.3}$$

Integration gives,

$$A_1 \frac{d(F_{12})}{dA_1} = \frac{1}{2\pi} \Bigg[\frac{B+X+L}{[C^2+(B+X+L)^2]^{1/2}} \left[\mathrm{Tan}^{-1}\left(\frac{A+y+L}{[C^2+(B+X+L)^2]^{1/2}} \right) - \mathrm{Tan}^{-1}\left(\frac{A+y}{[C^2+(B+X+L)^2]^{1/2}} \right) \right]$$

$$- \frac{B+X}{[C^2+(B+X)^2]^{1/2}} \left[\mathrm{Tan}^{-1}\left(\frac{A+y+L}{[C^2+(B+X)^2]^{1/2}} \right) - \mathrm{Tan}^{-1}\left(\frac{A+y}{[C^2+(B+X)^2]^{1/2}} \right) \right]$$

$$+ \frac{A+y+L}{[C^2+(A+y+L)^2]^{1/2}} \left[\mathrm{Tan}^{-1}\left(\frac{B+X+L}{[C^2+(A+y+L)^2]^{1/2}} \right) - \mathrm{Tan}^{-1}\left(\frac{B+X}{[C^2+(A+y+L)^2]^{1/2}} \right) \right]$$

$$- \frac{A+y}{[C^2+(A+y)^2]^{1/2}}\left[\mathrm{Tan}^{-1}\left(\frac{B+X+L}{[C^2+(A+y)^2]^{1/2}}\right) - \mathrm{Tan}^{-1}\left(\frac{B+X}{[C^2+(A+y)^2]^{1/2}}\right)\right] . \tag{A.4}$$

Integration of this over $dA_1 = dxdy$ gives the view factor between A_1 and A_2,

$$A_1F_{12} = \int_0^L dx \int_0^L dy \frac{d(F_{12})}{dA_1} . \tag{A.5}$$

Carrying out the integration results in,

$$2\pi F_{12} = (I+2)\{[K^2+(J+2)^2]^{1/2}\mathrm{Tan}^{-1}\left(\frac{I+2}{[K^2+(J+1)^2]^{1/2}}\right) - 2[K^2+(J+1)^2]^{1/2}$$

$$\mathrm{Tan}^{-1}\left(\frac{I+2}{[K^2+(J+1)^2]^{1/2}}\right) + [K^2+J^2]^{1/2}\mathrm{Tan}^{-1}\left(\frac{I+2}{[K^2+J^2]^{1/2}}\right)\}$$

$$+ I\{[K^2+(J+2)^2]^{1/2}\mathrm{Tan}^{-1}\left(\frac{I}{[K^2+(J+2)^2]^{1/2}}\right)$$

$$-2[K^2+(J+1)^2]^{1/2}\mathrm{Tan}^{-1}\left(\frac{I}{[K^2+(J+1)^2]^{1/2}}\right)+[K^2+J^2]^{1/2}$$

$$\mathrm{Tan}^{-1}\left(\frac{I}{[K^2+J^2]^{1/2}}\right)\}+(J+2)\{[K^2+(I+2)^2]^{1/2}$$

$$\mathrm{Tan}^{-1}\left(\frac{J+2}{[K^2+(I+2)^2]^{1/2}}\right) -2[K^2+(I+1)^2]^{1/2}$$

$$\mathrm{Tan}^{-1}\left(\frac{J+2}{[K^2+(I+1)^2]^{1/2}}\right) +[K^2+I^2]^{1/2}\mathrm{Tan}^{-1}\left(\frac{J+2}{[K^2\cdot I^2]^{1/2}}\right)\}$$

$$+J\{[K^2+(I+2)^2]^{1/2}\mathrm{Tan}^{-1}\left(\frac{J}{[K^2+(I+2)^2]^{1/2}}\right)-2[K^2+(I+1)^2]^{1/2}$$

$$\text{Tan}^{-1}\left(\frac{J}{[K^2+(I+1)^2]^{1/2}}\right)+[K^2+I^2]\text{Tan}^{-1}\left(\frac{J}{[K^2+I^2]^{1/2}}\right)\}$$

$$-2(I+1)\{[K^2+(J+2)^2]^{1/2}\text{Tan}^{-1}\left(\frac{I+1}{[K^2+(J+2)^2]^{1/2}}\right)$$

$$-2[K^2+(J+1)^2]^{1/2}\text{Tan}^{-1}\left(\frac{I+1}{[K^2+(J+1)^2]^{1/2}}\right)+[K^2+J^2]^{1/2}$$

$$\text{Tan}^{-1}\left(\frac{I+1}{[K^2+J^2]^{1/}}\right)\}-2(J+1)\{[K^2+(I+2)^2]^{1/2}$$

$$\text{Tan}^{-1}\left(\frac{J+1}{[K^2+(I+2)^2]^{1/2}}\right)-2[K^2+(I+1)^2]^{1/2}\text{Tan}^{-1}$$

$$\left(\frac{J+1}{[K^2+(I+1)^2]^{1/2}}\right)+[K^2+I^2]^{1/2}\text{Tan}^{-1}\left(\frac{J+1}{[K^2+J^2]^{1/2}}\right)\}$$

$$-\frac{K^2}{2}\ln\{\frac{[K^2+I^2+(J+2)^2][K^2+J^2+(I+2)^2][K^2+I^2+J^2]}{[K^2+I^2+(J+1)^2]^2[K^2+J^2+(I+1)^2]^2[K^2+(I+2)^2+(J+1)^2]^2}$$

$$X\ \frac{[K^2+(I+2)^2+(J+2)^2][K^2+(I+1)^2+(J+1)^2]^4}{[K^2+(I+1)^2+(J+2)^2]^2}\}\qquad(A.6)$$

where, $K = C/L$

$I = A/L$

$J = B/L.$

A.2. View Factors for Perpendicular Planes

Consider two subareas, A_1 and A_2, on perpendicular planes, as shown in figure A.2. C is the distance from the line of intersection of the planes to the near edge of A_2; B is the distance from the line of intersection of the planes to the near edge of A_1; A is the vertical separation of the near edges of A_1 and A_2; and L is the length of the sides of the subareas.

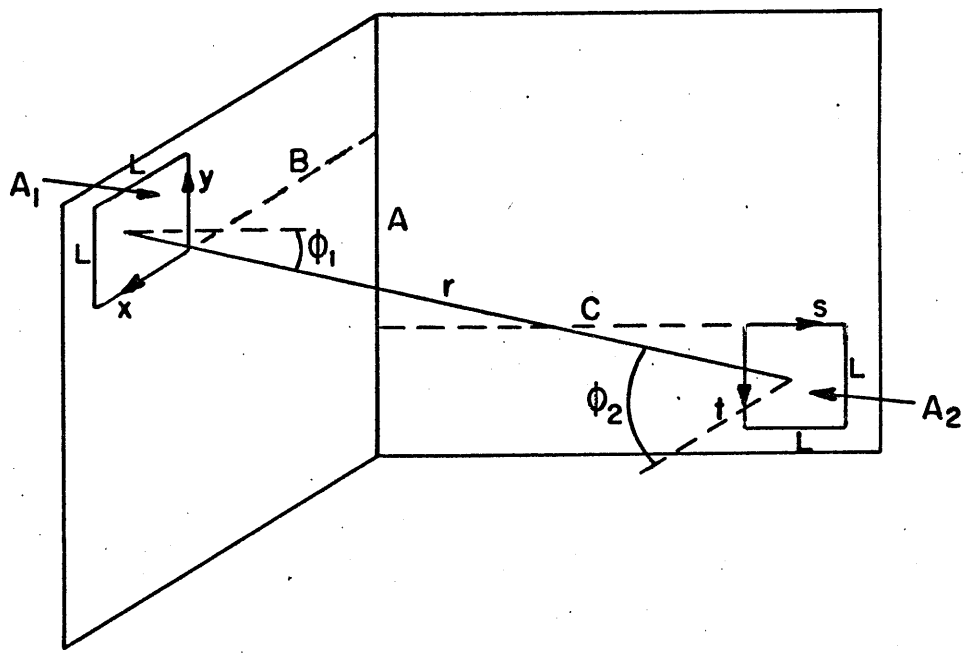

FIG. A.2 SUBAREAS ON PERPENDICULAR PLANES

Consider now a differential area dA_1 located at (x,y) on subarea A_1, and a differential area dA_2 located at (s,t) on subarea A_2. The view factor from dA_1 to dA_2 is given by

$$A_1 d^2(F_{12}) = \frac{\cos\phi_1 \cos\phi_2}{\pi r^2} \, dA_2 dA_1 \tag{A.7}$$

where ϕ_1 is the angle between the normal to dA_1 and r

ϕ_2 is the angle between the normal to dA_2 and r

r is the distance between dA_1 and dA_2.

Integrating over A_2 gives the view factor from dA_1 to A_2 or,

$$A_1 \frac{d(F_{12})}{dA_1} = \int_{A_2} \frac{\cos\phi_1 \cos\phi_2}{\pi r^2} \, dA_2 \, . \tag{A.8}$$

Let $u = A+y+t$

$v = C+S$

$Z = B+X$,

Then $r^2 = [u^2+v^2+Z^2]^2$

$\cos\phi_1 = v/r = v/[u^2+v^2+Z^2]^{1/2}$

$\cos\phi_2 = Z/r = Z/[u^2+v^2+Z^2]^{1/2}$

$dA_2 = dvdu$.

Substituting into equation (A.8) gives,

$$A_1 \frac{d(F_{12})}{dA_1} = \frac{Z}{\pi} \int_C^{C+L} dv \int_{A+y}^{A+y+L} \frac{vdu}{[u^2+v^2+Z^2]^2} \, . \tag{A.9}$$

Integration gives,

$$\frac{d(F_{12})}{dA_1} = \frac{Z}{2\pi}\left\{\frac{1}{[C^2+Z^2]^{1/2}} \mathrm{Tan}^{-1}\left(\frac{A+y+L}{[C^2+Z^2]^{1/2}}\right) - \frac{1}{[(C+L)^2+Z^2]^{1/2}}\right.$$

$$\left. \mathrm{Tan}^{-1}\left(\frac{A+y+L}{[(C+L)^2+Z^2]^{1/2}}\right) - \frac{1}{[C^2+Z^2]^{1/2}} \mathrm{Tan}^{-1}\left(\frac{A+y}{[C^2+Z^2]^{1/2}}\right)\right.$$

$$+\frac{1}{[(C+L)^2+z^2]^{1/2}}\,\mathrm{Tan}^{-1}\left(\frac{A+y}{[(C+L)^2+z^2]^{1/2}}\right)\}\,. \qquad (A.10)$$

Integration of this over $dA_1 = dxdy = dzdy$ gives the view factor from A_1 to A_2,

$$A_1F_{12} = \int_0^L dy \int_B^{B+L} \frac{d(F_{12})}{dA_1}\,dz. \qquad (A.11)$$

Carrying out the integration results in,

$$2\pi F_{12} = (I+2)\{[K^2+(J+1)^2]^{1/2}\mathrm{Tan}^{-1}\left(\frac{I+2}{[K^2+(J+1)^2]^{1/2}}\right) - [J^2+K^2]^{1/2}$$

$$\mathrm{Tan}^{-1}\left(\frac{I+2}{[J^2+K^2]^{1/2}}\right)+[J^2+(K+1)^2]^{1/2}\mathrm{Tan}^{-1}\left(\frac{I+2}{[J^2+(K+1)^2]^{1/2}}\right)$$

$$-[(J+1)^2+(K+1)^2]^{1/2}\mathrm{Tan}^{-1}\left(\frac{I+2}{[(J+1)^2+(K+1)^2]^{1/2}}\right)\}+2(I+1)$$

$$\{[J^2+K^2]^{1/2}\mathrm{Tan}^{-1}\left(\frac{I+1}{[J^2+K^2]^{1/2}}\right) - [K^2+(J+1)^2]^{1/2}\mathrm{Tan}^{-1}$$

$$\left(\frac{I+1}{[K^2+(J+1)^2]^{1/}}\right)+[(J+1)^2+(K+1)^2]^{1/2}\mathrm{Tan}^{-1}\left(\frac{I+1}{[(J+1)^2+(K+1)^2]^{1/2}}\right)$$

$$-[J^2+(K+1)^2]^{1/2}\mathrm{Tan}^{-1}\left(\frac{I+1}{[J^2+(K+1)^2]^{1/2}}\right)\}+I\{[J^2+(K+1)^2]^{1/2}$$

$$\mathrm{Tan}^{-1}\left(\frac{I}{[J^2+(K+1)^2]^{1/2}}\right)-[J^2+K^2]^{1/2}\mathrm{Tan}^{-1}\left(\frac{I}{[J^2+K^2]^{1/2}}\right)$$

$$+[K^2+(J+1)^2]^{1/2}\mathrm{Tan}^{-1}\left(\frac{I}{[K^2+(J+1)^2]^{1/2}}\right)-[(J+1)^2+(K+1)^2]^{1/2}$$

$$\mathrm{Tan}^{-1}\left(\frac{I}{[(J+1)^2+(K+1)^2]^{1/2}}\right)+\frac{(I+2)^2}{4}\,\ln$$

$$\left\{\frac{[(I+2)^2+(J+1)^2+K^2][(I+2)^2+J^2+(K+1)^2]}{[(I+2)^2+J^2+K^2][(I+2)^2+(J+1)^2+(K+1)^2]}\right\}$$

$$+\frac{(I+1)^2}{2}\,\ln\left\{\frac{[(I+1)^2+J^2+K^2][(I+1)^2+(J+1)^2+(K+1)^2]}{[(I+1)^2+(J+1)^2+K^2][(I+1)^2+J^2+(K+1)^2]}\right\}$$

$$+\frac{(J+1)^2}{4}\ln\{\frac{[(J+1)^2+K^2+(I+1)^2]^2[(J+1)^2+(K+1)^2+(I+2)^2]}{[(J+1)^2+K^2+(I+2)^2][(J+1)^2+(K+1)^2+(I+1)^2]}$$

$$\frac{[(J+1)^2+(K+1)^2+I^2]}{[(J+1)^2+K^2+I^2]}\}$$

$$+\frac{(K+1)^2}{4}\ln\{\frac{[(J+1)^2+(K+1)^2+I+2)^2][J^2+(K+1)^2+(I+1)^2]}{[J^2+(K+1)^2+(I+2)^2][(J+1)^2+(K+1)^2+(I+1)^2]^2}$$

$$\frac{[(J+1)^2+(K+1)^2+I^2]}{[J^2+(K+1)^2+I^2]}\}$$

$$+\frac{I^2}{4}\ln\{\frac{[I^2+(J+1)^2+K^2][I^2+J^2+(K+1)^2]}{[I^2+J^2+K^2][I^2+(J+1)^2+(K+1)^2]}\}$$

$$+\frac{J^2}{4}\ln\{\frac{[J^2+K^2+(I+2)^2][J^2+(K+1)^2+(I+1)^2]^2[I^2+J^2+K^2]}{[(I+1)^2+J^2+K^2]^2[(I+2)^2+(K+1)^2+J^2][(K+1)^2+J^2+I^2]}\}$$

$$+\frac{K^2}{4}\ln\{\frac{[J^2+K^2+(I+2)^2][I^2+J^2+K^2][(J+1)^2+(I+1)^2+K^2]^2}{[(J+1)^2+(I+2)^2+K^2][(J+1)^2+K^2+I^2][J^2+K^2+(I+1)^2]^2}\} \quad (A.12)$$

where, $I = A/L$

$J = B/L$

$K = C/L$.

A.3. Computer Program for Calculating View Factors

Equations (A.6) and (A.12) give the view factors between square subareas on parallel and perpendicular planes in terms of the parameters I, J, and K. Since these equations are quite tedious to evaluate by hand, and since they have to be evaluated for several values of I, J, K, it was decided to write computer programs to carry out the necessary calculations.

FRONTVIEW is the program for calculating the view factors for parallel planes, and SIDEVIEW is the program for calculating the view factors for perpendicular planes. A listing of

both programs is given in the following pages.

```
C       FRONTVIEW
C       VIEW FACTORS FOR PARALLEL PLANES
C       MAIN PROGRAM
        DIMENSION F(14,14,14)
   10 FORMAT(3H1K=I3)
   11 FORMAT(1H0,14(1X,F8.6))
        N = 14
        M = 14
        DO 50 K = 1,N
        WRITE(6,10) K
        X = K
        P1 = X*X
        DO 40 J = 1,M
        Y = J
        Q1 = Y*Y
        Q2 = (Y-1.)*(Y-1.)
        Q3 = (Y-2.)*(Y-2.)
        R1 = P1 + Q1
        R2 = P1 + Q2
        R3 = P1 + Q3
        S1 = SQRT(R1)
        S2 = SQRT(R2)
        S3 = SQRT(R3)
        DO 30 I = 1,J
        Z = I
        T1 = Z*Z
        T2 = (Z-1.)*(Z-1.)
        T3 = (Z-2.)*(Z-2.)
        R4 = P1 + T1
        R5 = P1 + T2
        R6 = P1 + T3
        S4 = SQRT(R4)
        S5 = SQRT(R5)
        S6 = SQRT(R6)
        U1 = R1 + T3
        U2 = R2 + T3
```

```
      U3 = R3 + T3
      U4 = R1 + T2
      U5 = R2 + T2
      U6 = R3 + T2
      U7 = R1 + T1
      U8 = R2 + T1
      U9 = R3 + T1
      W1 = (U1*U3*U9*U7*U5*U5*U5*U5)/(U2*U2*U6*U6*U8*U8*U4*U4)
      F1 = Z*(S1*ATAN(Z/S1) - 2.*S2*ATAN(Z/S2) + S3*ATAN(Z/S3))
      F2 = 2.*(Z-1.)*(S1*ATAN((Z-1.)/S1) - 2.*S2*ATAN((Z-1.)/S2)
     1+ S3*ATAN((Z-1.)/S3))
      F3 = (Z-2.)*(S1*ATAN((Z-2.)/S1) - 2.*S2*ATAN((Z-2.)/S2)
     1+ S3*ATAN((Z-2.)/S3))
      F4 = Y*(S4*ATAN(Y/S4) - 2.*S5*ATAN(Y/S5) + S6*ATAN(Y/S6))
      F5 = 2.*(Y-1.)*(S4*ATAN((Y-1.)/S4) - 2.*S5*ATAN((Y-1.)/S5)
     1+ S6*ATAN((Y-1.)/S6))
      F6 = (Y-2.)*(S4*ATAN((Y-2.)/S4) - 2.*S5*ATAN((Y-2.)/S5)
     1+ S6*ATAN((Y-2.)/S6))
      F7 = X*X*ALOG(W1)/2.
      F(I,J,K) = (F1-F2+F3+F4-F5+F6-F7)/(2.*3.1416)
   30 CONTINUE
      WRITE (6,11) (F(I,J,K),I = 1,J)
   40 CONTINUE
   50 CONTINUE
      END
```

```
C       SIDEVIEW
C       VIEW FACTORS FOR PERPENDICULAR PLANES
C       MAIN PROGRAM
        DIMENSION F(15,15,15)
   10   FORMAT(3H1J=I3)
   11   FORMAT(1H0,15(1X,F7.5))
        N = 15
        M = 15
        L = 15
        DO 50 J = 1,N
        WRITE(6,10) J
        X = J
        P1 = X*X
        P2 = (X-1.)*(X-1.)
        DO 40 K = J,M
        Y = K
        Q1 = Y*Y
        Q2 = (Y-1.)*(Y-1.)
        R1 = P1 + Q1
        R2 = P1 + Q2
        R3 = P2 + Q1
        R4 = P2 + Q2
        S1 = SQRT(R1)
        S2 = SQRT(R2)
        S3 = SQRT(R3)
        S4 = SQRT(R4)
        DO 30 I = 1,L
        Z = I
        T1 = R1 + Z*Z
        T2 = R2 + Z*Z
        T3 = R3 + Z*Z
        T4 = R4 + Z*Z
        U1 = R1 + (Z-1.)*(Z-1.)
        U2 = R2 + (Z-1.)*(Z-1.)
        U3 = R3 + (Z-1.)*(Z-1.)
        U4 = R4 + (Z-1.)*(Z-1.)
```

```
      V1 = R1 + (Z-2.)*(Z-2.)
      V2 = R2 + (Z-2.)*(Z-2.)
      V3 = R3 + (Z-2.)*(Z-2.)
      V4 = R4 + (Z-2.)*(Z-2.)
      W1 = (T2*T3)/(T4*T1)
      W3 = (U2*U2*T1*V1)/(T2*U1*U1*V2)
      W4 = (T1*U3*U3*V1)/(T3*U1*U1*V3)
      F4 = Z*Z*ALOG(W1)/4.
      F6 = X*X*ALOG(W3)/4.
      F7 = Y*Y*ALOG(W4)/4.
      NUM1 = J*K
      IF(NUM1 - 1) 20, 15, 20
   15 F1 = Z*(S2*ATAN(Z/S2) - S1*ATAN(Z/S1) + S3*ATAN(Z/S3))
      F2 = 2.*(Z-1.)*(S1*ATAN((Z-1.)/S1) - S2*ATAN((Z-1.)/S2)
     1- S3*ATAN((Z-1.)/S3))
      F3 = (Z-2.)*(S3*ATAN((Z-2.)/S3) - S1*ATAN((Z-2.)/S1)
     1+ S2*ATAN((Z-2.)/S2))
      IF(I .EQ. 1) GO TO 16
      W2 = (U4*U1)/(U2*U3)
      F5 = (Z-1.)*(Z-1.)*ALOG(W2)/2.
      IF(I .EQ. 2) GO TO 18
      GO TO 25
   16 F5 = 0.
      F9 = 0.
      F10 = 0.
      GO TO 27
   18 F8 = 0.
      F9 = 0.
      F10 = 0.
      GO TO 28
   20 F1 = Z*(S2*ATAN(Z/S2) - S4*ATAN(Z/S4) - S1*ATAN(Z/S1)
     1+ S3*ATAN(Z/S3))
      F2 = 2.*(Z-1.)*(S4*ATAN((Z-1.)/S4) - S2*ATAN((Z-1.)/S2)
     1+ S1*ATAN((Z-1.)/S1) - S3*ATAN((Z-1.)/S3))
      F3 = (Z-2.)*(S3*ATAN((Z-2.)/S3) - S1*ATAN((Z-2.)/S1)
     1- S4*ATAN((Z-2.)/S4) + S2*ATAN((Z-2.)/S2))
```

```
      W2 = (U4*U1)/(U2*U3)
      F5 = (Z-1.)*(Z-1.)*ALOG(W2)/2.
   25 W6 = (T4*U3*U3*V4)/(U4*U4*T3*V3)
      W7 = (T4*V4*U2*U2)/(T2*V2*U4*U4)
      F9 = (X-1.)*(X-1.)*ALOG(W6)/4.
      F10 = (Y-1.)*(Y-1.)*ALOG(W7)/4.
   27 W5 = (V2*V3)/(V4*V1)
      F8 = (Z-2.)*(Z-2.)*ALOG(W5)/4.
   28 F(K,I,J) = (F1+F2+F3+F4+F5+F6+F7+F8+F9+F10)/(2.*3.1416)
   30 CONTINUE
      WRITE (6,11) (F(K,I,J),I = 1,L)
   40 CONTINUE
   50 CONTINUE
      END
```

Appendix B

Computer Programs for Calculating Fluxes in a Cavity

This appendix discusses the computer program used to calculate the neutron fluxes on the surfaces of a hollow cavity surrounded by reflective walls. Section B.1 discusses HOLCAV, used for empty cavities, and Section B.2 discusses TARGET, a modification to handle cavities surrounding objects.

B.1. HOLCAV

HOLCAV is a computer program using an iteration technique to solve equation (2.14) as discussed in Section 2.2. Below is a listing of the symbols used in HOLCAV:

GN(JN,KN) = neutron current incident on a subarea located at (JN, KN) on face N.

BN(JN,KN) = albedo for a subarea located at (JN,KN) on face N

SO(J1,K1) = source ($n/cm^2 \cdot sec$) for a subarea located at (J1,K1) on face 1.

CN(JN,KN) = calculated neutron current incident on a subarea located at (JN,KN) on face N. Becomes GN(JN,KN) at start of next iteration.

NCN(JN,KN) = CN(JN,KN)*(1-BN(JN,KN)) = net current through a subarea located at (JN,KN) on face N.

PHN(JN,KN) = CN(JN,KN)*(1+BN(JN,KN)) = neutron flux on a subarea located at (JN,KN) on face N.

FL(L1,L2,L3) = view factor between subareas on parallel planes.

FP(L1,L2,L3) = view factor between subareas on perpendicular planes.

L1,L2, and L3 = coordinates describing the relative positions of the subareas under consideration. (See Section 2.2)

HN = maximum value of KN on face N.

WN = maximum value of JN on face N

B.2. TARGET

TARGET is a modification to HOLCAV for the purpose of calculating the neutron flux on a plane of reflecting material located inside of a cavity. The procedure by which this is done is discussed in Chapter 4 and will not be repeated here.

In addition to the symbols used in HOLCAV, the following symbols are used in TARGET.

GMI(JI,KI,N) = neutron current incident on a subarea located at (JI,KI) on face I of cavity N.

BMI(JI,KI,N) = albedo of a subarea located at (JI,KI) on face I of cavity N.

SOM(J1,K1,N) = source ($n/cm^2 \cdot sec$) for a subarea located at (J1,K1) on face 1 of cavity N.

PHM(JI,KI,N) = neutron flux on a subarea located at (JI,KI) on face I of cavity N.

CMI(JI,KI,N) = calculated neutron current incident on a subarea located at (JI,KI) on face I of cavity N. Becomes GMI(JI,KI,N) for start of next iteration.

NCM2(J2,K2,N) = CM2(J2,K2,N) = net current through a subarea located at (J2,K2) on face 2 of cavity N.

TSOM(N) = sum of source terms for cavity N.

TCMI(N) = total net current through face I of cavity N.

TCM21(N) = total net current of neutrons passing from cavity N to cavity NH.

NMAX = total number of cavities = 2

KIMAX (N) = maximum value for KI on face I of cavity N.

JIMAX(N) = maximum value for JI on face I of cavity N.

```
C      HOLCAV
C      CURRENTS IN HOLLOW RECTANGULAR CAVITY
C      THERMAL COLUMN WATER PIPES
       DIMENSION G1(10,10),G2(10,10),G3(10,10),G4(10,10),G5(10,10),
      1G6(10,10),B1(10,10),B2(10,10),B3(10,10),B4(10,10),B5(10,10),
      1B6(10,10),C1(10,10),C2(10,10),C3(10,10),C4(10,10),C5(10,10),
      1C6(10,10),NC1(10,10),NC2(10,10),NC3(10,10),NC4(10,10),NC5(10,10),
      1NC6(10,10),S0(10,10),FL(10,10,10),FP(10,10,10),PH1(10,10),
      1PH2(10,10),PH3(10,10),PH4(10,10),PH5(10,10),PH6(10,10)
    1 FORMAT(39H1           CURRENT INCIDENT ON FACE ONE)
    2 FORMAT(39H1           CURRENT INCIDENT ON FACE TWO)
    3 FORMAT(41H1           CURRENT INCIDENT ON FACE THREE)
    4 FORMAT(40H1           CURRENT INCIDENT ON FACE FOUR)
    5 FORMAT(40H1           CURRENT INCIDENT ON FACE FIVE)
    6 FORMAT(39H1           CURRENT INCIDENT ON FACE SIX)
    8 FORMAT(1H0,10(F12.5))
   10 FORMAT(36H1           NET CURRENT THRU FACE ONE)
   11 FORMAT(36H1           NET CURRENT THRU FACE TWO)
   12 FORMAT(38H1           NET CURRENT THRU FACE THREE)
   13 FORMAT(37H1           NET CURRENT THRU FACE FOUR)
   14 FORMAT(37H1           NET CURRENT THRU FACE FIVE)
   15 FORMAT(36H1           NET CURRENT THRU FACE SIX)
   16 FORMAT(9F8.5)
   17 FORMAT(1H0,15F8.5)
      INTEGER H1,W1,H2,W2,H3,W3,H4,W4,H5,W5,H6,W6
      REAL NC1, NC2, NC3, NC4, NC5, NC6
      H1=8
      W1=8
      H2=8
      W2=8
      H3=8
      W3=8
      H4=8
      W4=8
      H5=8
      W5=8
```

```
      H6=8
      W6=8
      DO 21 K1=1,H1
      READ(5,16) (G1(J1,K1),B1(J1,K1),SO(J1,K1), J1=1,W1)
      WRITE(6,17) (G1(J1,K1),B1(J1,K1),SO(J1,K1), J1=1,W1)
   21 CONTINUE
      DO 22 K2=1,H2
      READ(5,16) (G2(J2,K2),B2(J2,K2), J2=1,W2)
      WRITE(6,17) (G2(J2,K2),B2(J2,K2), J2=1,W2)
   22 CONTINUE
      DO 23 K3=1,H3
      READ(5,16) (G3(J3,K3),B3(J3,K3), J3=1,W3)
      WRITE(6,17) (G3(J3,K3),B3(J3,K3), J3=1,W3)
   23 CONTINUE
      DO 24 K4=1,H4
      READ(5,16) (G4(J4,K4),B4(J4,K4), J4=1,W4)
      WRITE(6,17) (G4(J4,K4),B4(J4,K4), J4=1,W4)
   24 CONTINUE
      DO 25 K5=1,H5
      READ(5,16) (G5(J5,K5),B5(J5,K5), J5=1,W5)
      WRITE(6,17) (G5(J5,K5),B5(J5,K5), J5=1,W5)
   25 CONTINUE
      DO 26 K6=1,H6
      READ(5,16) (G6(J6,K6),B6(J6,K6), J6=1,W6)
      WRITE(6,17) (G6(J6,K6),B6(J6,K6), J6=1,W6)
   26 CONTINUE
      L3=8
      DO 28 L2=1,10
      READ(5,16) (FL(L1,L2,L3), L1=1,10)
      WRITE(6,17) (FL(L1,L2,L3), L1=1,10)
   28 CONTINUE
      L3=8
      DO 29 L2=1,10
      READ(5,16) (FL(L1,L2,L3), L1=1,10)
      WRITE(6,17) (FL(L1,L2,L3), L1=1,10)
   29 CONTINUE
```

```
      DO 31 L3=1,10
      DO 30 L2=1,10
      READ(5,16) (FP(L1,L2,L3), L1=1,10)
      WRITE(6,17) (FP(L1,L2,L3), L1=1,10)
   30 CONTINUE
   31 CONTINUE
C     MAIN PROGRAM
   40 DO 101 K1=1,H1
      DO 100 J1=1,W1
      L3=W4
      S2=0.
      DO 51 K2=1,H2
      L2=1+IABS(K2-K1)
      DO 50 J2=1,W2
      L1=1+IABS(J2-J1)
      S=B2(J2,K2)*FL(L1,L2,L3)*G2(J2,K2)
      S2=S2+S
   50 CONTINUE
   51 CONTINUE
      L3=W1+1-J1
      S3=0.
      DO 61 K3=1,H3
      L2=1+IABS(K3-K1)
      DO 60 J3=1,W3
      L1=J3
      S=B3(J3,K3)*FP(L1,L2,L3)*G3(J3,K3)
      S3=S3+S
   60 CONTINUE
   61 CONTINUE
      L3=J1
      S4=0.
      DO 71 K4=1,H4
      L2=1+IABS(K4-K1)
      DO 70 J4=1,W4
      L1=J4
      S=B4(J4,K4)*FP(L1,L2,L3)*G4(J4,K4)
```

```
      S4=S4+S
   70 CONTINUE
   71 CONTINUE
      L3=H1+1-K1
      S5=0.
      DO 81 J5=1,W5
      L2=1+IABS(J5-J1)
      DO 80 K5=1,H5
      L1=K5
      S=B5(J5,K5)*FP(L1,L2,L3)*G5(J5,K5)
      S5=S5+S
   80 CONTINUE
   81 CONTINUE
      L3=K1
      S6=0.
      DO 91 J6=1,W6
      L2=1+IABS(J6-J1)
      DO 90 K6=1,H6
      L1=K6
      S=B6(J6,K6)*FP(L1,L2,L3)*G6(J6,K6)
      S6=S6+S
   90 CONTINUE
   91 CONTINUE
      C1(J1,K1)=(S2+S3+S4+S5+S6)
  100 CONTINUE
  101 CONTINUE
      DO 201 K2=1,H2
      DO 200 J2=1,W2
      L3=W4
      S1=0.
      DO 151 K1=1,H1
      L2=1+IABS(K2-K1)
      DO 150 J1=1,W1
      L1=1+IABS(J2-J1)
      S=FL(L1,L2,L3)*(B1(J1,K1)*G1(J1,K1)+S0(J1,K1))
      S1=S1+S
```

```
150 CONTINUE
151 CONTINUE
    L3=W2+1-J2
    S3=0.
    DO 161 K3=1,H3
    L2=1+IABS(K3-K2)
    DO 160 J3=1,W3
    L1=W3+1-J3
    S=B3(J3,K3)*FP(L1,L2,L3)*G3(J3,K3)
    S3=S3+S
160 CONTINUE
161 CONTINUE
    L3=J2
    S4=0.
    DO 171 K4=1,H4
    L2=1+IABS(K4-K2)
    DO 170 J4=1,W4
    L1=W4+1-J4
    S=B4(J4,K4)*FP(L1,L2,L3)*G4(J4,K4)
    S4=S4+S
170 CONTINUE
171 CONTINUE
    L3=H2+1-K2
    S5=0.
    DO 181 J5=1,W5
    L2=1+IABS(J5-J2)
    DO 180 K5=1,H5
    L1=H5+1-K5
    S=B5(J5,K5)*FP(L1,L2,L3)*G5(J5,K5)
    S5=S5+S
180 CONTINUE
181 CONTINUE
    L3=K2
    S6=0.
    DO 191 J6=1,W6
    L2=1+IABS(J6-J2)
```

```
      DO 190 K6=1,H6
      L1=H6+1-K6
      S=B6(J6,K6)*FP(L1,L2,L3)*G6(J6,K6)
      S6=S6+S
  190 CONTINUE
  191 CONTINUE
      C2(J2,K2)=(S1+S3+S4+S5+S6)
  200 CONTINUE
  201 CONTINUE
      DO 301 K3=1,H3
      DO 300 J3=1,W3
      L3=J3
      S1=0.
      DO 251 K1=1,H1
      L2=1+IABS(K3-K1)
      DO 250 J1=1,W1
      L1=W1+1-J1
      S=FP(L1,L2,L3)*(B1(J1,K1)*G1(J1,K1)+S0(J1,K1))
      S1=S1+S
  250 CONTINUE
  251 CONTINUE
      L3=W3+1-J3
      S2=0.
      DO 261 K2=1,H2
      L2=1+IABS(K3-K2)
      DO 260 J2=1,W2
      L1=W2+1-J2
      S=B2(J2,K2)*FP(L1,L2,L3)*G2(J2,K2)
      S2=S2+S
  260 CONTINUE
  261 CONTINUE
      L3=W1
      S4=0.
      DO 271 K4=1,H4
      L2=1+IABS(K4-K3)
      DO 270 J4=1,W4
```

```
      L1=1+IABS(J4-J3)
      S=B4(J4,K4)*FL(L1,L2,L3)*G4(J4,K4)
      S4=S4+S
  270 CONTINUE
  271 CONTINUE
      L3=H3+1-K3
      S5=0.
      DO 281 K5=1,H5
      L2=1+IABS(K5-J3)
      DO 280 J5=1,W5
      L1=W5+1-J5
      S=B5(J5,K5)*FP(L1,L2,L3)*G5(J5,K5)
      S5=S5+S
  280 CONTINUE
  281 CONTINUE
      L3=K3
      S6=0.
      DO 291 K6=1,H6
      L2=1+IABS(K6-J3)
      DO 290 J6=1,W6
      L1=W6+1-J6
      S=B6(J6,K6)*FP(L1,L2,L3)*G6(J6,K6)
      S6=S6+S
  290 CONTINUE
  291 CONTINUE
      C3(J3,K3)=(S1+S2+S4+S5+S6)
  300 CONTINUE
  301 CONTINUE
      DO 401 K4=1,H4
      DO 400 J4=1,W4
      L3=J4
      S1=0.
      DO 351 K1=1,H1
      L2=1+IABS(K4-K1)
      DO 350 J1=1,W1
      L1=J1
```

```
      S=FP(L1,L2,L3)*(B1(J1,K1)*G1(J1,K1)+S0(J1,K1))
      S1=S1+S
  350 CONTINUE
  351 CONTINUE
      L3=W4+1-J4
      S2=0.
      DO 361 K2=1,H2
      L2=1+IABS(K4-K2)
      DO 360 J2=1,W2
      L1=J2
      S=B2(J2,K2)*FP(L1,L2,L3)*G2(J2,K2)
      S2=S2+S
  360 CONTINUE
  361 CONTINUE
      L3=W1
      S3=0.
      DO 371 K3=1,H3
      L2=1+IABS(K4-K3)
      DO 370 J3=1,W3
      L1=1+IABS(J4-J3)
      S=B3(J3,K3)*FL(L1,L2,L3)*G3(J3,K3)
      S3=S3+S
  370 CONTINUE
  371 CONTINUE
      L3=H4+1-K4
      S5=0.
      DO 381 K5=1,H5
      L2=1+IABS(K5-J4)
      DO 380 J5=1,W5
      L1=J5
      S=B5(J5,K5)*FP(L1,L2,L3)*G5(J5,K5)
      S5=S5+S
  380 CONTINUE
  381 CONTINUE
      L3=K4
      S6=0.
```

```
      DO 391 K6=1,H6
      L2=1+IABS(K6-J4)
      DO 390 J6=1,W6
      L1=J6
      S=B6(J6,K6)*FP(L1,L2,L3)*G6(J6,K6)
      S6=S6+S
  390 CONTINUE
  391 CONTINUE
      C4(J4,K4)=(S1+S2+S3+S5+S6)
  400 CONTINUE
  401 CONTINUE
      DO 501 K5=1,H5
      DO 500 J5=1,W5
      L3=K5
      S1=0.
      DO 451 J1=1,W1
      L2=1+IABS(J5-J1)
      DO 450 K1=1,H1
      L1=H1+1-K1
      S=FP(L1,L2,L3)*(B1(J1,K1)*G1(J1,K1)+S0(J1,K1))
      S1=S1+S
  450 CONTINUE
  451 CONTINUE
      L3=H5+1-K5
      S2=0.
      DO 461 J2=1,W2
      L2=1+IABS(J5-J2)
      DO 460 K2=1,H2
      L1=H2+1-K2
      S=B2(J2,K2)*FP(L1,L2,L3)*G2(J2,K2)
      S2=S2+S
  460 CONTINUE
  461 CONTINUE
      L3=W5+1-J5
      S3=0.
      DO 471 J3=1,W3
```

```
      L2=1+IABS(K5-J3)
      DO 470 K3=1,H3
      L1=H3+1-K3
      S=B3(J3,K3)*FP(L1,L2,L3)*G3(J3,K3)
      S3=S3+S
  470 CONTINUE
  471 CONTINUE
      L3=J5
      S4=0.
      DO 481 J4=1,W4
      L2=1+IABS(K5-J4)
      DO 480 K4=1,H4
      L1=H4+1-K4
      S=B4(J4,K4)*FP(L1,L2,L3)*G4(J4,K4)
      S4=S4+S
  480 CONTINUE
  481 CONTINUE
      L3=H1
      S6=0.
      DO 491 K6=1,H6
      L2=1+IABS(K6-K5)
      DO 490 J6=1,W6
      L1=1+IABS(J6-J5)
      S=B6(J6,K6)*FL(L1,L2,L3)*G6(J6,K6)
      S6=S6+S
  490 CONTINUE
  491 CONTINUE
      C5(J5,K5)=(S1+S2+S3+S4+S6)
  500 CONTINUE
  501 CONTINUE
      DO 601 K6=1,H6
      DO 600 J6=1,W6
      L3=K6
      S1=0.
      DO 551 J1=1,W1
      L2=1+IABS(J6-J1)
```

```
      DO 550 K1=1,H1
      L1=K1
      S=FP(L1,L2,L3)*(B1(J1,K1)*G1(J1,K1)+S0(J1,K1))
      S1=S1+S
  550 CONTINUE
  551 CONTINUE
      L3=H6+1-K6
      S2=0.
      DO 561 J2=1,W2
      L2=1+IABS(J6-J2)
      DO 560 K2=1,H2
      L1=K2
      S=B2(J2,K2)*FP(L1,L2,L3)*G2(J2,K2)
      S2=S2+S
  560 CONTINUE
  561 CONTINUE
      L3=W6+1-J6
      S3=0.
      DO 571 J3=1,W3
      L2=1+IABS(K6-J3)
      DO 570 K3=1,H3
      L1=K3
      S=B3(J3,K3)*FP(L1,L2,L3)*G3(J3,K3)
      S3=S3+S
  570 CONTINUE
  571 CONTINUE
      L3=J6
      S4=0.
      DO 581 J4=1,W4
      L2=1+IABS(K6-J4)
      DO 580 K4=1,H4
      L1=K4
      S=B4(J4,K4)*FP(L1,L2,L3)*G4(J4,K4)
      S4=S4+S
  580 CONTINUE
  581 CONTINUE
```

```
      L3=H1
      S5=0.
      DO 591 K5=1,H5
      L2=1+IABS(K6-K5)
      DO 590 J5=1,W5
      L1=1+IABS(J6-J5)
      S=B5(J5,K5)*FL(L1,L2,L3)*G5(J5,K5)
      S5=S5+S
  590 CONTINUE
  591 CONTINUE
      C6(J6,K6)=(S1+S2+S3+S4+S5)
  600 CONTINUE
  601 CONTINUE
      DO 641 K1=1,H1
      DO 640 J1=1,W1
      NC1(J1,K1)=C1(J1,K1)*(1.-B1(J1,K1))
  640 CONTINUE
  641 CONTINUE
      DO 651 K2=1,H2
      DO 650 J2=1,W2
      NC2(J2,K2)=C2(J2,K2)*(1.-B2(J2,K2))
  650 CONTINUE
  651 CONTINUE
      DO 661 K3=1,H3
      DO 660 J3=1,W3
      NC3(J3,K3)=C3(J3,K3)*(1.-B3(J3,K3))
  660 CONTINUE
  661 CONTINUE
      DO 671 K4=1,H4
      DO 670 J4=1,W4
      NC4(J4,K4)=C4(J4,K4)*(1.-B4(J4,K4))
  670 CONTINUE
  671 CONTINUE
      DO 681 K5=1,H5
      DO 680 J5=1,W5
      NC5(J5,K5)=C5(J5,K5)*(1.-B5(J5,K5))
```

```
680 CONTINUE
681 CONTINUE
    DO 691 K6=1,H6
    DO 690 J6=1,W6
    NC6(J6,K6)=C6(J6,K6)*(1.-B6(J6,K6))
690 CONTINUE
691 CONTINUE
    TSO=0.
    TNC1=0.
    DO 701 K1=1,H1
    DO 700 J1=1,W1
    TSO=TSO+SO(J1,K1)
    TNC1=TNC1+NC1(J1,K1)
700 CONTINUE
701 CONTINUE
    TNC2=0.
    DO 711 K2=1,H2
    DO 710 J2=1,W2
    TNC2=TNC2+NC2(J2,K2)
710 CONTINUE
711 CONTINUE
    TNC3=0.
    DO 721 K3=1,H3
    DO 720 J3=1,W3
    TNC3=TNC3+NC3(J3,K3)
720 CONTINUE
721 CONTINUE
    TNC4=0.
    DO 731 K4=1,H4
    DO 730 J4=1,W4
    TNC4=TNC4+NC4(J4,K4)
730 CONTINUE
731 CONTINUE
    TNC5=0.
    DO 741 K5=1,H5
    DO 740 J5=1,W5
```

```
      TNC5=TNC5+NC5(J5,K5)
  740 CONTINUE
  741 CONTINUE
      TNC6=0.
      DO 751 K6=1,H6
      DO 750 J6=1,W6
      TNC6=TNC6+NC6(J6,K6)
  750 CONTINUE
  751 CONTINUE
      KK=TSO/(TNC1+TNC2+TNC3+TNC4+TNC5+TNC6)
      DO 811 K1=1,H1
      DO 810 J1=1,W1
      C1(J1,K1)=KK*C1(J1,K1)
  810 CONTINUE
  811 CONTINUE
      DO 821 K2=1,H2
      DO 820 J2=1,W2
      C2(J2,K2)=KK*C2(J2,K2)
  820 CONTINUE
  821 CONTINUE
      DO 831 K3=1,H3
      DO 830 J3=1,W3
      C3(J3,K3)=KK*C3(J3,K3)
  830 CONTINUE
  831 CONTINUE
      DO 841 K4=1,H4
      DO 840 J4=1,W4
      C4(J4,K4)=KK*C4(J4,K4)
  840 CONTINUE
  841 CONTINUE
      DO 851 K5=1,H5
      DO 850 J5=1,W5
      C5(J5,K5)=KK*C5(J5,K5)
  850 CONTINUE
  851 CONTINUE
      DO 861 K6=1,H6
```

```
      DO 860 J6=1,W6
      C6(J6,K6)=KK*C6(J6,K6)
  860 CONTINUE
  861 CONTINUE
      Z=0.
      DO 911 K1=1,H1
      DO 910 J1=1,W1
      X1=ABS(C1(J1,K1)-G1(J1,K1))
      IF(X1 .GE. Z) GO TO 909
      Z=Z
      GO TO 910
  909 Z=X1
  910 CONTINUE
  911 CONTINUE
      DO 921 K2=1,H2
      DO 920 J2=1,W2
      X2=ABS(C2(J2,K2)-G2(J2,K2))
      IF(X2 .GE. Z) GO TO 919
      Z=Z
      GO TO 920
  919 Z=X2
  920 CONTINUE
  921 CONTINUE
      DO 931 K3=1,H3
      DO 930 J3=1,W3
      X3=ABS(C3(J3,K3)-G3(J3,K3))
      IF(X3 .GE. Z) GO TO 929
      Z=Z
      GO TO 930
  929 Z=X3
  930 CONTINUE
  931 CONTINUE
      DO 941 K4=1,H4
      DO 940 J4=1,W4
      X4=ABS(C4(J4,K4)-G4(J4,K4))
      IF(X4 .GE. Z) GO TO 939
```

```
      Z=Z
      GO TO 940
  939 Z=X4
  940 CONTINUE
  941 CONTINUE
      DO 951 K5=1,H5
      DO 950 J5=1,W5
      X5=ABS(C5(J5,K5)-G5(J5,K5))
      IF(X5 .GE. Z) GO TO 949
      Z=Z
      GO TO 950
  949 Z=X5
  950 CONTINUE
  951 CONTINUE
      DO 961 K6=1,H6
      DO 960 J6=1,W6
      X6=ABS(C6(J6,K6)-G6(J6,K6))
      IF(X6 .GE. Z) GO TO 959
      Z=Z
      GO TO 960
  959 Z=X6
  960 CONTINUE
  961 CONTINUE
      IF(Z .LE. 0.0001) GO TO 1100
      DO 1011 K1=1,H1
      DO 1010 J1=1,W1
      G1(J1,K1)=C1(J1,K1)
 1010 CONTINUE
 1011 CONTINUE
      DO 1021 K2=1,H2
      DO 1020 J2=1,W2
      G2(J2,K2)=C2(J2,K2)
 1020 CONTINUE
 1021 CONTINUE
      DO 1031 K3=1,H3
      DO 1030 J3=1,W3
```

```
      G3(J3,K3)=C3(J3,K3)
 1030 CONTINUE
 1031 CONTINUE
      DO 1041 K4=1,H4
      DO 1040 J4=1,W4
      G4(J4,K4)=C4(J4,K4)
 1040 CONTINUE
 1041 CONTINUE
      DO 1051 K5=1,H5
      DO 1050 J5=1,W5
      G5(J5,K5)=C5(J5,K5)
 1050 CONTINUE
 1051 CONTINUE
      DO 1061 K6=1,H6
      DO 1060 J6=1,W6
      G6(J6,K6)=C6(J6,K6)
 1060 CONTINUE
 1061 CONTINUE
      GO TO 40
 1100 WRITE(6,1)
      DO 1110 K1=1,H1
      WRITE(6,8) (C1(J1,K1), J1=1,W1)
 1110 CONTINUE
      WRITE(6,2)
      DO 1120 K2=1,H2
      WRITE(6,8) (C2(J2,K2), J2=1,W2)
 1120 CONTINUE
      WRITE(6,3)
      DO 1130 K3=1,H3
      WRITE(6,8) (C3(J3,K3), J3=1,W3)
 1130 CONTINUE
      WRITE(6,4)
      DO 1140 K4=1,H4
      WRITE(6,8) (C4(J4,K4), J4=1,W4)
 1140 CONTINUE
      WRITE(6,5)
```

```
      DO 1150 K5=1,H5
      WRITE(6,8) (C5(J5,K5), J5=1,W5)
1150 CONTINUE
      WRITE(6,6)
      DO 1160 K6=1,H6
      WRITE(6,8) (C6(J6,K6), J6=1,W6)
1160 CONTINUE
      WRITE(6,10)
      DO 1210 K1=1,H1
      WRITE(6,8) (NC1(J1,K1), J1=1,W1)
1210 CONTINUE
      WRITE(6,11)
      DO 1220 K2=1,H2
      WRITE(6,8) (NC2(J2,K2), J2=1,W2)
1220 CONTINUE
      WRITE(6,12)
      DO 1230 K3=1,H3
      WRITE(6,8) (NC3(J3,K3), J3=1,W3)
1230 CONTINUE
      WRITE(6,13)
      DO 1240 K4=1,H4
      WRITE(6,8) (NC4(J4,K4), J4=1,W4)
1240 CONTINUE
      WRITE(6,14)
      DO 1250 K5=1,H5
      WRITE(6,8) (NC5(J5,K5), J5=1,W5)
1250 CONTINUE
      WRITE(6,15)
      DO 1260 K6=1,H6
      WRITE(6,8) (NC6(J6,K6), J6=1,W6)
1260 CONTINUE
      WRITE(6,1400)
      DO 1311 K1=1,H1
      DO 1310 J1=1,W1
      PH1(J1,K1)=C1(J1,K1)*(1.+B1(J1,K1))
1310 CONTINUE
```

```
      WRITE(6,8) (PH1(J1,K1), J1=1,W1)
 1311 CONTINUE
      WRITE(6,1401)
      DO 1321 K2=1,H2
      DO 1320 J2=1,W2
      PH2(J2,K2)=C2(J2,K2)*(1.+B2(J2,K2))
 1320 CONTINUE
      WRITE(6,8) (PH2(J2,K2), J2=1,W2)
 1321 CONTINUE
      WRITE(6,1402)
      DO 1331 K3=1,H3
      DO 1330 J3=1,W3
      PH3(J3,K3)=C3(J3,K3)*(1.+B3(J3,K3))
 1330 CONTINUE
      WRITE(6,8) (PH3(J3,K3), J3=1,W3)
 1331 CONTINUE
      WRITE(6,1403)
      DO 1341 K4=1,H4
      DO 1340 J4=1,W4
      PH4(J4,K4)=C4(J4,K4)*(1.+B4(J4,K4))
 1340 CONTINUE
      WRITE(6,8) (PH4(J4,K4), J4=1,W4)
 1341 CONTINUE
      WRITE(6,1404)
      DO 1351 K5=1,H5
      DO 1350 J5=1,W5
      PH5(J5,K5)=C5(J5,K5)*(1.+B5(J5,K5))
 1350 CONTINUE
      WRITE(6,8) (PH5(J5,K5), J5=1,W5)
 1351 CONTINUE
      WRITE(6,1405)
      DO 1361 K6=1,H6
      DO 1360 J6=1,W6
      PH6(J6,K6)=C6(J6,K6)*(1.+B6(J6,K6))
 1360 CONTINUE
      WRITE(6,8) (PH6(J6,K6), J6=1,W6)
```

```
1361 CONTINUE
1400 FORMAT(27H1                    FLUX ON FACE ONE)
1401 FORMAT(27H1                    FLUX ON FACE TWO)
1402 FORMAT(29H1                    FLUX ON FACE THREE)
1403 FORMAT(28H1                    FLUX ON FACE FOUR)
1404 FORMAT(28H1                    FLUX ON FACE FIVE)
1405 FORMAT(27H1                    FLUX ON FACE SIX)
     END
```

```
C      TARGET
C      MAIN PROGRAM
C      FLUXES IN CONVERGING HOLLOW CAVITY
       COMMON GM1(10,10,10),GM2(10,10,10),GM3(10,10,10),GM4(10,10,10),GM5
      1(10,10,10),GM6(10,10,10),BM1(10,10,10),BM2(10,10,10),BM3(10,10,10)
      1,BM4(10,10,10),BM5(10,10,10),BM6(10,10,10),SOM(10,10,10),PHM1(10,
      110,10),PHM2(10,10,10),PHM3(10,10,10),PHM4(10,10,10),PHM5(10,10,10)
      1,PHM6(10,10,10),CM1(10,10,10),CM2(10,10,10),CM3(10,10,10),CM4(10,
      110,10),CM5(10,10,10),CM6(10,10,10),NCM2(10,10,10)
       COMMON G1(10,10),G2(10,10),G3(10,10),G4(10,10),G5(10,10),G6(10,10)
      1,B1(10,10),B2(10,10),B3(10,10),B4(10,10),B5(10,10),B6(10,10),C1(10
      1,10),C2(10,10),C3(10,10),C4(10,10),C5(10,10),C6(10,10),NC1(10,10),
      1NC2(10,10),NC3(10,10),NC4(10,10),NC5(10,10),NC6(10,10),SO(10,10),
      1PH1(10,10),PH2(10,10),PH3(10,10),PH4(10,10),PH5(10,10),PH6(10,10)
       COMMON TSOM(10),TCM21(10),TCM1(10),TCM2(10),TCM3(10),TCM4(10),
      1TCM5(10),TCM6(10)
       COMMON TNC1,TNC2,TNC3,TNC4,TNC5,TNC6
       COMMON FL(10,10,10),FP(10,10,10),KK,Z,H1,H2,H3,H4,H5,H6,W1,W2,W3,
      1W4,W5,W6
       COMMON K1MAX(10),J1MAX(10),K2MAX(10),J2MAX(10),K3MAX(10),J3MAX(10)
      1,K4MAX(10),J4MAX(10),K5MAX(10),J5MAX(10),K6MAX(10),J6MAX(10)
       INTEGER HK2,HJ2
       INTEGER H1,W1,H2,W2,H3,W3,H4,W4,H5,W5,H6,W6
       REAL KK
       REAL NC1,NC2,NC3,NC4,NC5,NC6,NCM2
       READ(5,10) NMAX
   10  FORMAT(1I5)
       DO 80 N=1,NMAX
       READ(5,11) (K1MAX(N),J1MAX(N),K2MAX(N),J2MAX(N),K3MAX(N),J3MAX(N),
      1K4MAX(N),J4MAX(N),K5MAX(N),J5MAX(N),K6MAX(N),J6MAX(N))
   11  FORMAT(12I5)
       WRITE(6,11) (K1MAX(N),J1MAX(N),K2MAX(N),J2MAX(N),K3MAX(N),J3MAX(N)
      1,K4MAX(N),J4MAX(N),K5MAX(N),J5MAX(N),K6MAX(N),J6MAX(N))
       H1=K1MAX(N)
       W1=J1MAX(N)
       H2=K2MAX(N)
```

```
      W2=J2MAX(N)
      H3=K3MAX(N)
      W3=J3MAX(N)
      H4=K4MAX(N)
      W4=J4MAX(N)
      H5=K5MAX(N)
      W5=J5MAX(N)
      H6=K6MAX(N)
      W6=J6MAX(N)
      DO 12 K1=1,H1
      READ(5,13) (GM1(J1,K1,N),BM1(J1,K1,N),SOM(J1,K1,N), J1=1,W1)
   13 FORMAT(9F8.5)
      WRITE(6,14) (GM1(J1,K1,N),BM1(J1,K1,N),SOM(J1,K1,N), J1=1,W1)
   14 FORMAT(1H0,15F8.5)
   12 CONTINUE
      DO 15 K2=1,H2
      READ(5,13) (GM2(J2,K2,N),BM2(J2,K2,N), J2=1,W2)
      WRITE(6,14) (GM2(J2,K2,N),BM2(J2,K2,N), J2=1,W2)
   15 CONTINUE
      DO 16 K3=1,H3
      READ(5,13) (GM3(J3,K3,N),BM3(J3,K3,N), J3=1,W3)
      WRITE(6,14) (GM3(J3,K3,N),BM3(J3,K3,N), J3=1,W3)
   16 CONTINUE
      DO 17 K4=1,H4
      READ(5,13) (GM4(J4,K4,N),BM4(J4,K4,N), J4=1,W4)
      WRITE(6,14) (GM4(J4,K4,N),BM4(J4,K4,N), J4=1,W4)
   17 CONTINUE
      DO 18 K5=1,H5
      READ(5,13) (GM5(J5,K5,N),BM5(J5,K5,N), J5=1,W5)
      WRITE(6,14) (GM5(J5,K5,N),BM5(J5,K5,N), J5=1,W5)
   18 CONTINUE
      DO 19 K6=1,H6
      READ(5,13) (GM6(J6,K6,N),BM6(J6,K6,N), J6=1,W6)
      WRITE(6,14) (GM6(J6,K6,N),BM6(J6,K6,N), J6=1,W6)
   19 CONTINUE
   80 CONTINUE
```

```
      READ(5,10) MMAX
      WRITE(6,81) MMAX
   81 FORMAT('0',1I5)
      DO 85 M=1,MMAX
      READ(5,10) L3
      WRITE(6,81) L3
      DO 83 L2=1,10
      READ(5,13) (FL(L1,L2,L3), L1=1,10)
      WRITE(6,14) (FL(L1,L2,L3), L1=1,10)
   83 CONTINUE
   85 CONTINUE
      DO 89 L3=1,10
      DO 89 L2=1,10
      READ(5,13) (FP(L1,L2,L3), L1=1,10)
      WRITE(6,14) (FP(L1,L2,L3), L1=1,10)
   89 CONTINUE
   90 DO 500 N=1,NMAX
      H1=K1MAX(N)
      W1=J1MAX(N)
      H2=K2MAX(N)
      W2=J2MAX(N)
      H3=K3MAX(N)
      W3=J3MAX(N)
      H4=K4MAX(N)
      W4=J4MAX(N)
      H5=K5MAX(N)
      W5=J5MAX(N)
      H6=K6MAX(N)
      W6=J6MAX(N)
      TSOM(N)=0.
      DO 100 K1=1,H1
      DO 100 J1=1,W1
      G1(J1,K1)=GM1(J1,K1,N)
      B1(J1,K1)=BM1(J1,K1,N)
      SO(J1,K1)=SOM(J1,K1,N)
      TSOM(N)=TSOM(N)+SO(J1,K1)
```

```
100 CONTINUE
    DO 110 K2=1,H2
    DO 110 J2=1,W2
    G2(J2,K2)=GM2(J2,K2,N)
    B2(J2,K2)=BM2(J2,K2,N)
110 CONTINUE
    DO 120 K3=1,H3
    DO 120 J3=1,W3
    G3(J3,K3)=GM3(J3,K3,N)
    B3(J3,K3)=BM3(J3,K3,N)
120 CONTINUE
    DO 130 K4=1,H4
    DO 130 J4=1,W4
    G4(J4,K4)=GM4(J4,K4,N)
    B4(J4,K4)=BM4(J4,K4,N)
130 CONTINUE
    DO 140 K5=1,H5
    DO 140 J5=1,W5
    G5(J5,K5)=GM5(J5,K5,N)
    B5(J5,K5)=BM5(J5,K5,N)
140 CONTINUE
    DO 150 K6=1,H6
    DO 150 J6=1,W6
    G6(J6,K6)=GM6(J6,K6,N)
    B6(J6,K6)=BM6(J6,K6,N)
150 CONTINUE
    CALL HOLCAV
    TCM1(N)=TNC1
    DO 160 K1=1,H1
    DO 160 J1=1,W1
    CM1(J1,K1,N)=C1(J1,K1)
160 CONTINUE
    TCM2(N)=TNC2
    DO 170 K2=1,H2
    DO 170 J2=1,W2
    CM2(J2,K2,N)=C2(J2,K2)
```

```
      NCM2(J2,K2,N)=NC2(J2,K2)
  170 CONTINUE
      TCM3(N)=TNC3
      DO 180 K3=1,H3
      DO 180 J3=1,W3
      CM3(J3,K3,N)=C3(J3,K3)
  180 CONTINUE
      TCM4(N)=TNC4
      DO 190 K4=1,H4
      DO 190 J4=1,W4
      CM4(J4,K4,N)=C4(J4,K4)
  190 CONTINUE
      TCM5(N)=TNC5
      DO 200 K5=1,H5
      DO 200 J5=1,W5
      CM5(J5,K5,N)=C5(J5,K5)
  200 CONTINUE
      TCM6(N)=TNC6
      DO 210 K6=1,H6
      DO 210 J6=1,W6
      CM6(J6,K6,N)=C6(J6,K6)
  210 CONTINUE
      IF(N .EQ. NMAX) GO TO 500
      IF(N .EQ. 1) GO TO 215
      HK2=K1MAX(N+1)
      HJ2=J1MAX(N+1)
      LK2=((H2-HK2)/2)+1
      LJ2=((W2-HJ2)/2)+1
      MK2=LK2+HK2-1
      MJ2=LJ2+HJ2-1
      GO TO 216
  215 LK2=3
      LJ2=4
      MK2=6
      MJ2=7
  216 TCM21(N)=0.0
```

```
      DO 220 K2=LK2,MK2
      DO 220 J2=LJ2,MJ2
      TCM21(N)=TCM21(N)+NCM2(J2,K2,N)
      K1=K2+1-LK2
      J1=J2+1-LJ2
      SOM(J1,K1,N+1)=CM2(J2,K2,N)
  220 CONTINUE
  500 CONTINUE
      TTCM=TCM1(1)
      DO 510 N=1,NMAX
      TTCM=TTCM+TCM2(N)+TCM3(N)+TCM4(N)+TCM5(N)+TCM6(N)
  510 CONTINUE
      NN=NMAX-1
      DO 515 N=1,NN
      TTCM=TTCM-TCM21(N)
  515 CONTINUE
  521 KK=ABS(TSOM(1)/TTCM)
      Z=0.0
      DO 700 N=1,NMAX
  522 FORMAT('0',1F10.5)
      H1=K1MAX(N)
      W1=J1MAX(N)
      H2=K2MAX(N)
      W2=J2MAX(N)
      H3=K3MAX(N)
      W3=J3MAX(N)
      H4=K4MAX(N)
      W4=J4MAX(N)
      H5=K5MAX(N)
      W5=J5MAX(N)
      H6=K6MAX(N)
      W6=J6MAX(N)
      DO 530 K1=1,H1
      DO 530 J1=1,W1
      C1(J1,K1)=CM1(J1,K1,N)
      G1(J1,K1)=GM1(J1,K1,N)
```

```
      B1(J1,K1)=BM1(J1,K1,N)
  530 CONTINUE
      DO 540 K2=1,H2
      DO 540 J2=1,W2
      C2(J2,K2)= CM2(J2,K2,N)
      G2(J2,K2)= GM2(J2,K2,N)
      B2(J2,K2)=BM2(J2,K2,N)
  540 CONTINUE
      DO 550 K3=1,H3
      DO 550 J3=1,W3
      C3(J3,K3)= CM3(J3,K3,N)
      G3(J3,K3)=GM3(J3,K3,N)
      B3(J3,K3)=BM3(J3,K3,N)
  550 CONTINUE
      DO 560 K4=1,H4
      DO 560 J4=1,W4
      C4(J4,K4)=CM4(J4,K4,N)
      G4(J4,K4)=GM4(J4,K4,N)
      B4(J4,K4)=BM4(J4,K4,N)
  560 CONTINUE
      DO 570 K5=1,H5
      DO 570 J5=1,W5
      C5(J5,K5)=CM5(J5,K5,N)
      G5(J5,K5)=GM5(J5,K5,N)
      B5(J5,K5)=BM5(J5,K5,N)
  570 CONTINUE
      DO 580 K6=1,H6
      DO 580 J6=1,W6
      C6(J6,K6)=CM6(J6,K6,N)
      G6(J6,K6)=GM6(J6,K6,N)
      B6(J6,K6)=BM6(J6,K6,N)
  580 CONTINUE
      CALL NORM
      Z=Z
  582 FORMAT('0',1F10.5)
      DO 590 K1=1,H1
```

```
      DO 590 J1=1,W1
      GM1(J1,K1,N)=C1(J1,K1)
      PHM1(J1,K1,N)=PH1(J1,K1)
  590 CONTINUE
      DO 600 K2=1,H2
      DO 600 J2=1,W2
      GM2(J2,K2,N)=C2(J2,K2)
      PHM2(J2,K2,N)=PH2(J2,K2)
  600 CONTINUE
      DO 610 K3=1,H3
      DO 610 J3=1,W3
      GM3(J3,K3,N)=C3(J3,K3)
      PHM3(J3,K3,N)=PH3(J3,K3)
  610 CONTINUE
      DO 620 K4=1,H4
      DO 620 J4=1,W4
      GM4(J4,K4,N)=C4(J4,K4)
      PHM4(J4,K4,N)=PH4(J4,K4)
  620 CONTINUE
      DO 630 K5=1,H5
      DO 630 J5=1,W5
      GM5(J5,K5,N)=C5(J5,K5)
      PHM5(J5,K5,N)=PH5(J5,K5)
  630 CONTINUE
      DO 640 K6=1,H6
      DO 640 J6=1,W6
      GM6(J6,K6,N)=C6(J6,K6)
      PHM6(J6,K6,N)=PH6(J6,K6)
  640 CONTINUE
  700 CONTINUE
      IF(Z .LE. 0.0001) GO TO 1000
      NN=NMAX-1
      DO 720 N=1,NN
      IF(N .EQ. 1) GO TO 705
      H2=K2MAX(N)
      W2=J2MAX(N)
```

```
      HK2=K1MAX(N+1)
      HJ2=J1MAX(N+1)
      LK2=((H2-HK2)/2)+1
      LJ2=((W2-HJ2)/2)+1
      MK2=LK2+HK2-1
      MJ2=LJ2+HJ2-1
      GO TO 706
  705 LK2=3
      LJ2=4
      MK2=6
      MJ2=7
  706 DO 710 K2=LK2,MK2
      DO 710 J2=LJ2,MJ2
      K1=K2+1-LK2
      J1=J2+1-LJ2
      BM2(J2,K2,N)=GM1(J1,K1,N+1)/GM2(J2,K2,N)
  710 CONTINUE
  720 CONTINUE
      GO TO 90
 1000 DO 1500 N=1,NMAX
      H1=K1MAX(N)
      W1=J1MAX(N)
      H2=K2MAX(N)
      W2=J2MAX(N)
      H3=K3MAX(N)
      W3=J3MAX(N)
      H4=K4MAX(N)
      W4=J4MAX(N)
      H5=K5MAX(N)
      W5=J5MAX(N)
      H6=K6MAX(N)
      W6=J6MAX(N)
      WRITE(6,1001) N
 1001 FORMAT('1','FLUX ON FACE ONE,CACITY  ',I2)
      DO 1010 K1=1,H1
      WRITE(6,1011) (PHM1(J1,K1,N), J1=1,W1)
```

```
1011 FORMAT('0',10F12.5)
1010 CONTINUE
     WRITE(6,1012) N
1012 FORMAT('1','FLUX ON FACE TWO,CAVITY  ',I2)
     DO 1020 K2=1,H2
     WRITE(6,1011) (PHM2(J2,K2,N), J2=1,W2)
1020 CONTINUE
     WRITE(6,1021) N
1021 FORMAT('1','FLUX ON FACE THREE,CAVITY  ',I2)
     DO 1030 K3=1,H3
     WRITE(6,1011) (PHM3(J3,K3,N), J3=1,W3)
1030 CONTINUE
     WRITE(6,1031) N
1031 FORMAT('1','FLUX ON FACE FOUR,CAVITY  ',I2)
     DO 1040 K4=1,H4
     WRITE(6,1011) (PHM4(J4,K4,N), J4=1,W4)
1040 CONTINUE
     WRITE(6,1041) N
1041 FORMAT('1','FLUX ON FACE FIVE,CAVITY  ',I2)
     DO 1050 K5=1,H5
     WRITE(6,1011) (PHM5(J5,K5,N), J5=1,W5)
1050 CONTINUE
     WRITE(6,1051) N
1051 FORMAT('1','FLUX ON FACE SIX,CAVITY  ',I2)
     DO 1060 K6=1,H6
     WRITE(6,1011) (PHM6(J6,K6,N), J6=1,W6)
1060 CONTINUE
1500 CONTINUE
     END
```

```
      SUBROUTINE NORM
      COMMON GM1(10,10,10),GM2(10,10,10),GM3(10,10,10),GM4(10,10,10),GM5
     1(10,10,10),GM6(10,10,10),BM1(10,10,10),BM2(10,10,10),BM3(10,10,10)
     1,BM4(10,10,10),BM5(10,10,10),BM6(10,10,10),SOM(10,10,10),PHM1(10,
     110,10),PHM2(10,10,10),PHM3(10,10,10),PHM4(10,10,10),PHM5(10,10,10)
     1,PHM6(10,10,10),CM1(10,10,10),CM2(10,10,10),CM3(10,10,10),CM4(10,
     110,10),CM5(10,10,10),CM6(10,10,10),NCM2(10,10,10)
      COMMON G1(10,10),G2(10,10),G3(10,10),G4(10,10),G5(10,10),G6(10,10)
     1,B1(10,10),B2(10,10),B3(10,10),B4(10,10),B5(10,10),B6(10,10),C1(10
     1,10),C2(10,10),C3(10,10),C4(10,10),C5(10,10),C6(10,10),NC1(10,10),
     1NC2(10,10),NC3(10,10),NC4(10,10),NC5(10,10),NC6(10,10),SO(10,10),
     1PH1(10,10),PH2(10,10),PH3(10,10),PH4(10,10),PH5(10,10),PH6(10,10)
      COMMON TSOM(10),TCM21(10),TCM1(10),TCM2(10),TCM3(10),TCM4(10),
     1TCM5(10),TCM6(10)
      COMMON TNC1,TNC2,TNC3,TNC4,TNC5,TNC6
      COMMON FL(10,10,10),FP(10,10,10),KK,Z,H1,H2,H3,H4,H5,H6,W1,W2,W3,
     1W4,W5,W6
      COMMON K1MAX(10),J1MAX(10),K2MAX(10),J2MAX(10),K3MAX(10),J3MAX(10)
     1,K4MAX(10),J4MAX(10),K5MAX(10),J5MAX(10),K6MAX(10),J6MAX(10)
      INTEGER HK2,HJ2
      INTEGER H1,W1,H2,W2,H3,W3,H4,W4,H5,W5,H6,W6
      REAL KK
      REAL NC1,NC2,NC3,NC4,NC5,NC6,NCM2
      DO 811 K1=1,H1
      DO 810 J1=1,W1
      C1(J1,K1)=KK*C1(J1,K1)
      PH1(J1,K1)=C1(J1,K1)*(1.+B1(J1,K1))
      X1=ABS(C1(J1,K1)-G1(J1,K1))
      IF(X1 .GE. Z) GO TO 909
      Z=Z
      GO TO 810
  909 Z=X1
  810 CONTINUE
  811 CONTINUE
      DO 821 K2=1,H2
      DO 820 J2=1,W2
```

```
      C2(J2,K2)=KK*C2(J2,K2)
      PH2(J2,K2)=C2(J2,K2)*(1.+B2(J2,K2))
      X2=ABS(C2(J2,K2)-G2(J2,K2))
      IF(X2 .GE. Z) GO TO 919
      Z=Z
      GO TO 820
  919 Z=X2
  820 CONTINUE
  821 CONTINUE
      DO 831 K3=1,H3
      DO 830 J3=1,W3
      C3(J3,K3)=KK*C3(J3,K3)
      PH3(J3,K3)=C3(J3,K3)*(1.+B3(J3,K3))
      X3=ABS(C3(J3,K3)-G3(J3,K3))
      IF(X3 .GE. Z) GO TO 929
      Z=Z
      GO TO 830
  929 Z=X3
  830 CONTINUE
  831 CONTINUE
      DO 841 K4=1,H4
      DO 840 J4=1,W4
      C4(J4,K4)=KK*C4(J4,K4)
      PH4(J4,K4)=C4(J4,K4)*(1.+B4(J4,K4))
      X4=ABS(C4(J4,K4)-G4(J4,K4))
      IF(X4 .GE. Z) GO TO 939
      Z=Z
      GO TO 840
  939 Z=X4
  840 CONTINUE
  841 CONTINUE
      DO 851 K5=1,H5
      DO 850 J5=1,W5
      C5(J5,K5)=KK*C5(J5,K5)
      PH5(J5,K5)=C5(J5,K5)*(1.+B5(J5,K5))
      X5=ABS(C5(J5,K5)-G5(J5,K5))
```

```
      IF(X5 .GE. Z) GO TO 949
      Z=Z
      GO TO 850
  949 Z=X5
  850 CONTINUE
  851 CONTINUE
      DO 861 K6=1,H6
      DO 860 J6=1,W6
      C6(J6,K6)=KK*C6(J6,K6)
      PH6(J6,K6)=C6(J6,K6)*(1.+B6(J6,K6))
      X6=ABS(C6(J6,K6)-G6(J6,K6))
      IF(X6 .GE. Z) GO TO 959
      Z=Z
      GO TO 860
  959 Z=X6
  860 CONTINUE
  861 CONTINUE
      RETURN
      END
```

Appendix C

Lead Shutter Shielding Effects

Because of the benefits to be gained in neutron economy by eliminating the lead shutters (Section 3.2), it was decided to determine what effect the lead shutters had in shielding the D_2O lattice room and the hohlraum. The relative locations of the regions of interest are shown in figure C.1. As shown in the figure, there are three movable shields: the cadmium shutter (Cd), the lead shutter (Pb), and the steel doors (Fe). There are eight possible combinations for the shields which are given in Table C.1.

Table C.1

Shield Combinations

Cd Open	Cd Closed
Pb open, Fe open	Pb open, Fe open
Pb open, Fe closed	Pb open, Fe closed
Pb closed, Fe open	Pb closed, Fe open
Pb closed, Fe closed	Pb closed, Fe closed

Measurements were made of the gamma dose rate, the fast neutron flux, and the thermal neutron flux in the lattice room and hohlraum for all eight combinations. The measurements were also made as a function of the reactor power (both increasing and decreasing).

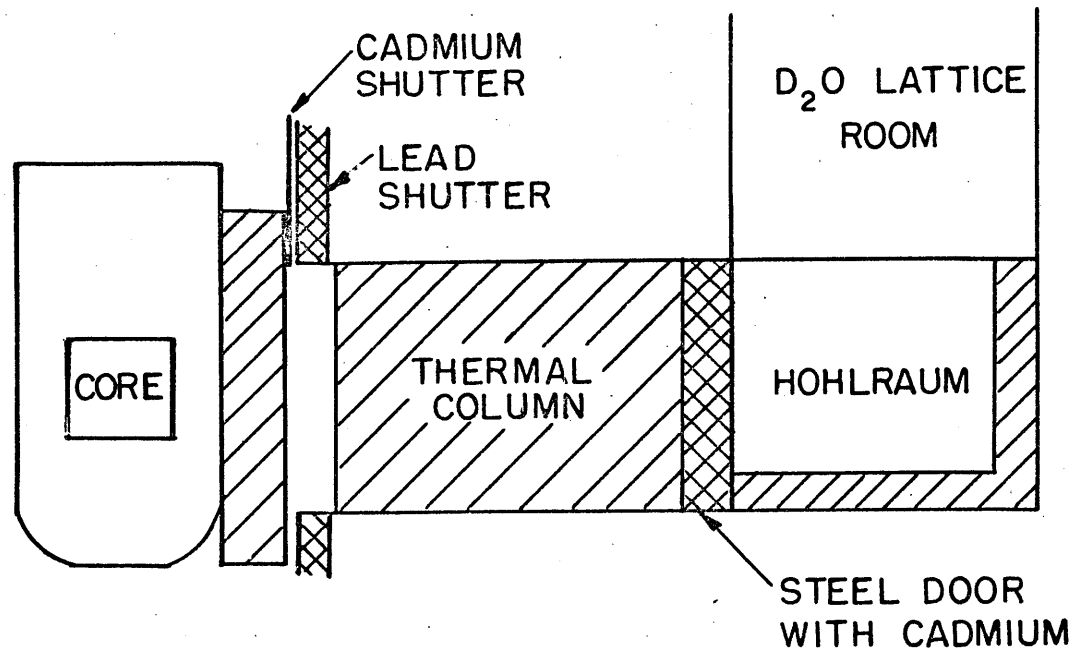

FIG. C.1 RELATIVE POSITIONS OF LATTICE ROOM, HOHLRAUM, AND SHUTTERS

In the lattice room the gammas were measured with a "Cutie Pie" detector, the fast neutrons with a BF_3 sheathed in polyethylene, and the slow neutrons with a bare BF_3. In the hohlraum the gammas were measured with a "Victoreen" detector, the fast neutrons with a polyethylene and cadmium sheathed BF_3 for fluxes $<5X10^3$ $n/cm^2 \cdot sec$ and a polyethylene and cadmium sheathed fission chamber for fluxes $>5X10^3$, and the slow neutrons with a bare BF_3 for fluxes $<10^7 n/cm^2 \cdot sec$ and a bare fission chamber for fluxes $>10^7$.

The results of the measurements are tabulated in Tables C.2 through C.5, and plotted in figures C.2 through C.7

With the lead shutter in the open position, the gamma dose rate in the lattice room appears to follow the slow neutron flux. This means that most of the gammas reaching the lattice room are capture gammas from the graphite in the thermal column and hohlraum. It therefore follows that the gamma dose rate in the lattice room can be controlled by controlling the thermal flux in the thermal column by means of the cadmium shutter. The steel door (with cadmium on it) also has a large effect on the lattice room gamma dose rate, indicating that a large part of these gammas originate in the graphite of the hohlraum.

A large fraction of the gammas reaching the hohlraum come directly from the reactor; therefore, the cadmium shutter alone is not very effective in reducing the hohlraum gamma dose rate. However, the steel doors are very effective in shielding the hohlraum from gamma rays. It appears that the only time the lead shutter may have to be closed is for work in the thermal

Table C.2

Dose Rates in Hohlraum

Cd Shutter Open — C = closed

Friday July 12, 1968 — O = opened

Power KW	Pb	Fe	Slow Neutrons CPM	Slow Neutrons $n/cm^2 \cdot sec$	Fast Neutrons CPM	Fast Neutrons $n/cm^2 \cdot sec$	Gammas, R/min Power Decreasing	Gammas, R/min Power Mon. July 15
	O	O	———	———	93,424(FC)	2.90×10^6	68	65.5
5000	O	C	———	———	4,807(FC)	1.44×10^5	0.1	0.1
	C	O	———	———	38,983(FC)	1.21×10^6	25	23
	C	C	———	———	1,019(FC)	3.16×10^4	0	~0.01
	O	O	———	———	17,312(FC)	5.37×10^5	32.5	12.7
1000	O	O	———	———	891(FC)	2.76×10^4	14	~0.01
	C	O	———	———	6,921(FC)	2.15×10^5	0.34-0.5	4.3
	C	C	188,224(BF_3)	6.77×10^6	193(FC)	5.48×10^3	0	0
	O	O	———	———	———	———	1.72	1.75
100	O	C	44(FC)	3.43×10^6	149,311(BF_3)	2.99×10^3	0.75	0
	C	O	800,000(FC)	5.60×10^{10}	715(FC)	2.22×10^4	0.27	0.4
	C	C	17,594(BF_3)	6.25×10^5	32,701(BF_3	6.54×10^2	0.25	0

Table C.2 (Continued)

Power KW	Pb	Fe	Slow Neutrons CPM	Slow Neutrons $n/cm^2 \cdot sec$	Fast Neutrons CPM	Fast Neutrons $n/cm^2 \cdot sec$	Gammas, R/min Power Decreasing	Gammas, R/min Power Mon. July 15
	O	O	137,868(FC)	$9.64X10^4$	232,200(BF_3)	$4.64X10^3$	_____	0.12
10	O	C	8,244(BF_3)	$2.92X10^5$	14,660(BF_3)	$2.93X10^2$	_____	0.0
	C	O	64,734(FC)	$4.88X10^4$	92,880(BF_3)	$1.86X10^3$	_____	0.04
	C	C	1,808(BF_3)	$6.41X10^4$	3,095(BF_3)	$6.19X10^1$	0.25	0

Table C.3

Dose Rates In Hohlraum

Cd Shutter Closed

Sat. July 13, 1968

C = closed

O = Opened

Power Kw	Pb	Fe	Slow Neutrons CPM	Slow Neutrons $n/cm^2 \cdot sec$	Fast Neutrons CPM	Fast Neutrons $n/cm^2 \cdot sec$	Gammas Tracer Lab mr	Gammas Victoreen R/Min
	O	O	275,000(FC)	$1.93X10^{10}$	6,740(FC)	$2.09X10^{5}$	400	7.6
1000	O	C	———	———	869(FC)	$2.69X10^{4}$	8	0
	C	O	———	———	1,844(FC)	$5.72X10^{4}$	400	0.3
	C	C	148,392(BF_3)	$5.35X10^{6}$	188(FC)	$5.83X10^{3}$	4	0
	O	O	32,784(FC)	$2.29X10^{9}$	657(FC)	$2.04X10^{4}$	50	0.79
100	O	C	74,746(BF_3)	$2.83X10^{6}$	132,234(BF_3)	$2.64X10^{3}$	2	0
	C	O	22,822(FC)	$1.60X10^{9}$	190(FC)	$5.89X10^{3}$	30	0
	C	C	16,630(BF_3)	$5.91X10^{5}$	29,276(BF_3)	$5.86X10^{2}$	2	0
	O	C	3,163(FC)	$2.22X10^{8}$	104,442(BF_3)	$2.09X10^{3}$	5	0.06
10	O	C	7,886(BF_3	$2.80X10^{5}$	13,868(BF_3)	$2.77\ X10^{2}$	—	—
	C	O	2,123(FC)	$1.44X10^{8}$	30,144(BF_3)	$6.03X10^{2}$	4	0
	C	C	1,653(BF_3)	$5.86X10^{4}$	3,871(BF_3)	$7.74X10^{1}$	1	0

Table C.4

Dose Rates in Lattice Room

Cd Shutter Open — C = Closed

Friday July 12, 1968 — O = Opened

Power KW	Pb	Fe	Slow Neutrons CPM	Slow Neutrons $n/cm^2 \cdot sec$	Fast Neutrons CPM	Fast Neutrons $n/cm^2 \cdot sec$	Gammas, mr/hr
	O	O	———	———	———	———	———
5000	O	C	———	———	———	———	———
	C	O	———	———	———	———	———
	C	C	———	———	———	———	———
	O	O	———	———	———	———	60,000
1000	O	C	16,300	1.25×10^2	81,000	9.00×10^2	100
	C	O	———	———	1,960,000	2.18×10^4	30,000
	C	C	———	———	———	———	———
	O	O	800,000	6.15×10^3	575,000	6.39×10^3	5,500
100	O	C	1,700	1.31×10^1	8,300	9.22×10^1	150
	C	O	372,000	2.86×10^3	278,000	3.09×10^3	3,000
	C	C	385	2.96	1,648	1.83×10^1	100

Table C.4 (Continued)

Power KW	Pb	Fe	Slow Neutrons CPM	Slow Neutrons $n/cm^2 \cdot sec$	Fast Neutrons CPM	Fast Neutrons $n/cm^2 \cdot sec$	Gammas, mr/hr
	O	O	87,000	6.69×10^2	63,000	7.00×10^2	550
10	O	C	167	1.28	800	8.89	100
	C	O	41,000	3.15×10^2	29,000	3.22×10^2	350
	C	C	33	2.54×10^{-1}	238	2.64	100

Table C.5

Dose Rates in Lattice Room

Cd Shutter Closed — C = Closed

Sat. July 13, 1968 — O = Opened

Power KW	Pb	Fe	Slow Neutrons CPM	Slow Neutrons $n/cm^2 \cdot sec$	Fast Neutrons CPM	Fast Neutrons $n/cm^2 \cdot sec$	Gammas, mr/hr
	O	O	———	———	———	———	———
5000	O	C	———	———	———	———	———
	C	O	———	———	———	———	———
	C	C	———	———	———	———	———
	O	O	289,000	$2.22X10^3$	470,000	$5.22X10^3$	1,800
1000	O	C	15,500	$1.19X10^2$	74,200	$8.24X10^2$	100
	C	O	160,200	$1.23X10^3$	180,000	$2.00X10^3$	1,000
	C	C	13,343	$2.57X10^1$	15,900	$1.77X10^2$	150
	O	O	29,000	$2.23X10^2$	51,600	$5.74X10^2$	300
100	O	C	1,523	$1.17X10^1$	7,700	$8.55X10^1$	100
	C	O	15,839	$1.22X10^2$	18,419	$2.05X10^2$	200
	C	C	309	2.38	1,686	$1.87X10^1$	100

Table C.5 (Continued)

Power KW	Pb	Fe	Slow Neutrons CPM	Slow Neutrons $n/cm^2 \cdot sec$	Fast Neutrons CPM	Fast Neutrons $n/cm^2 \cdot sec$	Gammas, mr/hr
	0	0	2,850	$2.19X10^{1}$	5,296	$5.89X10^{1}$	100
10	0	C	160	1.23	843	9.36	100
	C	0	1,528	$1.17X10^{1}$	1,911	$2.22X10^{1}$	100
	C	C	30	$2.31X10^{-1}$	210	2.34	100

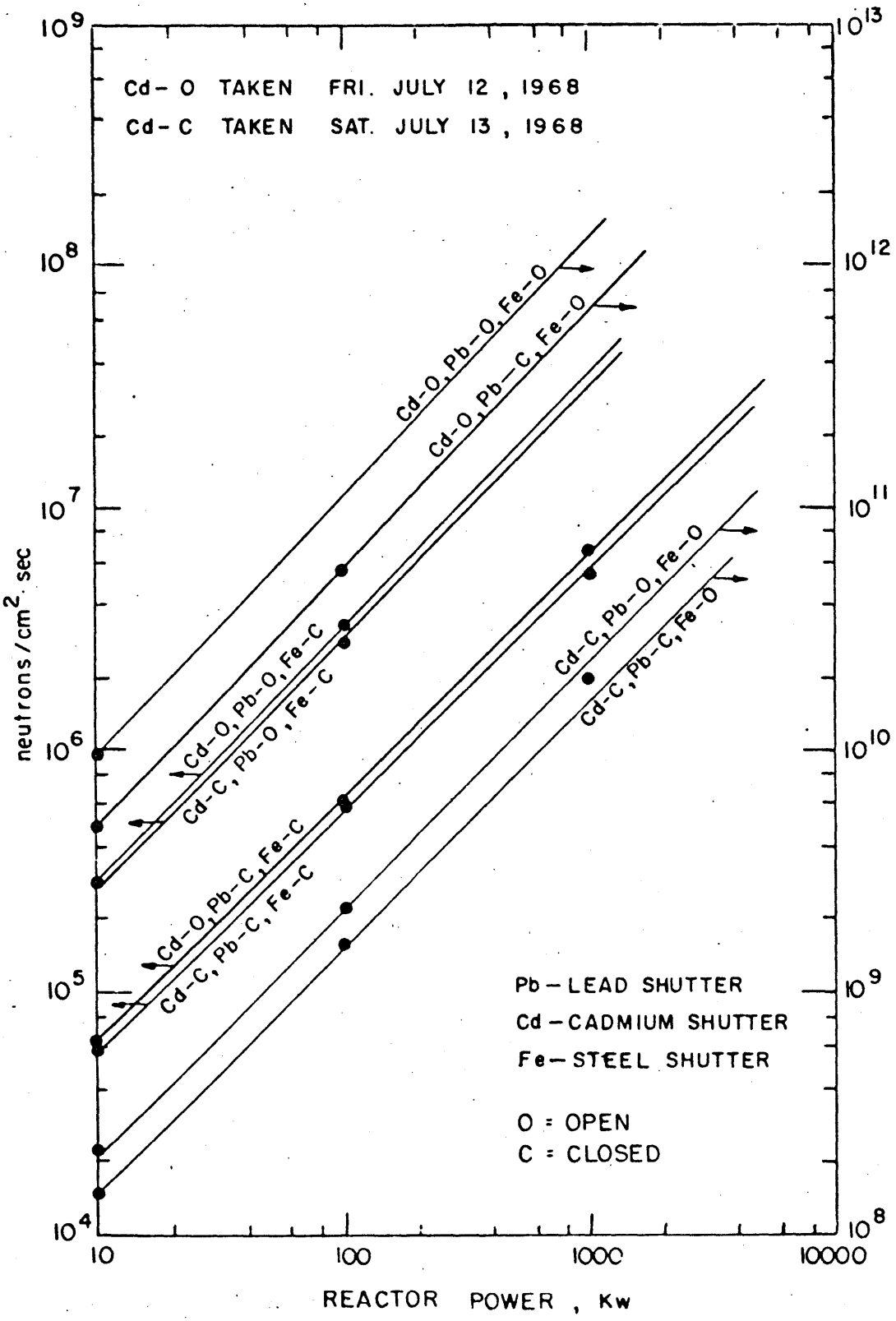

FIG. C.2. HOHLRAUM SLOW NEUTRONS

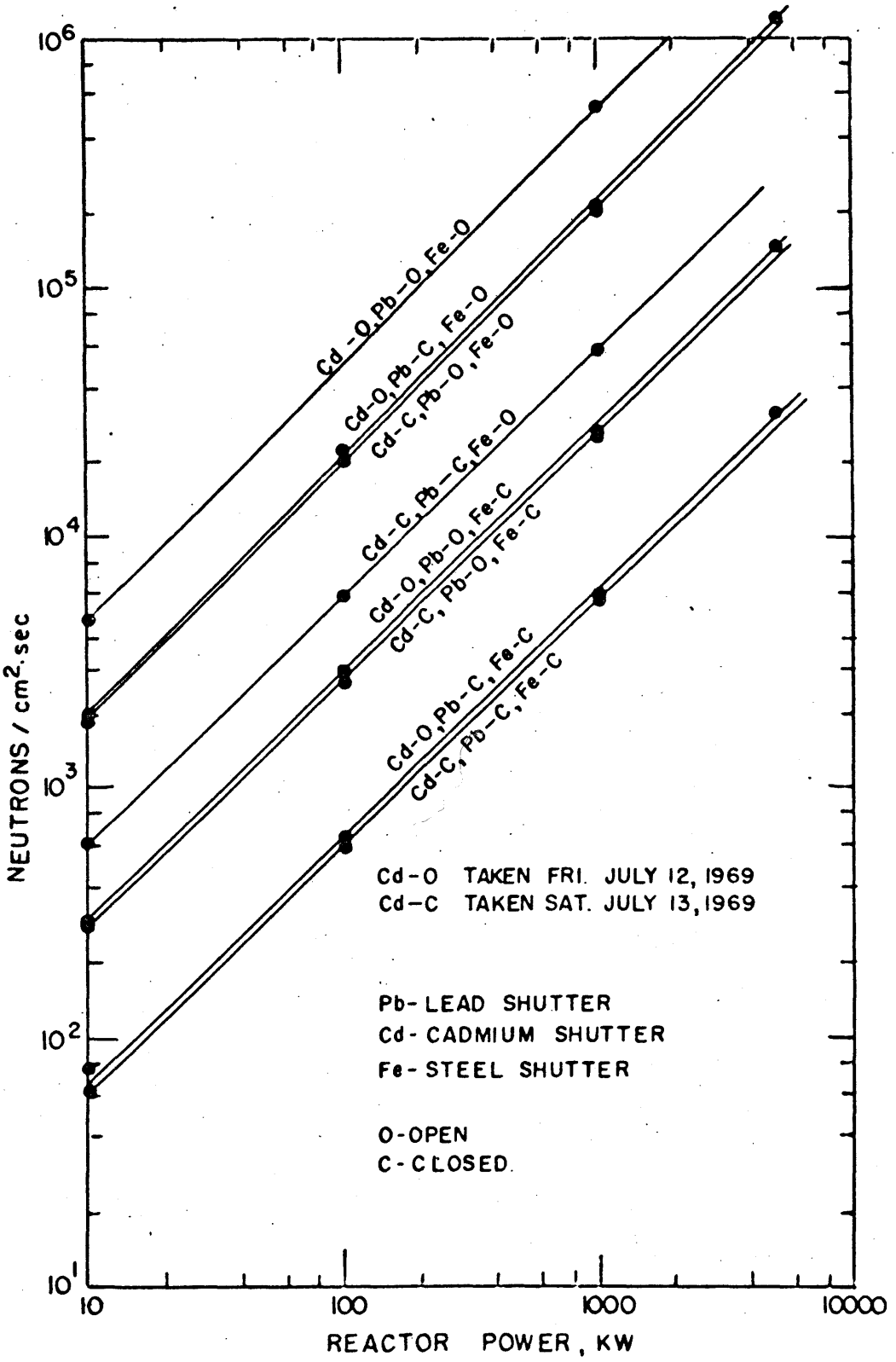

FIG.C.3 HOHLRAUM FAST NEUTRONS

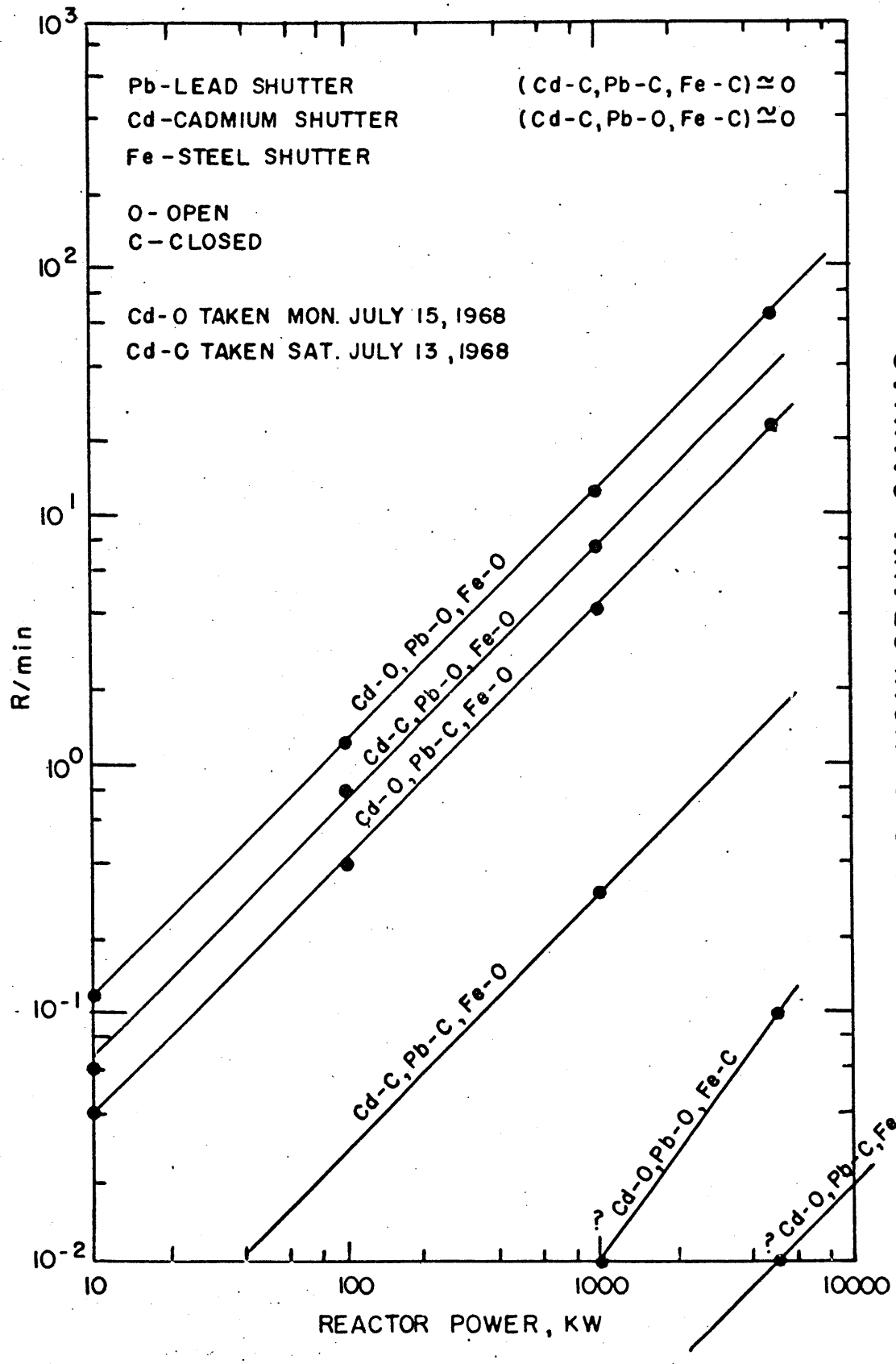

FIG. C.4 HOHLORAUM GAMMAS

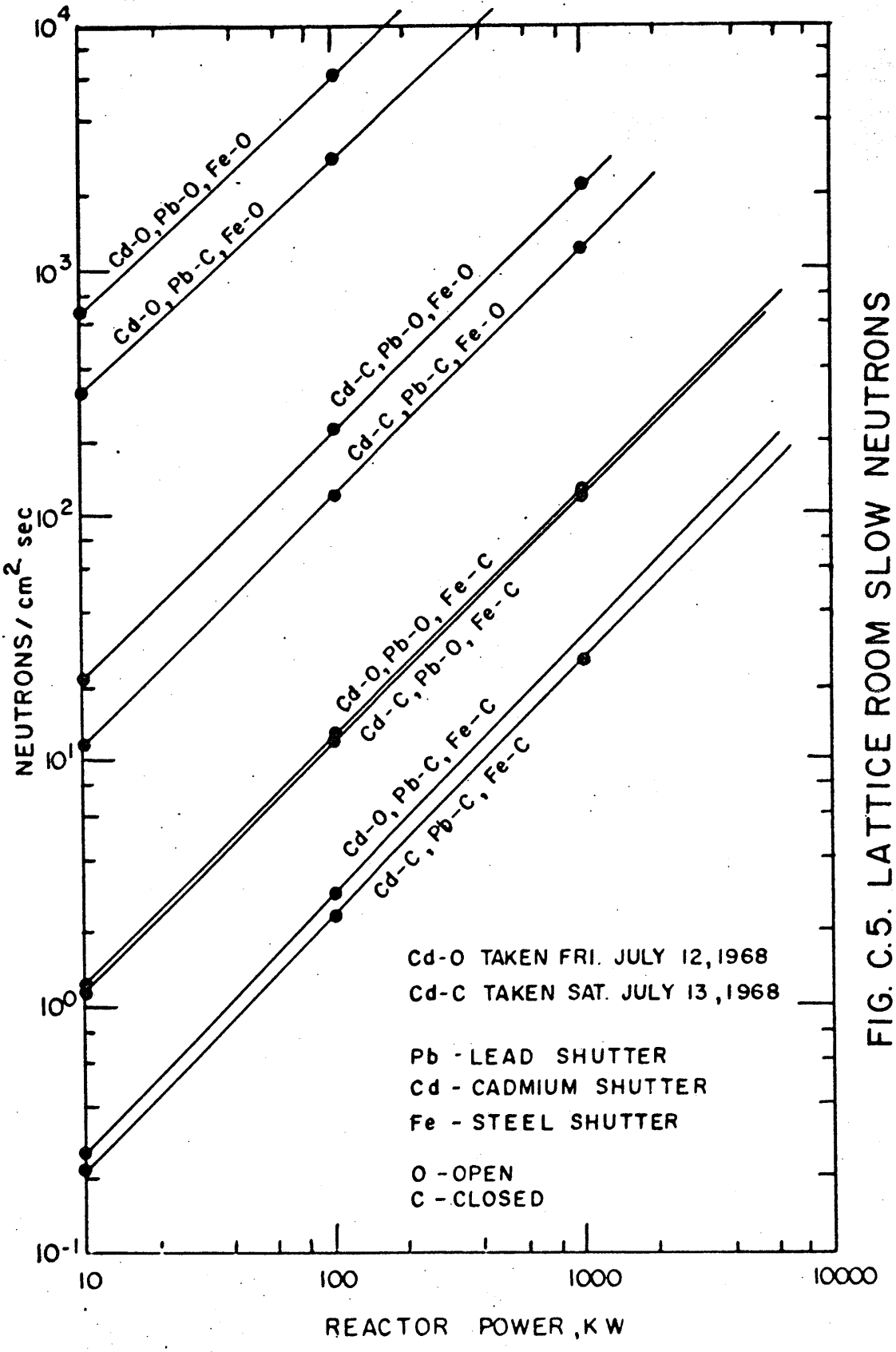

FIG. C.5. LATTICE ROOM SLOW NEUTRONS

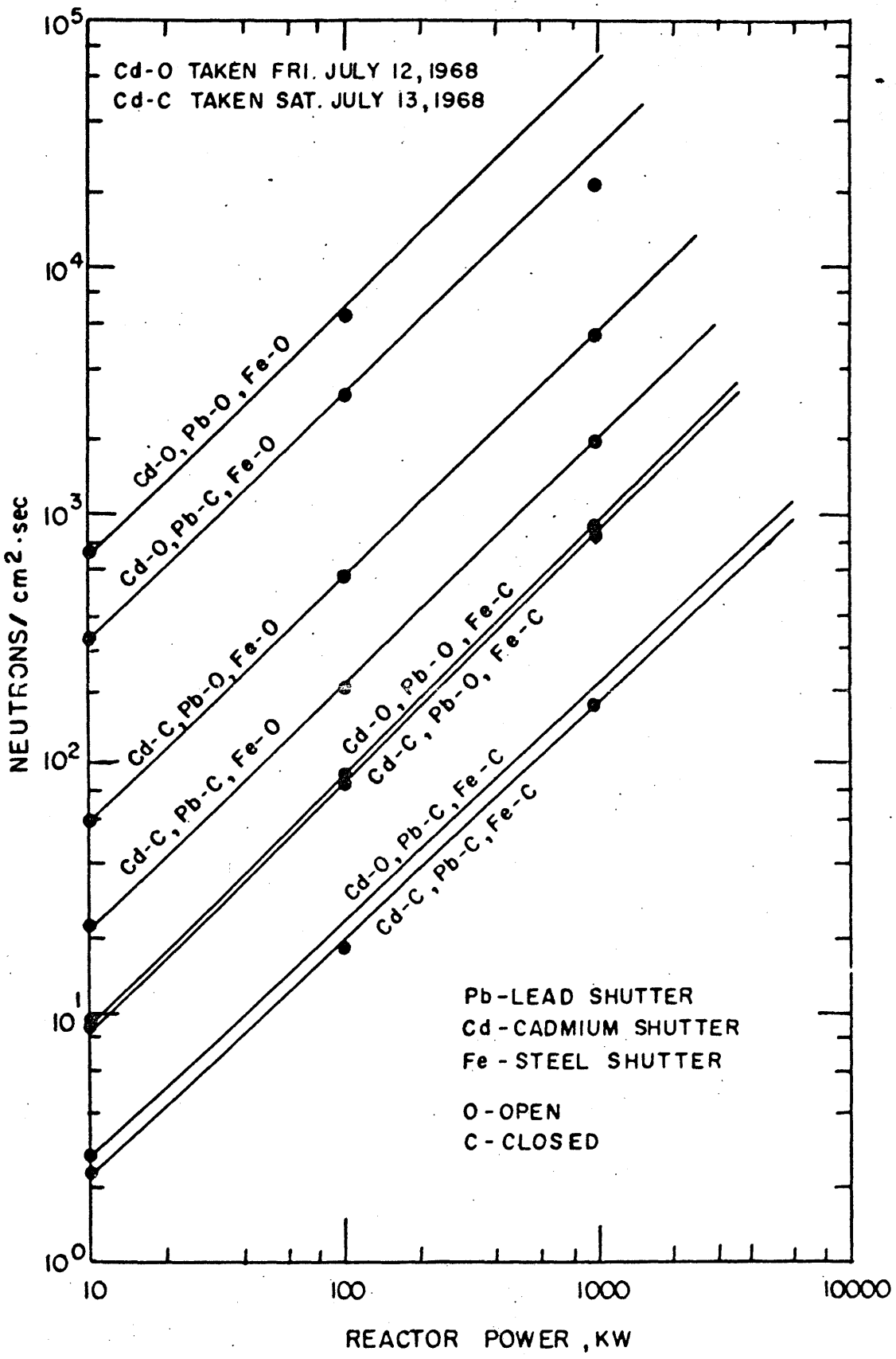

FIG. C·6. LATTICE ROOM FAST NEUTRONS

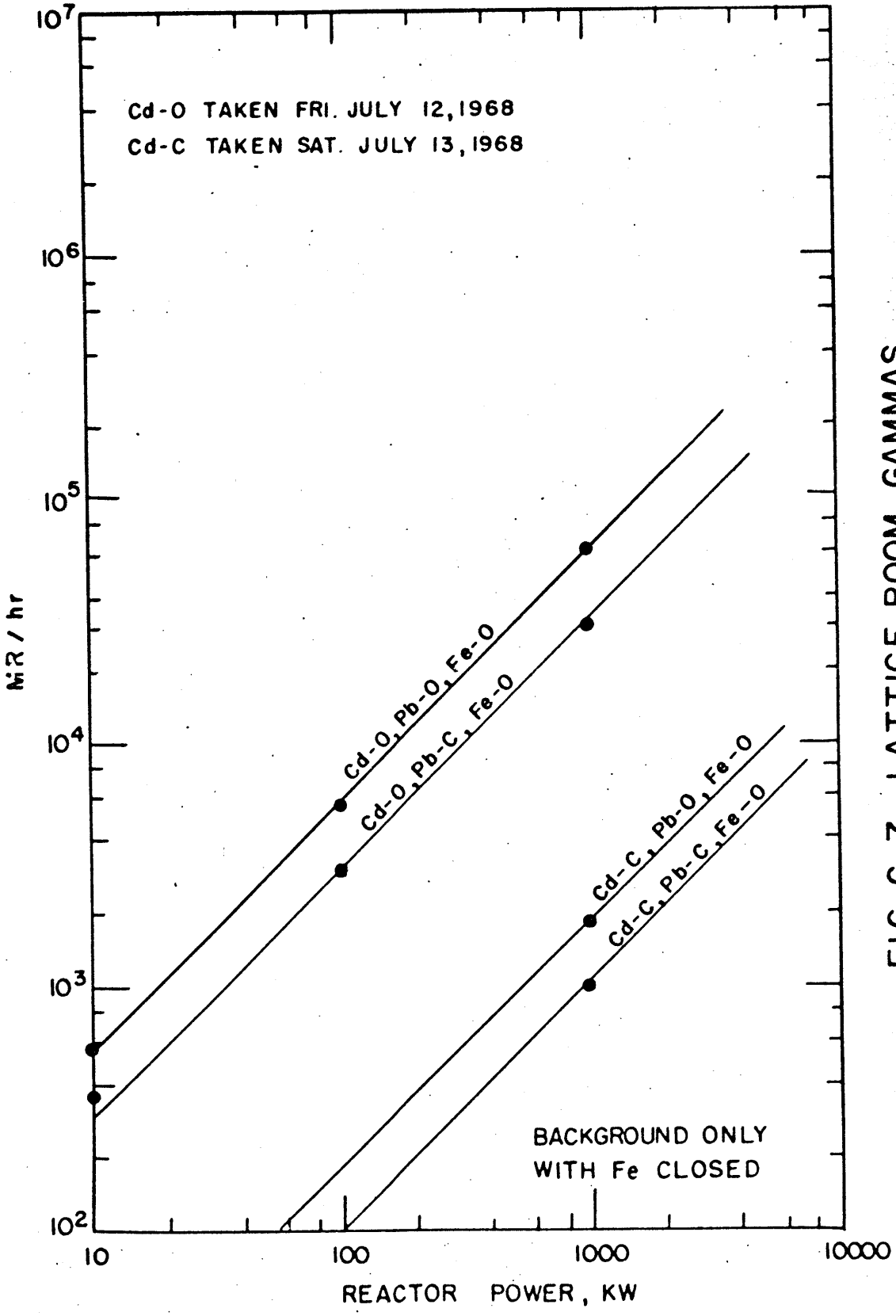

FIG. C. 7. LATTICE ROOM GAMMAS

column itself.

The steel doors appear to be the most effective shield against fast neutrons in both the hohlraum and lattice room. One would expect this for the hohlraum but not for the lattice room since the steel doors do not lie in the line of sight from the reactor to the lattice room. The apparent effect is probably due to the way in which the fast neutrons were measured. The fast neutron detectors were sheathed in cadmium; therefore, they were actually measuring epicadmium neutrons which include some of the thermal spectrum which can be reflected into the lattice room by the hohlraum. Thus, any effect the steel doors have on thermal neutrons above the cadmium cut-off would be observed as an effect on fast neutrons. In fact because of the observed large effect ($\frac{\phi_{\text{fast, steel closed}}}{\phi_{\text{fast, steel open}}} \sim 0.01$), it may be concluded that most of "fast" neutrons are really epicadmium thermal neutrons, and that the real fast flux is very small.

Appendix D

Cryostat Heat Load Calculations

D.1. Thermal Column Flux Measurements

To determine the induced heating due to thermal neutrons, fast neutrons, and graphite capture gammas, it is necessary to know these fluxes in the thermal column. As part of this work the absolute thermal flux and cadmium ratio were measured in a horizontal beam port in the thermal column (9CHI) using cobalt and gold foils. The foils were counted with a NaI crystal calibrated for absolute count rates for cobalt (11).

The cadmium ratio is given by

$$CR = \frac{(C_b-CB)W_c[1-T(C_c-CB)]}{(C_c-CB)W_b[1-T(C_b-CB)]}\, e^{\lambda(T_D{}^b-T_D{}^c)} \qquad (D.1)$$

where C_b = bare foil count rate

C_c = Cd covered foil count rate

CB = background count rate

W_c = Cd covered foil weight

W_b = bare foil weight

T = counter dead time

λ = foil decay constant

$T_D{}^b$ = bare foil decay time

$T_D{}^c$ = Cd covered foil decay time.

The absolute 2200m/sec flux is given by

$$\phi_{2200} = \frac{A(1-\frac{1}{CR})(C_b-CB)e^{\lambda T_D{}^b}}{N_o W_b \sigma_{2200} \varepsilon [1-T(C_b-CB)]\{1-e^{-\lambda(TR-TC)}[1-\alpha(1-e^{-\lambda TC})]\}} \quad (D.2)$$

where A = atomic weight

N_o = Avogadro's number

σ_{2200} = 2200 m/sec activation cross section

ε = counter efficiency = 0.00859 (11)

TR = total irradiation time = 100 hr, 23 min

TC = time lead shutters closed = 8 hr, 3 min

α = ratio of flux with lead shutter closed to flux with shutter open = 0.52 (12).

The parameters needed to calculate the cadmium ratio and ϕ_{2200} are given in Table D.1.

Table D.1

Thermal Column Flux Data

	Cobalt	Gold
C_b, counts/min	334,338	139,347
C_c, counts/min	1,779	77,340
CB, counts/min	73.6	110
W_b, grams	0.020333	0.003261
W_c, grams	0.053660	0.012264
T, min	$(2.15\pm).65)10^{-9}$	$(1.97\pm0.56)10^{-7}$
λ, hr^{-1}	$1.5072X10^{-5}$	0.010736
$T_D{}^b$, hr	576	329.15
$T_D{}^c$, hr	576	69.57
A, amu	58.94	———
σ_{2200}, barns	37.3	———

The dead times were measured using the two source method. The foils were Al-Au(.072%) wire 30 mils in diameter and Al-Co (0.55%) wire 40 mils in diameter. The cadmium covering was 40 mil. diameter tubing with a 20 mil wall. No correction has been made for flux depressions in the foils.

By using the data in Table D.1 gives

[CR] Cobalt = 517.76±4.35

[CR] Gold = 111.44±1.14.

The higher value for cobalt is due to the fact that the infinitely dilute resonance integral for cobalt is only about 75 barns as compared with about 1500 barns for gold.

Using the data for cobalt gives

$$\phi_{2200} = (5.80\pm0.03)10^{10} n/cm^2 \cdot sec$$

and $$\phi_{th} = \frac{\sqrt{4T}}{\pi T_o} \phi_{2200} = (7.34\pm0.04)10^{10} n/cm^2 \cdot sec$$

where T was measured to be 70°C.

This value of ϕ_{th} is on the order of 50% lower than values listed in Reactor Operations (12). This is consistent with results Bill Bley (11) has obtained in other parts of the reactor.

D.2. Core Gamma Heating

Consider an infinite planar medium of thickness t separated from the reactor core by a thickness L of graphite. Assume the core gamma flux to be a plane source with n energy groups. The flux for the i^{th} group is

$$S_i = S_o R_i \tag{D.3}$$

where R_i = fraction of gammas in i^{th} group

S_o = total source flux.

The total source flux is given by

$$S_o = \frac{2D}{\sum_n R_i E_i \left(\frac{\mu_a}{\rho}\right)_i^a} \tag{D.4}$$

where D = measured dose rate at core tank

E_i = energy of i^{th} group

$\left(\frac{\mu_a}{\rho}\right)_i^a$ = mass absorption coefficient in air for i^{th} group.

The i^{th} group gamma flux reaching the medium is given by

$$\phi_i = \frac{S_i}{2} K_i = \frac{S_o}{2} R_i K_i \tag{D.5}$$

where

$$K_i = \int_{\mu_{oi}^G L}^{\infty} \frac{e^{-x}}{x} dx \tag{D.6}$$

and μ_{oi}^G = total attenuation coefficient in graphite for i^{th} group.

The energy deposited by the i^{th} group in a thickness dx of the medium is given by

$$dP_i = B_i^G B_i^M \mu_{ai}^M E_i \phi_i e^{-\mu_{oi}^M x} dx \tag{D.7}$$

or

$$dP_i = B_i^G B_i^M \mu_{ai}^M E_i \frac{S_o}{2} R_i K_i e^{-\mu_{oi}^M x} dx \tag{D.8}$$

where B_i^G = build up factor in graphite for i^{th} group

B_i^M = build up factor in medium for i^{th} group

μ_{ai}^M = energy absorption coefficient in medium for i^{th} group

μ_{oi}^M = total attenuation coefficient in medium for i^{th} group.

Defining the volumetric heat generation for the i^{th} group as

$$H_i = \frac{1}{t}\int_o^t dP_i \qquad (D.9)$$

gives $$H_i = \frac{S_o}{2} R_i K_i B_i {}^{G}B_i {}^{M}E_i \left(\frac{\mu_{ai}}{\mu_{oi}}{}^{M}_{M}\right)\left[\frac{1-e^{-\mu_{oi}{}^{M}t}}{t}\right] . \qquad (D.10)$$

Substituting equation (D.4) and summing over n gives the total volumetric heat generation

$$H_T = \frac{D\Sigma_n R_i K_i B_i {}^{G}B_i {}^{M}E_i \left(\frac{\mu_{ai}}{\mu_{oi}}{}^{M}_{M}\right)[1-e^{-\mu_{oi}{}^{M}t}]}{t\Sigma_n R_i E_i \left(\frac{\mu_a}{P}\right)_i {}^{a}} . \qquad (D.11$$

The group parameters needed to evaluate equation (D.11) are given in Table D.2. The R_i's have been taken from Frank Berte's thesis (13), and the other parameters from ANL-5800 (14). The values for D_2O have been taken as those given for H_2O.

Using the following values:

$D = 1.3X10^{8}$ r/hr (12)

$t_{AL} = 1$ cm

$t_{D_2O} = 30$ cm

$L = 58.42$ cm

gives, $H_{AL} = 10.91X10^{-3}$ watt/cm^3

$H_{D_2O} = 3.968X10^{-3}$ watt/cm^3 .

The core gamma heating which has to be removed by the helium coolant is that generated in the aluminum supply line, the aluminum return line, the aluminum sphere, the aluminum coils, the aluminum beam tube, and the D_2O moderator. These heat loads are given in Table D.3.

Table D.2

Group Constants for Core Gamma Heating

Group	E_i, Mev	R_i	K_i	B_i^G	$B_i^{D_2O}$	B_i^{AL}	$\mu_{ai}^{D_2O}$ cm^{-1}	$\mu_{oi}^{D_2O}$ cm^{-1}	μ_{ai}^{AL} cm^{-1}	μ_{oi}^{AL} cm^{-1}	$(\frac{\mu_a}{P})_i^a$ $\frac{cm^2}{g}$
1	0.25	.5830	.00000	108.00	8.75	1.23	.0311	.12700	.0754	.3010	.0278
2	0.75	.2116	.00016	26.60	3.44	1.11	.0323	.08135	.0756	.1907	.0291
3	1.25	.0905	.00091	10.10	2.16	1.07	.0298	.06300	.0699	.1480	.0268
4	1.75	.0396	.00210	6.37	1.78	1.05	.0274	.05340	.0648	.1258	.0247
5	2.25	.0230	.00407	4.58	1.58	1.04	.0256	.04690	.0613	.1113	.0231
6	2.75	.0159	.00673	3.76	1.47	1.03	0.241	.04200	.0585	.1006	.0218
7	3.25	.0102	.01013	3.21	1.39	1.03	.0228	.03820	.0564	.0924	.0207
8	3.75	.0081	.01375	2.83	1.33	1.02	.0218	.03530	.0548	.0866	.0198
9	4.25	.0057	.01779	2.57	1.28	1.02	.0209	.03295	.0535	.0818	.0191
10	4.75	.0042	.02216	2.38	1.25	1.02	.0202	.03105	.0523	.0780	.0184
11	5.25	.0029	.02597	2.24	1.23	1.02	.0196	.02945	.0516	.0749	.0179
12	5.75	.0017	.03088	2.09	1.20	1.02	.0190	.02815	.0510	.0725	.0174
13	6.25	.0012	.03485	1.99	1.18	1.01	.0186	.02706	.0506	.0705	.0170
14	6.75	.0006	.03827	1.92	1.17	1.01	.0182	.02618	.0503	.0690	.0162

Table D.3

Core Gamma Heat Load

Watts

Sup. Line	Ret. Line	Sphere	Coils	Beam Tube	D_2O
0.786	0.786	5.055	0.878	3.943	58.832

D.3. Graphite Gamma Heating

The model used for calculating the induced heating due to graphite capture gammas is shown in figure D.1

The medium in which the heating is to be calculated is taken as an infinite plane of thickness t. The graphite in the thermal column is divided into slabs, and the gammas generated in each slab are assumed to be an infinite plane source at the center of the slab.

Following the procedure of section D.2 gives the volumetric heat generation,

$$H = \frac{EB^M(\frac{\mu_a{}^M}{\mu_o{}^M})(1-e^{-\mu_o{}^M t})}{2t} \sum_n S_i K_i B_i{}^G \qquad (D.12)$$

where E = gamma ray energy = 5 Mev

B^M = build up factor for medium

$\mu_a{}^M$ = energy absorption coefficient for medium

$\mu_o{}^M$ = total attenuation coefficient for medium

$B_i{}^G$ = build up factor for i^{th} slab of graphite

S_i = gamma source flux for i^{th} slab

n = number of slabs

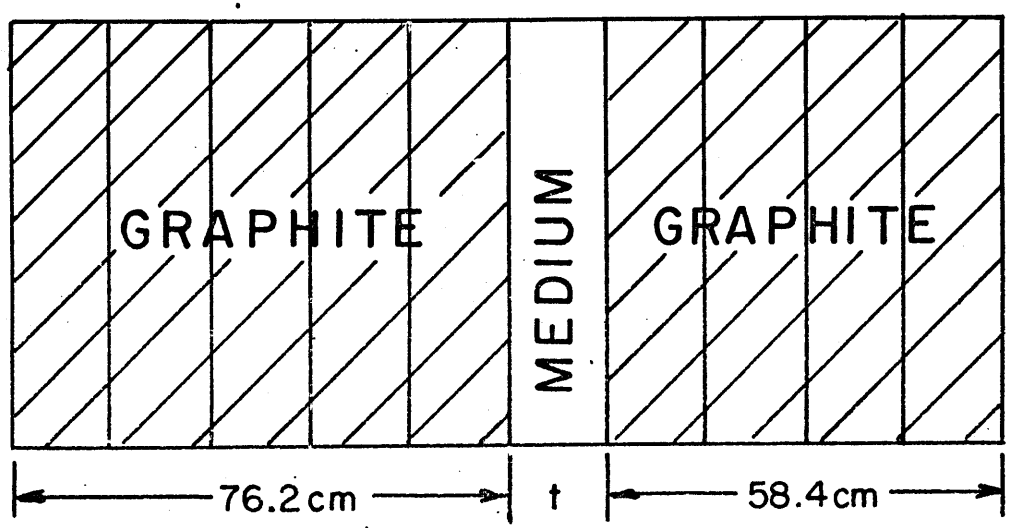

FIGURE D.I. MODEL FOR GRAPHITE GAMMA HEATING

$$K_i = \int_{\mu_o{}^G L_i}^{\infty} \frac{e^{-x}}{x}\, dx \qquad (D.13)$$

$\mu_o{}^G$ = total attenuation coefficient for graphite

L_i = distance from center of i^{th} slab to medium.

Assuming graphite is a 1/v absorber and taking ϕ_{2200} as

$$\phi_{2200} = (5.8X10^{10}\ n/cm^2\cdot sec)\cos\frac{\pi x}{a}\cos\frac{\pi y}{b}\, e^{-\gamma(z-76.20cm)} \qquad (D.14)$$

gives

$$S_i = \frac{8(5.8X10^{10})\Sigma_a{}^{2200}}{\pi^2\gamma}\sinh\gamma\frac{\Delta}{2}\, e^{\gamma L_i} \qquad (D.15)$$

where

$\Sigma_a{}^{2200}$ = 2200 m/sec absorption cross section for graphite = $2.728X10^{-4}$/cm

$$\gamma = [\frac{1}{L^2} + (\frac{\pi}{a})^2 + (\frac{\pi}{b})^2]^{1/2} = 0.03335/cm$$

L = diffusion length of graphite = 53 cm

a = thermal column height = 162.1 cm

b = thermal column width = 161.1 cm

Δ = slab thickness = $\begin{cases} 15.24\ cm, & o<z<76.20\ cm \\ 14.60\ cm, & 76.20\ cm<z<134.6\ cm. \end{cases}$

Substituting equation (D.15) into equation (D.12) gives

$$H = \frac{(23.2X10^{10})\Sigma_a{}^{2200}EB^M(\frac{\mu_a{}^M}{\mu_o{}^M})(1-e^{-\mu_o{}^M t})}{\pi^2\gamma t} X\sinh\gamma\frac{\Delta}{2}\sum_n K_i B_i{}^G e^{\gamma L_i} \qquad (D.16)$$

The parameters needed to evaluate equation (D.16) have been taken from ANL-5800(14) and are given in Table D.4.

Using these constants and the following values:

$B^{D_2O} = 1.23$

$B^{AL} = 1.01$

$\mu_a^{D_2O} = 0.0198/cm$

$\mu_o^{D_2O} = 0.0301/cm$

$\mu_a^{AL} = 0.0518/cm$

Table D.4

Constants for Graphite Gamma Heating

Slab	Li,cm	Ki	B_i^G
1	68.58	.01370	2.53
2	53.34	.03234	2.19
3	38.10	.08095	1.86
4	22.86	.2240	1.51
5	7.62	.8379	1.17
6	7.30	.8690	1.16
7	21.90	.2403	1.49
8	36.50	.08948	1.82
9	51.10	.03681	2.15

$\mu_o^{AL} = 0.0761/cm$

$t_{D_2O} = 30$ cm

$t_{AL} = 1$ cm

gives,

$$H_{D_2O} = 2.707X10^{-6} \text{ watt/cm}^3$$

$$H_{AL} = 8.502X10^{-6} \text{ watt/cm}^3.$$

The heat due to graphite gamma heating which must be removed by the coolant helium is given in Table D.5.

Table D.5

Graphite Gamma Heat Load

Milliwatts

Sup. Line	Ret. Line	Sphere	Coils	Beam Tube	D_2O
0.613	0.613	3.939	0.684	3.073	40.136

D.4. Fast Neutron Heating

The energy deposited in a medium due to the slowing down of fast neutrons is given by

$$H = \int E_L \Sigma_S(E) \phi(E) dE \qquad (D.17)$$

where E_L = energy lost per collision

$\Sigma_S(E)$ = scattering cross section

$\phi(E)$ = fast neutron flux.

Assuming isotropic scattering,

$$E_L = \frac{2A}{(A+1)^2} E.$$

Assuming

$$\phi(E) = \phi_o/E$$

and $\Sigma_S(E)$ = Constant

gives

$$H = \frac{2A}{(A+1)^2}\Sigma_S\phi_o\Delta E \qquad (D.18)$$

where ΔE = energy range of fast neutrons.

The activation of a bare irradiated foil is given by

$$(Act)_B = \int_o^\infty \phi\sigma dE = \int_o^{E_c} \phi\sigma dE + \int_{E_c}^\infty \phi\sigma dE \qquad (D.19)$$

where E_c = cadmium cut-off energy.

Assuming σ is 1/v for E less than E_c, and $\phi = \phi_o/E$ for E greater than E_c, gives

$$(Act)_B = \phi_{2200}\sigma_{2200} + \phi_o I_\infty \qquad (D.20)$$

where σ_{2200} = 2200 m/sec activation cross section

I_∞ = infinite dilute resonance integral.

The activation of a cadmium covered irradiated foil is given by

$$(Act)_{Cd} = \int_{E_c}^\infty \phi\sigma dE = \phi_o I_\infty = (Act)_B/CR \qquad (D.21$$

where CR = cadmium ratio.

Using equations (D.21), (D.20), and (D.18) gives

$$H = \frac{2A\Sigma_S\phi_{2200}\sigma_{2200}\Delta E}{(A+1)^2 I_\infty (CR-1)} \cdot \qquad (D.22)$$

Using,

$\phi_{2200} = 5.80X10^{10}$ n/cm^2·sec

$\Delta E = 10$ Mev

$CR_{Au} = 111$

$\sigma_{2200}^{Au} = 98.8b$

$I_\infty^{Au} = 1490b$

$$A_{D_2O} = 3.595(15)$$

$$A_{AL} = 27$$

$$\Sigma_S^{D_2O} = 0.4519/cm$$

$$\Sigma_S^{AL} = 0.08434/cm$$

gives

$$H_{D_2O} = 6.633X10^{-6} \text{ watt/cm}^3$$

$$H_{AL} = 3.252X10^{-7} \text{ watt/cm}^3.$$

The induced heat due to fast neutrons which must be removed by the coolant helium is given in Table D.6.

Table D.6

Fast Neutron Heat Load

Milliwatts

Sup. Line	Ret. Line	Sphere	Coils	Beam Tube	D_2O
0.023	0.023	0.151	0.026	0.118	98.346

The cobalt data gives values about 60% higher than the gold data; however, the fast neutron heat load is still very small compared to the radiant heat transfer and core gamma heat load.

D.5. Cryostat Gamma Heating

Thermal neutrons cause heating through the gamma rays given off in the (n,γ) reaction. Assuming the medium is a 1/v absorber and taking ϕ_{2200} as given in equation (D.15), results in

$$S = \frac{(4.69X10^{11})\Sigma_a^{2200}}{\pi^2\gamma}\text{Sinh}\gamma\frac{t}{2} \qquad (D.23)$$

where S = gamma flux

γ = 0.03335/cm

Σ_a^{2200} = 2200 m/sec absorption cross section for the medium

t = thickness of medium.

If gammas of different energies are given off, the flux for the i^{th} group is

$$\phi_i = \frac{(4.64X10^{11})\Sigma_a^{2200}R_i}{\pi^2\gamma}\text{Sinh}\ \gamma\frac{t}{2} \qquad (D.24)$$

where R_i = fraction of gammas given off in i^{th} group.

The volumetric heat generation is given by

$$H = \frac{(4.64X10^{11})\Sigma_a^{2200}}{\pi^2\gamma}\ \text{Sinh}\gamma\frac{t}{2}\Sigma_n R_i\mu_{ai}E_i \qquad (D.25)$$

where n = number of energy groups

E_i = energy of i^{th} group

μ_{ai} = energy absorption coefficient in medium for i^{th} group.

In D_2O one 6 Mev gamma is given off for every thermal neutron absorbed. Using,

$\Sigma_a^{2200} = 3.323X10^{-5}$/cm

t = 30 cm

μ_a = .0188/cm

gives

$H_{D_2O} = 2.665X10^{-7}$ watt/cm^3.

The gammas given off by aluminum have been separated into 9 energy groups. The group constants, taken from ANL-5800 (14), are given in Table D.7.

Table D.7

Group Constants for Aluminum Gamma Heating

Group	E_i, Mev	R_i	μ_{ai}, cm-1
1	0.5	.67428	.0772
2	1.5	.55714	.0670
3	2.5	.19714	.0599
4	3.5	.17714	.0556
5	4.5	.17714	.0529
6	5.5	.05428	.0513
7	6.5	.05428	.0505
8	7.5	.05428	.0497
9	8.5	.05428	.0493

The fact that the R_i's add up to two is due to the fact that about 2 gamma rays are given off for every thermal neutron absorbed.

Using,

$$\Sigma_a^{2200} = 0.01416/\text{cm}$$

$$t = 1 \text{ cm}$$

gives, $H_{AL} = 1.384 \times 10^{-5}$ watt/cm^3 .

The heat load due to cryostat gammas which must be removed by the coolant helium is given in Table D.8.

Table D.8

Cryostat Gamma Heat Load

Milliwatts					
Sup. Line	Ret. Line	Sphere	Coils	Beam Tube	D_2O
0.998	0.998	6.413	1.113	5.002	3.951

D.6. Radiant Heat Transfer

The radiant heat transfer from surface 1 to surface 2 is given by

$$Q = A_1 \bar{F}_{12} \sigma (T_1^4 - T_2^4) \qquad (D.26)$$

where A_1 = area of surface 1

σ = Stefan-Boltzman constant

T_1 = absolute temperature of surface 1

T_2 = absolute temperature of surface 2

$\bar{F}_{12}$ = effective view factor from surface 1 to surface 2, and is given by

$$\bar{F}_{12} = \frac{1}{\frac{1-e_1}{e_1} + \frac{1}{F_{12}} + \left(\frac{A_1}{A_2}\right)\left(\frac{1-e_2}{e_2}\right)} \qquad (D.27)$$

where e_1 = emissivity of surface 1

e_2 = emissivity of surface 2

F_{12} = geometric view factor from surface 1 to surface 2

A_2 = area of surface 2.

The radiant heat which must be removed by the coolant helium is that transferred from the vacuum jacket to the helium supply line, the helium return line, the moderator sphere, and the beam tube. These heat loads are given in Table D.9.

The temperature of the vacuum jacket has been taken as 343°K and the emissivity as 0.085. The temperature of the supply line has been taken to be the same as the helium inlet temperature. The temperature rise of the helium has been estimated to be about 6°K; therefore, the temperature of the return line has been taken as 26°K. The surface temperature of the sphere has been calculated to be about 26°K (section 5.2). The temperature of the beam tube has been taken as its average temperature (section D.8). The emissivities have been taken from reference 16.

Table D.9

Radiant Heat Load

Surface	T,°K	e	Q, watts
Sup. Line	20	0.048	5.070
Ret. Line	26	0.048	5.070
Sphere	26	0.048	9.869
Beam Tube	48	0.053	14.552

If the aluminum surfaces become oxidized, their emissivities may rise to a value of about 0.2. In this case the radiant heat transfer will increase by about a factor of 4 resulting in a total heat load of 215 watts and a helium

temperature rise of about 12°K.

D.7. Free Molecular Conduction

Free molecular conduction is the transport of heat from the warm vacuum jacket to the cold surfaces by the molecules remaining in the vacuum. The rate of heat transfer is given by [17],

$$Q = GA_2P(T_1-T_2) \qquad (D.28)$$

where A_2 = area of cold surface

P = absolute pressure

T_1 = temperature of warm surface

T_2 = temperature of cold surface

and

$$G = \frac{\gamma+1}{\gamma-1}\left[\frac{g_c R}{8\pi M T_1}\right]^{1/2}\left[\frac{1}{a_2} + \frac{A_2}{A_1}\left(\frac{1}{a_1}-1\right)\right]^{-1} \qquad (D.29)$$

where γ = specific heat ratio

R = universal gas constant

M = gas molecular weight

a_2 = accomodation coefficient for cold surface

a_1 = accomodation coefficient for warm surface

A_1 = area of warm surface.

For air, $\gamma = 1.4$

$M = 29$

$a_1 = 0.85$

$a_2 = 1.00$.

Using these values the heat load due to free molecular conduction has been calculated. The results are given in Table D.10.

Table D.10

Free Molecular Conduction Heat Load

Surface	T, °K	Q, Milliwatts
Sup. Line	20	10.844
Ret. Line	26	10.743
Sphere	26	21.595
Beam Tube	48	27.274

It is expected that the pressure in the vacuum will be less than or equal to 10^{-4} mm of mercury; therefore, the value has been used in the calculation. The temperature of the vacuum jacket has been taken as 343°K. At a pressure of about $5X10^{-2}$ Torr the free molecular conduction becomes equal to the radiant heat transfer.

D.8. Thermal Conduction

Since the helium supply and return lines and the beam tube are in thermal contact with the shield block there will be some heat conducted into the cryostat. To reduce this heat load the helium lines and beam tube have been insulated from the shield block by stainless steel tubes approximately 17 inches long.

Neglecting the small amount of heat generated in the beam tube, the temperature of the aluminum section (figure 5.3) is given by

$$T = T_1 + (T_o - T_1)\frac{(1-\frac{x}{L_T})}{[\frac{L_s}{L_T}(\frac{k_a}{k_s}-1)+1]} \qquad (D.30)$$

where T_1 = temperature at surface of sphere = 26°K

T_o = temperature of shield block = 343°K

x = distance measured from botton of shield block

L_T = total length of beam tube = 65 in

L_T = length of stainless steel = 17.5 in

k_a = conductivity of aluminum = 128 Btu/hr·ft·°F

k_s = conductivity of stainless steel = 10 Btu/hr·ft·°F

and the heat conducted into the sphere is given by

$$Q = \frac{(T_o - T_1)k_a \pi D t}{L_T[\frac{L_s}{L_T}(\frac{k_a}{k_s}-1)+1]} \qquad (D.31)$$

where D = diameter of beam tube = 3 inches

t = thickness of beam tube = 0.065 inches.

Using the values listed gives

Q = 4.038 watts.

and an average temperature for the beam tube of 48°K.

Again neglecting heat generation, the heat conducted into the helium lines is given by

$$Q = \frac{(T_o - T_1)k_s \pi D t}{L_s} \qquad (D.32)$$

where T_1 = temperature of the line

D = diameter of stainless steel tube = $2\frac{3}{8}$ in

t = thickness of stainless steel tube = 0.02 in.

For the supply line, T_1 = 20°K and

$Q = 1.247$ watts.

For the return line, t_1 = 26°K and

$Q = 1.222$ watts.

A summary of the heat loads is given in Table 5.1.

Appendix E

Helium Pressure Drop Calculations

E.1 Supply and Return Lines

The pressure drop through the helium supply and return lines is given by

$$\frac{dP}{dL} = f\frac{32\dot{m}^2}{\pi^2 g_c \rho^5 D^5} \qquad (E.1)$$

where D = tube diameter

f = Fanning friction factor

$\dot{m}$ = mass flow rate.

Since the flow rate is 55.09 lbm/hr, the Reynolds number is greater than $2X10^4$ and the friction factor is given by [1]

$$f = \frac{0.046}{R_e^{0.2}} = 0.046\left(\frac{\pi D\mu}{4\dot{m}}\right)^{0.2} \qquad (E.2)$$

where μ = viscosity.

Substituting into equation (E.1) gives

$$\frac{dP}{dL} = 1.472\left(\frac{\dot{m}}{\pi}\right)^{1.8}\left(\frac{\mu}{4}\right)^{0.2}\frac{1}{\rho g_c D^{4.8}} \cdot \qquad (E.3)$$

Using $\dot{m}$ = 55.09 lbm/hr

μ = 0.00813 lbm/hr·ft

ρ = 0.1952 lbm/ft^3

D = 0.93in.

gives $\frac{dP}{dL} = 1.1257X10^{-4}$ psi/in.

The supply and return lines are each 130 inches long; therefore the pressure drop for each one is

$\Delta P = 0.01463$ psi.

E.2. Cooling Coils

The cooling coil consists of four $\frac{1}{4}$" diameter aluminum coils operated in parallel. Each coil has an entrance, an exit, and four 90 degree turns. The pressure drop for each coil is given by

$$\Delta P = (\frac{dP}{dL})L + \Delta P_{ent} + \Delta P_{ext} + 4\Delta P_{90} \qquad (E.4)$$

where $\frac{dP}{dL}$ = pressure drop along the length of the coil

L = length of coil

P_{ent} = entrance pressure drop

P_{ext} = exit pressure drop

P_{90} = 90 degree turn pressure drop.

The pressure drop along the length of the coil is given by equation (E.3). The entrance pressure drop is given by (1),

$$\Delta P_{ent} = \frac{8\dot{m}^2}{g_c \pi^2 \rho D_c^4}[1.4 - 16(\frac{D_c}{D_L})^4] \qquad (E.5)$$

where D_c = diameter of coil tube

D_L = diameter of supply and return lines.

The exit pressure drop is given by (1)

$$\Delta P_{ext} = \frac{8\dot{m}^2}{g_c \pi^2 \rho D_c^4}[16(\frac{D_c}{D_L})^4 - 0.12] . \qquad (E.6)$$

The 90 degree turn pressure drop is given by (1)

$$\Delta P_{90} = \left(\frac{dP}{dL}\right)(D_c)\left(\frac{L}{D}\right)_{90} \qquad \text{(E.7)}$$

where

$$\left(\frac{L}{D}\right)_{90} = 31 .$$

Substituting equations (E.3), (E.5), (E.6), and (E.7) into equation (E.4) gives

$$\Delta P = \frac{8\dot{m}^2}{\pi^2 g_c \rho D_c^4}\left[\frac{(0.184)}{D_c^{0.8}}\left(\frac{\pi\mu}{4\dot{m}}\right)^{0.2}(L+124D_c) + 1.28\right]. \qquad \text{(E.8)}$$

Using

$$\dot{m} = \frac{1}{4}(55.09 \text{ lbm/hr})$$

$$\rho = 0.1952 \text{ lbm/ft}^3$$

$$D_c = 0.2725 \text{ in}$$

$$\mu = 0.00813 \text{ lbm/hr·ft}$$

$$L = 60 \text{ in}$$

gives

$$\Delta P = 0.37848 \text{ psi} .$$

References

1. Rohsenow, W. M., Choi, H., "Heat, Mass, and Momentum Transfer," Prentice-Hall (1961).

2. Madell, J. T., "Thermal Neutron Flux on the Surfaces of a Graphite Lined Cavity," Ph.D. Thesis, Nucl. Eng. Dept., M.I.T. (1961).

3. Pigford, T., Jones, A., Martinez, J., Kirshbaum, A., "Angular Distribution of Neutrons from a Graphite Surface," Transactions of A.N.S., Dec. 1960, page 466.

4. Placzek, G., "The Angular Distribution of Neutrons Emerging from a Plane Surface," Physics Review, 72, 556, 1947.

5. Heimberg, E. C., "Monte Carlo Studies," MS Thesis, Nucl. Eng. Dept., M.I.T. (1969)

6. Childers, F. K., Jr., "Measurement of Effective Resonance Integral Shelf-Shielding Factor for Gold at M.I.T. Research Reactor," B.S. Thesis, Physics Department, M.I.T., June 1963.

7. Forbes, I. A., "Design, Construction, and Evaluation of a Facility for the Simulation of Fast Reactor Blankets," Ph.D. Thesis, Nucl. Eng. Dept., M.I.T. (1970).

8. Addae, A. K., Private Communication, M.I.T., 1970.

9. Driscoll, M. J., Private Communication, M.I.T., 1970.

10. Ziebold, T. O., "M.I.T. Reactor Cryogenics Facilities, Technical Specifications," MITR-CF-2, March, 1968.

11. Bley, B., Private Communication, M.I.T., 1968.

12. MITR Staff, "Reference Manual for the M.I.T. Reactor," No. 5, M.I.T.

13. Berte, F. J., "Design Calculations for an In-Pile Cryostat at the M.I.T. Reactor Facility," M.S. Thesis, Nucl. Eng. Dept., M.I.T. (1964).

14. "Reactor Physics Constants," ANL-5800(1963).

15. Toppel, B. J., Baksys, I., "The Argonne Revised Thermos Code," ANL-7023 (1965).

16. Gubareff, Janssen, Tarborg, "Thermal Radiation Properties Survey," Honeywell (1960).

17. Barron, R., "Cryogenic Systems," McGraw-Hill (1966).

18. Ziebold, T. O., Private Communication, M.I.T., 1968.

19. Webb, F. J., "Cold Neutron Sources, Part II," A.E.R.E., Harwell, Berks (1963).

20. Brown, St. John, "Neutron Energy Spectrum in D_2O," DP-33 (1954).

21. Whittemore, W. L, McReynolds, A. W., "Differential Neutron Thermalization," GA-2503 (1961).

22. Springer, T., "Transmissions-und Streuexperimente mit langsamen Neutronen am FRM-Reaktor," (Kernforschungsanlage Julick), Mit 11 Textabbildungen, (Eingegangen am 28. November, 1963).

23. Hughes, D., Schwartz, R., "Neutron Cross Section," BNL-325, Second Edition (1958).

24. Cavanaugh, G. P., "Subthermal Neutron Moderation in Low Temperature D_2O-H_2O Mixtures," B.S. Thesis, Physics Dept., MIT (1969).

25. Springer, T., "Die Streuung von langsamen Neutronen an Wasser, Eis und Wasserdampt," (Zusammenfassender Bericht), (Laboratorium fur Technische Physik der Technischen Hochschule Munchen), Mit 15 Textabbildungen, (Eingegangen am 6. Marz 1961).

26. Palevsky, H., "Looking at Matter with Particles," BNL-50059 (1967).

27. Webb, F., "Cold Neutron Sources," A.E.R.E., Harwell, Berks (1963).

28. Rush, J., Connor, D., Carter, R., "Study of D_2O Ice as a Cold-Neutron Source," Nuc. Sci. and Eng: 25, 383-389 (1966).

29. Van Dingenen, W., "Systematic Study of Some Cold Neutron Sources," Nuc. Instruments and Methods 16(1962).

30. Tunkelo, E., "Construction and Performance of a Cold Neutron Source," Ph.D. Thesis, Otanieni Institute of Technology (1966).

31. Spath, Karb, Oehme, "Safety Report on the Cold Neutron Source at FR2, Project FR2/16," KFK-818 (1968).

32. Synan, J., "A Study of Cold Neutron Moderators," MS Thesis, Nuc. Eng. Dept., MIT (1969).